Analysis of type Ia supernovae from the Young Supernova Experiment

Master's Thesis

Written by *Marcus Horskær Bredtved*

May 19, 2021

Supervised by
Radoslaw Jan Wojtak, Jens Hjorth

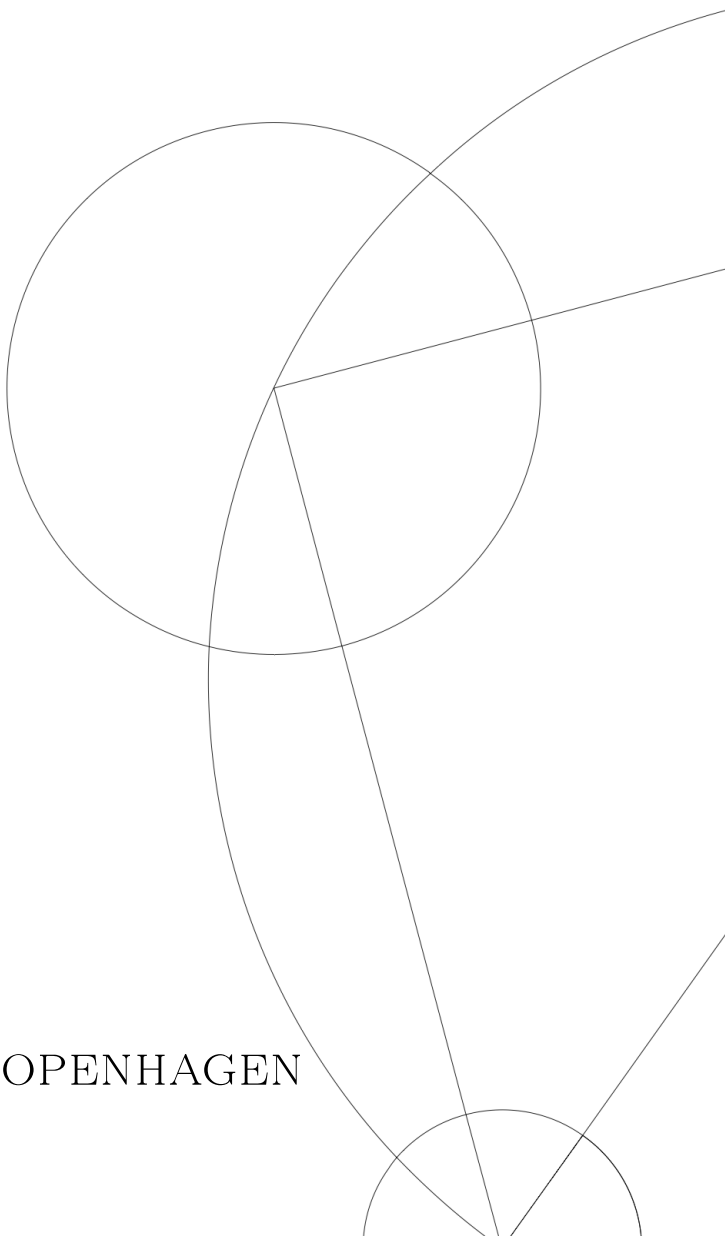

University of Copenhagen

UNIVERSITY OF COPENHAGEN

Name of Institute:	Niels Bohr Institute
Name of Department:	DARK
Author:	Marcus Horskær Bredtved
Email:	pbv615@alumni.ku.dk

Title:	Analysis of type Ia supernovae from the Young Supernova Experiment
Supervisors:	Radoslaw Jan Wojtak, Jens Hjorth
Handed in:	May 19, 2021

Abstract

Type Ia supernovae have become an increasingly popular tool among astronomers, as they offer a precise and accurate way to calibrate distances on large scales in the universe. Using data from the Young Supernova Experiment, I analyse the properties of the light curves of type Ia supernovae with the light curve fitting tool SNooPy, and apply the results to different areas of cosmology. This is done using Bayesian inference in combination with Markov Chain Monte Carlo.

Initial calibration of the supernova sample is important for quality assurance. I perform a standardization of the Ia supernova sample I gather from the Young Supernova Experiment in the BV and gr filters. I find that depending on which filters are used, one should expect to obtain different results. Furthermore, I investigate if an uncertainty on the redshift is present in my sample. I find that a single supernova outlier can drive an uncertainty in the redshift, but no uncertainty is present if the sample quality is assured.

The Hubble constant plays a key role in cosmology, as it determines the expansion rate of the universe. I measure the Hubble constant for two different calibration samples, and find $H_0 = 72.11 \pm 2.02$ km s^{-1} Mpc^{-1} using the SH0ES calibration sample, and $H_0 = 66.81 \pm 2.45$ km s^{-1} Mpc^{-1} using the SBF calibration sample.

The linear growth can help determine, if new theories of gravity might be needed to explain Dark Energy. I measure the linear growth, $f\sigma_8$, for three different samples of varying sizes. The most precise measurement is obtained by combining my sample with a subsample of the Foundation survey, for which I find $f\sigma_8 = 0.37 \pm 0.07$, in agreement with the Planck cosmology.

Because using type Ia supernovae for distance estimation is widely used among astronomers, it is important to use as good a light curve fitting tool as possible. I compare the two main light curve fitting tools, SNooPy and SALT2, by testing how well they calibrate my sample of Ia supernovae. This is done for two samples: one where all supernovae are shared, and one where the sample size is maximized individually. I find that for both samples, SALT2 performs a better calibration than SNooPy, by a measure of the intrinsic scatter. Using SALT2, I find $\sigma_{int} = 0.12 \pm 0.02$ for the shared sample and $\sigma_{int} = 0.18 \pm 0.02$ for the maximal sample, versus values from SNooPy of $\sigma_{int} = 0.17 \pm 0.04$ and $\sigma_{int} = 0.21 \pm 0.03$.

Acknowledgements

I would like to extend my sincerest thank you to my main supervisor Radek. Despite a very different year in many ways, he has been an extraordinary supervisor. Encouraging and understanding, he always had new and exciting ideas for me to explore, while also being ready to help if requested. I have no doubt that he has played a big role throughout the year for my own ambition with our work, and for that I thank him. I also thank my second supervisor Jens Hjorth, for providing comments and direction for the thesis, as well as for creating a terrific educational environment for students at DARK. This work was supported by a grant from VILLUM FONDEN (project number 16599).

I would also like to thank Luca Izzo at DARK for thoughtful and helpful discussions throughout the year, and for providing me with the data for some of the light curves used in this thesis.

Last but not least, a big thank you to three of my closest friends, who I initially met through our shared interest in astrophysics at the University of Copenhagen. Jonathan, Victoria and Katrine, the years would have have been considerably less enjoyable was it not for your company.

Dedicated to the memory of my beloved girlfriend

Contents

1 Introduction

1.1 Introduction and thesis goal

Supernovae (hereafter SN(e)) are some of the most extreme events in the universe, and therefore also some of the most interesting. Each type of SN has its own trademark making it unique, but especially one has played a key role in cosmology, namely the type Ia SN. A type Ia SN is special, because the prerequisites for one to occur are very specific, which creates a tight correlation between theory and observation. This allows for the use of type Ia SNe as cosmic yardsticks, resulting in a reliable and precise distance estimator. Because of this, Ia SNe have risen to be a center of attention and studying for many cosmologists in the recent decades, and has likewise been a part of several scientific accomplishments. This includes the discovery that the expansion of the universe is accelerating, as well as increasingly precise measurements of the Hubble constant. They are thus a powerful tool for cosmologists, and the impact they have had, and continue to have in modern research, verifies this.

The Young Supernova Experiment is an experiment aimed at observing transient astronomical events, which includes type Ia SNe. In this thesis, the aim is to use early data from the experiment to analyze the light curves (hereafter LC(s)) of type Ia SNe, and then apply the results of the LC analysis to several areas of relevance within cosmology.

The Hubble constant describes the expansion of the universe, and therefore have big implications on our understanding of it. Much work has gone into measuring this constant, and over the last couple of decades, the certainty to which this has been accomplished has become impressively high. However, as a result of increasingly precise measurements, a tension has risen due to a conflict between results obtained using different methods. Using an approach to measuring the Hubble constant based on early-universe physics, seems to produce a different result than approaches relying on late-universe physics. As such, it is of great importance to build a significant sample of measurements. This will help to determine whether our understanding of the physics are wrong, and hence if the model that these measurements are based upon needs modifications, or if the tension can be attributed to errors in the methods. I wish to use Ia SNe to obtain the first measurement of the Hubble constant based on data from the Young Supernova Experiment.

Since the discovery of the accelerated expansion of the universe, astronomers have been trying to explain the cause of this phenomenon. The source of the acceleration has been dubbed Dark Energy due to its mysterious nature, but not much

is known about this force. Some scientists have tried to explain Dark Energy by a modification in the theory of gravity, making it important to investigate if the currently accepted cosmological model corresponds with observations. If this is not the case, these modified theories of gravity might be needed to explain Dark Energy. I aim to determine the linear growth using my sample of Ia SNe, as this observational quantity can help constrain theories and models when compared to their theoretical predictions.

Lastly, I will investigate if the two main LC fitting tools produce similar results, when applied to the same sample of SNe. As these programs are based on models, it is not unreasonable to think that one might perform better than the other. If one appears to produce better results, it might be worth considering which LC fitting tool to use in future work with Ia SNe.

In Section 1 I explain more about the background and motivation of the project. In Section 2 I describe the methods I have used to work towards the aim of the thesis. I present the results of the analyses in Section 3, and in Section 4 the results are discussed and put into a broader context. The main conclusions of the thesis are summarized in Section 5.

1.2 Measuring cosmological distances

Distances between objects in the universe have been notoriously difficult to measure throughout the history of astronomy. As there exists no option to directly measure distances to objects very far away, clever methods are needed to determine these. These methods are what makes up what is known as the cosmic distance ladder. The methods used in the cosmic distance ladder all wary in applicability, as they are limited by distance. As such, which method, or rung, of the cosmic distance ladder one has to use, depends on the object to investigate. The reason the cosmic distance ladder has gotten its name, is that each rung of the distance ladder is used to calculate the next. This succession of methods to determine distances to celestial objects are needed, as no single method can determine distances on all scales. However, this in turn means, that the distance measurements derived from the cosmic distance ladder are all dependent on the fact, that the prior steps are accurate.

1.2.1 Direct distance measurements: parallax, eclipsing binaries, and megamasers

On one of the lowest scales of the cosmic distance ladder, we find direct distance measurements. These are methods, with which we can obtain a direct distance measurement to an object, independent of other distances. These can thus be considered the base of the cosmic distance ladder.

To measure direct distances within our own galaxy, we often resort to the method of trigonometric parallax. If we observe a star at two different points, the position of the star will shift by an angle θ. The standard technique is to measure the shift in θ from the current position of the earth, compared to half a year later, using the distance from the Sun to the Earth as a baseline. The distance to the star will then be given by:

$$d = \frac{1}{p}$$

Where the parallax is $p = \theta/2$ in arcseconds, and d is the distance to the star in parsec. This formula holds, if the baseline we use for the triangle is 1 AU, i.e. the distance between the Earth and the Sun. Because we know the distance from the Earth to the Sun with great precision, the accuracy of the measurements using stellar parallax is limited only by how precisely we can measure θ. Because the parallax becomes smaller with greater distance, we can only use this method for relatively nearby objects. One of the most prominent uses of the parallax method, is to measure the distance to Cepheid variable stars (hereafter Cepheids) in the Milky Way. The main sources of parallax measurements are from the older Hipparcos satellite, and the newer actively observing Gaia space observatory.

Another method to obtain direct distance measurements, is by the use of eclipsing binaries. This method requires, that we are lucky to observe a binary system of stars with an orbital plane along our line of sight. As the stars undergo a full orbit, we will observe two decreases in the brightness of the binary system, corresponding to when the stars pass in front of each other with respect to us as observers. The width of these eclipses in combination with a measurement of the radial velocity of each star, will give us the size of each star. Stellar models can then give us a good estimate of the luminosity of the stars, which in combination with a measurement of their apparent magnitude will yield the distance to the system. This method is applied in [Pietrzyński et al., 2013], where they use cooler stars with accurate stellar models, to estimate the distance to the Large Magellanic Cloud to an accuracy of 2%.

Finally, megamasers can also provide a direct distance measurement. A megamaser

is a component of a galaxy which emits energy through intense radiation, typically in the microwave wavelength range. This happens because the component, for example a gas cloud, is experiencing stimulated spectral line emissions. Through interferometric observations of megamasers in accretion disks around supermassive black holes (SMBHs), these masers can act as tracers of the Keplarian motion about a point mass. Using the megamasers as tracers of position and velocity in combination with centripetal acceleration, the distance to the megamaser can be estimated. This is done in [Pesce et al., 2020], where they use water megamasers in the accretion disks of SMBHs to place constraints on the distance to and the mass of the SMBH.

1.2.2 Cepheid variable stars

On the next rung of the cosmic distance ladder, we can measure distances using Cepheids, building on the methods of direct distance measurements. Cepheids are luminous supergiant stars, which are pulsationally unstable. The main accepted theory for why Cepheids pulsate is the so-called 'κ-mechanism'. It is believed, that the helium in the outer layers of the Cepheid is the main driving force behind the process. At the dimmest part of a Cepheid's pulsation cycle, the outer layers of helium are doubly ionized. Doubly ionized helium is opaque, meaning that the radiation from the inner layers of the Cepheid can not escape. Because of this the temperature rises, which causes an expansion of the outer layers. Because of the expansion, the outer layers begin to cool, and the helium becomes less ionized, and therefore also less opaque. The radiation from the inner parts can now escape, increasing the luminosity of the Cepheid. As the cooling proceeds, at some point the radiation pressure will not be able to withstand the gravitational attraction of the Cepheid, resulting in a contraction. This then restarts the cycle of expansion and contraction. Because of this pulsation, the luminosity of Cepheids vary due to changes in their surface area and surface temperature.

Henrietta Leavitt found a correlation between the time of maxima in the observed brightness, denoted the period P, and the mean flux $\bar{f}$, averaged over one period [Leavitt and Pickering, 1912]. She found, that Cepheids which have the longest period also have the highest averaged flux. Using this correlation, we can calibrate Cepheids and use them as standard candles, if we can find the distance to a single Cepheid using one of the direct distance methods. A standard candle is a cosmological object that has a known absolute magnitude, which is related to the distance to the object. In reality, we use as many Cepheids as possible and not just a single Cepheid, as a greater sample yields a more accurate normalisation of the period-luminosity relation.

We can accurately measure the flux and periods of Cepheids out to a luminosity distance of $d_L \sim 30$ Mpc.

1.2.3 Surface brightness fluctuations

The method of using surface brightness fluctuations (hereafter SBF) for distance measurements was first proposed by [Tonry and Schneider, 1988]. The SBF used for distance measurements comes from the galaxy image of an early-type galaxy. In this image, there will be measureable fluctuations in its surface brightness due to the discreteness of the stars within the galaxy.

Imagine we have two identical galaxies, one placed at a distance of twice the other. The mean amount of stars in a pixel of the galaxy image N scales with the distance as $N \sim d^2$, and the flux scales with the distance as $f \sim d^{-2}$. The galaxy at twice the distance will contain four times as many stars in each pixel, but the mean amount of flux we would measure would also decrease by a factor of four, meaning the mean surface brightness that we would measure in every pixel of the image for each of the two galaxies would be the same. However, the root mean square between the pixels relative to the mean flux will scale as $RMS \sim d^{-1}$. This means, that the galaxy at twice the distance will appear twice as smooth in the galaxy image.

The amplitude of these fluctuations thus go with the distance as d^{-1}, and they can therefore be used as a distance indicator. The calibration of the zero point of SBF measurements, however, relies on a distance independent observable, such as Cepheids. SBF can be observed out to a distance of ~ 100 Mpc, which is further compared to the distance of ~ 30 Mpc for Cepheids, with an uncertainty of $5-10\%$ [Cantiello et al., 2018].

If we wish to find the distance to celestial objects further away, we need an even more luminous object, such as a SN.

1.2.4 Supernovae and type Ia

SNe are some of the most luminous events in the universe. The outcome of the SN and its properties are greatly dependent on the mass of the progenitor star.

For high mass stars, typically around $M > 8$ $M_\odot$, the SN is driven by a core collapse, as the outwards radiation pressure produced at the core of the star, can no longer withstand the inwards gravitational pressure caused by its own mass.

For medium mass stars, such as our sun, the process is quite different, and does not directly result in a SN. When the core of a medium mass star consists of carbon and oxygen, it does not have the required temperature and pressure to begin higher element fusion processes, contrary to the high mass stars. Due to mass ejection, its outer layers are stripped away, and what remains is a planetary nebulae, as well as the hot core consisting of carbon and oxygen. As there are no nuclear reactions in the core, it cools down and shrinks over time, settling to become what we know as a white dwarf.

The white dwarf does not keep decreasing in size however, as most of the electrons in the core are degenerate, which gives rise to electron degeneracy pressure. This degeneracy pressure arises, because the Pauli exclusion principle does not allow two identical half-integer spin particles, such as electrons, to occupy the same quantum state. As a result, a pressure will arise resisting compression of matter further. This does not mean, that the white dwarf can not end in a SN. If either a white dwarf in a binary system is able to accrete gas from the outer layers of the companion star, or two white dwarfs merge, the mass of the white dwarf will increase. As the mass of the white dwarf approaches what is known as the Chandrasekhar limit, which is a mass of $M \sim 1.4$ $M_\odot$, the increase in pressure of the interior of the white dwarf allows for the fusion of carbon. As a result, the temperature increases as well. Because the white dwarf is made of degenerate matter, it can not expand and cool, even though the temperature continues to increase. The result is a runaway process of reactions, eventually leading to a thermonuclear explosion of the white dwarf. This is what is known as a type Ia SN.

Observationally, type I SNe are classified by the absence of hydrogen emission lines in their spectra, and type Ia SNe are further classified by a Si $\lambda 6355$ absorption feature in their spectrum. The LCs of type Ia SNe are powered by the radioactive decay of ^{56}N to ^{56}Co.

1.2.5 Type Ia SNe as standard candles

Even though SNe are very luminous events, they do not usually allow for distance estimations. Under normal circumstances, there would be little way to tell if we were looking at a very dim nearby SN, or a very bright SN far away. However, because the process for a type Ia SN to occur is so specific, if we can identify a given SN as a type Ia, it fixes the mass and luminosity of the SN, allowing us to use it as a standard candle. This means, that we can assume any deviance from the expected brightness is due to the distance between the observer and the SN. The luminosity of a type Ia SN at peak brightness is about $L = 4 \times 10^9$ $L_\odot$. Thus,

for a moderately bright galaxy, the type Ia SN can outshine all of the other stars in the galaxy combined. Type Ia SNe have been observed at a redshift of $z \sim 2.5$, meaning we can use them as distance indicators to approximately this redshift [Rodney et al., 2014][Graur et al., 2014].

Because type Ia SNe can be used as standard candles, we can estimate the distance to all observed type Ia SNe, if we know the distance to just one. This means, that type Ia SNe can then also be used as the next rung of the cosmic distance ladder. The typical approach to calibrating the distance to Ia SNe, involves observing a SN in the same galaxy as a Cepheid. Because we can estimate the distance to the Cepheid using the lumniosity-period relation in a given galaxy, we can also estimate the distance to the SN. Like for the calibration of Cepheids, we use as big of a sample as possible of Cepheid and SN related events to calibrate the distance to a given SN. Once we have the distance to a type Ia SN, we can proceed to estimate the distance to any observed Ia SN without the need for a Cepheid calibration measurement in the galaxy, by comparing the observed luminosities of the two events. A prerequisite for this method is, that we observe a Cepheid and a Ia SN in the same galaxy, which is a rare occurrence. Because of this, the sample size of these calibration SNe is relatively small, and an important limiting factor in the precision to which we can estimate distances to other Ia SNe.

Because we know the expected luminosity of the Ia SN, we can also correct for the extinction of the emitted light. Extinction is the result of absorption and scattering of light, as it traverses through a medium. Dust causes a lot of extinction between an observer and the source, either by scattering or absorbing the light. It is therefore critical to account for extinction features, when working with cosmological observations.

1.3 Phillips Relation and color correction

Even though the theoretical expectation of the peak magnitude of all type Ia SNe should be roughly the same, due to the fact they stem from the same mechanism, this is not what is observed. Observations of galaxies in which Ia SNe occur, where the distances to the galaxies have been determined using Cepheids, show that Ia SNe do not always have identical peak magnitudes. In fact, the luminosity appears to vary from $L \approx (3-5) \times 10^9$ $L_\odot$.

This could pose a problem for the usability of type Ia SNe as standard candles, as there would then be no way to determine the absolute magnitude of a given SN with great certainty. This in turn means that there is no way of telling, if we are

looking at a Ia SN which happens to be very luminous, or if the distance to the SN is low.

It has been observed, however, that there is a correlation between the peak luminosity of Ia SN and its LC shape. This relation is known as the Phillips Relation, or the luminosity-decline relation, and was formulated by Mark Phillips in 1993 [Phillips, 1993]. Phillips observed nine Ia SNe in the B, V, and I bands, with relative distance measurements to their host galaxies. Correcting for the extinction, he was able to find a reasonable estimate of the absolute magnitude of the SNe. Using the absolute magnitudes and LCs of the SNe, Phillips noticed a strong correlation between the peak luminosity and the decline rate of the luminosity, with the steepest slope of the correlation in the B band, becoming progressively flatter in the longer wavelength bands V and I. The correlation Phillips noticed, is that the higher the absolute magnitude of a type Ia SN, the greater its decline rate. Phillips formulated the luminosity-decline relation as a correlation between the peak luminosity of the light curve, and, after some experimenting, the parameter Δm_{15}. This parameter is defined as the decline in the magnitude in the B band after 15 days. Phillips used Δm_{15}, as he found this parameter to provide the greatest discrimination.

In addition to a term relating the shape of the LC to its peak, the observed SN is also affected by a shift in color. As such, if we wish to use Ia SNe as standard candles, we need to correct for this color shift. This can be done by using a color correction parameter, which correlates the peak magnitude of the SN with its measured color. This was first done by [Tripp, 1997]. The shift in color usually comes from several factors and not a single place. This includes dust from the intergalactic medium, the interstellar medium of the host galaxy, as well as the intrinsic color of the SN. However, seeing as it makes no difference what the contribution from each source is if we want to correct for the total shift in color, the effects of these dust sources are all contained within a single parameter, denoted as R.

Thus, the use of type Ia SNe as standard candles can be recovered, despite fluctuations in the peak luminosity and a shift in color, if they are first calibrated using the associated corrections.

1.4 The Hubble Constant

The current standard cosmological model to describe the nature of our universe, is the Λ Cold Dark Matter model (hereafter ΛCDM). The ΛCDM model best

describes the data we observe, however the model is not without flaws. One of the most important parameters in our current understanding of the universe is the Hubble Constant, H_0. H_0 describes the Hubble flow, i.e. the expansion rate of the universe, which sets the distance scale. It is defined as:

$$H_0 = a^{-1}\frac{da}{dt}$$

when a, the scale factor of the universe, is $a = 1$.

Because H_0 is a central parameter in the ΛCDM model, it is of great interest to scientists to determine its value as accurately as possible. There are several ways to accomplish this, however especially two methods have gained popularity based on their applicability, and the precision to which they are able to measure the parameter.

The first method applies the ΛCDM model to describe early-universe physics, using fluctuations in the Cosmic Microwave Background (hereafter CMB) to produce a model consistent with what we observe. The model which best fit the overall data of the observed CMB spectrum in a flat ΛCDM universe, results in a value of $H_0 = 67.4 \pm 0.5$ km s^{-1} Mpc [Aghanim et al., 2020].

The second method uses observations of the late universe (the universe as it is today), to measure the distance-redshift relation from which we can obtain H_0. As described in Section 1.2, this method relies on building a distance ladder, which uses Cepheid calibrations of the luminosity to measure the distance to type Ia SNe. Using this method, [Riess et al., 2021] have measured a value of $H_0 = 73.2 \pm 1.3$ km s^{-1} Mpc.

The two methods, although different in nature, should agree on the final result of H_0. However, as can clearly be seen, they do not. This discrepancy in H_0 is known as the Hubble tension. The measurements are in clear disagreement at $\sim 4.2\sigma$, meaning it is very unlikely that it is due to random statistical effects that the measurements disagree. This also means, that beyond unlikely random statistical effects, there are two overall alternatives which can explain the Hubble tension:

(1) Hidden and currently unaccounted for systematic errors in the Planck or Riess determinations of H_0.

(2) The ΛCDM model is wrong and requires modification, because H_0 determined from the CMB depends on the assumed cosmological model.

As such, for the method using observations of the distance-redshift relation, it becomes important to build an increasingly larger sample size of Ia SNe, to verify the validity of the results, or obtain evidence to justify modification of the ΛCDM model. Observations from YSE of Ia SNe can help build this larger sample. In Section 2.4, I use the Ia SNe from YSE to estimate the Hubble constant.

1.5 The peculiar velocity field

Peculiar velocities are motions of objects which deviates from the general and homogeneous expansion of the universe, i.e. the Hubble flow. Peculiar velocities can be attributed to the fact that on scales smaller than $\sim$ 100 Mpc, the distribution of matter is not homogeneous, and they can therefore be used to trace this distribution. We can link peculiar velocities to perturbations in the density of matter, which can be used to constrain cosmological parameters describing the underlying matter distribution, which in turn describes the large scale structure of the local universe.

The cosmological principle states, that when viewed on a large enough scale, the distribution of matter in the universe is homogeneous and isotropic. However, formation of structures such as galaxies proves that, on smaller scales, this is not the case. It is believed, that these structures are the result of gravitational instabilities in the early universe. These small density deviations can be seen in the CMB, as they are coupled with the small temperature fluctuations we observe in the CMB today.

We can use linear perturbation theory to describe the relationship between the observed peculiar velocities of objects, and the mass density fluctuations on scales larger than $\sim$ 10 Mpc. On smaller scales than this, the linear theory breaks down and becomes inapplicable. The density perturbations are commonly characterized by the fractional difference, which we assume to be small:

$$\left|\delta(\mathbf{r})\right| = \frac{\rho - \bar{\rho}}{\bar{\rho}} \ll 1 \tag{1}$$

Where ρ is the density and $\bar{\rho}$ the mean density of the universe. The relationship between δ and the peculiar velocity field $\boldsymbol{v}(\boldsymbol{r})$ is given by:

$$\boldsymbol{v}(\boldsymbol{r}) = \frac{f(\Omega_m)}{4\pi} \int d^3\boldsymbol{r'} \delta(\boldsymbol{r'}) \, \frac{\boldsymbol{r'} - \boldsymbol{r}}{|\boldsymbol{r'} - \boldsymbol{r}|^3} \tag{2}$$

where $\boldsymbol{r}$ is measured in km s^{-1}. $f(\Omega_m)$ is the growth rate of density perturbations, with $f \approx \Omega_m^{\gamma}$, where $\gamma \approx 0.55$ for the ΛCDM model. However, this is assuming

that the currently accepted theory of gravity, the theory of General Relativity (hereafter GR), holds. For modified theories of gravity, γ might take on a different value, and hence measurements of peculiar velocities can also be used to constrain theories of gravity [Boruah et al., 2020].

This becomes especially relevant when trying to explain the accelerated expansion of the universe. The ΛCDM model attributes the acceleration to Dark Energy, which is included as a cosmological constant in the equations of GR. Because of this, GR also describes the growth of structure. Measuring the growth of structure is therefore of great importance, to confirm whether the predictions derived from the ΛCDM model and GR accurately describes the universe on large scales. If this is not the case, modified theories of gravity might be needed to explain the acceleration of the universe. One of the most prominent models of modified gravity is the $f(R)$ model [Linder, 2009]. This model can be challenging to distinguish from GR, as it can have an expansion history mimicking the ΛCDM model, yielding a similar redshift-distance relation. The two are however distinguishable by their prediction in growth of structure. The first step to determine if such modified theories of gravity are needed, is to check the consistency of the ΛCDM model.

According to the ΛCDM model, most of the matter in the universe is made up of dark matter. This means, that we can not observe most of the matter density contrast, and so to use Eq. 2, we must make an assumption about the distribution of matter relating to observations of galaxies. Galaxies can be thought of as high peaks of an underlying initially randomly distributed density field. We therefore assume, that we can trace the true distribution of the mass density field, using observations of the distribution of galaxies while accounting for the bias associated with these observations. Assuming linear biasing holds on large scales, we can relate the distribution of galaxies to the mass density distribution by:

$$\delta^g = b\delta$$

where b is the linear galaxy bias, defined as the ratio of the mean overdensity of galaxies to the mean overdensity of mass. This linear bias allows us to describe the relationship between the spatial distribution of galaxies and the underlying dark matter density field. Inserting this into Eq. 2, we can use it to predict peculiar velocities, where:

$$\beta = \frac{f}{b} \tag{3}$$

describes the relationship between gravitational acceleration and peculiar velocities [Carrick et al., 2015].

Under the assumption of linear biasing, we can write $b = \sigma_8^g/\sigma_8$, where σ_8 is the root mean square density fluctuation in a sphere of radius 8 h^{-1}Mpc. Inserting this into Eq. 3 yields:

$$\beta = \frac{f\sigma_8}{\sigma_8^g} \Rightarrow f\sigma_8 = \beta\sigma_8^g \tag{4}$$

where $f\sigma_8$ is what we measure, as a product of the linear growth and σ_8. We can measure σ_8^g directly from the distribution of galaxies, and so by estimating β from the peculiar velocity field, the cosmological parameter $f\sigma_8$ can be constrained.

Using the reconstructed density and radial velocity code from [Carrick et al., 2015][1], I construct Figure 1 showing the density field **(a)** and the radial velocity field **(b)** in the supergalactic plane. The distances these are based on are obtained in an iterative way in [Carrick et al., 2015]. First, they assume no peculiar velocity correction in the redshift-distance relation, and compute the density and peculiar velocity fields. Then, using this first estimate, they recalculate the distances, where the redshift-distance relation is now modified by peculiar velocities of the first estimate. Repeating these steps several times, their results converge to what they represent as the final estimate. At the center of both figures (0,0) is the Local Group, within which the Milky Way lies. Furthermore, several galactic superclusters have been marked, showing that several regions of overdensity corresponds with the position of these. Comparing the radial velocity field to the position of these superclusters, we can see that with respect to the local group, the radial velocities behave as we would expect them to. The superclusters gravitationally attract the matter in their vicinity, and so from our point of view, we will either see radial velocities around a supercluster receding from us or approaching us, corresponding to a Doppler redshift and a Doppler blueshift, respectively. Accordingly, the radial velocities have been marked either with red to indicate a Doppler redshift, or blue to indicate a Doppler blueshift. Overall, it is clear to see that the velocity field traces the underlying mass density distribution.

The observed redshift of a galaxy stems from a combination of peculiar velocity, and a recessional velocity due to the Hubble flow. To use peculiar velocities to constrain β, then, once needs to know the distance to the galaxy in order to separate these two components. The contribution from the Hubble flow component in a non-relativistic limit, $v \approx cz$, can be found by $v = Hr$. Type Ia SNe are great distance indicators, and can hence be used for this purpose.

[1]Publicly available: https://cosmicflows.iap.fr/

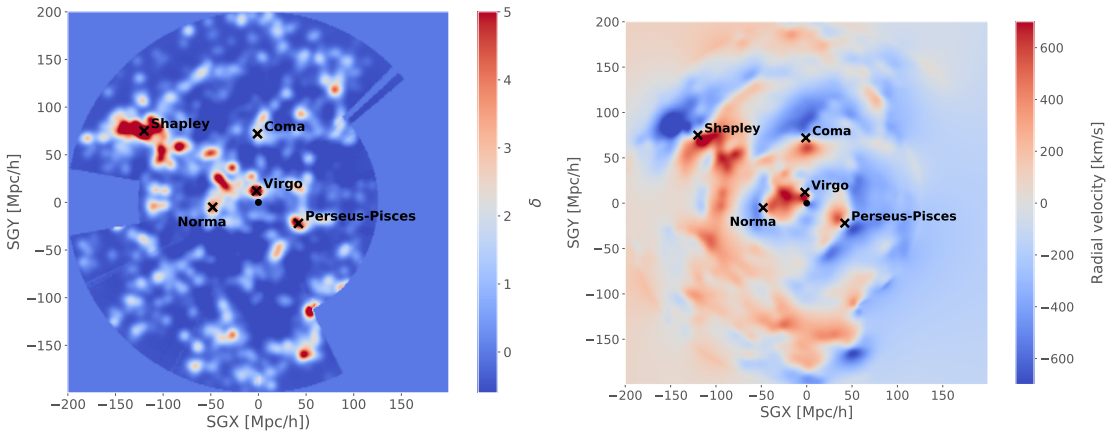

(a) **(b)**

Figure 1: The reconstructed density field **(a)** and radial velocity field **(b)** of galaxies within 200 h^{-1} Mpc from [Carrick et al., 2015] shown in galactic coordinates. The Local Group have been marked at (0,0) with a circle. The position of several superclusters near the Local Group is shown with an **x**.

1.6 The Young Supernova Experiment

The Young Supernova Experiment (hereafter YSE) is a three year long experiment, focused on discovering and following up transient astronomical events (hereafter transients). Transients are astronomical events whose duration are of varying length, but can range from hours to years. Transients are given their name due to the contrast in their timescales, when compared to the timescales of the evolution of galaxies, stars, and other long-time evolving astronomical objects. Transients include a wide range of objects, such as tidal disruption events, SNe, and more. YSE uses, at the time of writing, the telescope Pan-STARRS1 (hereafter PS1) to perform wide-field surveys of the sky, covering an area of 750 deg^2, taking up 7% of the total observation time of PS1. The use of wide-field surveys significantly increases the chance of discovering a transient, as transient events are unpredictable, meaning the greater an area surveyed, the greater the chances of discovering a transient. In time, YSE plans on using Pan-STARRS2 in their survey for transients as well, increasing the surveyed area to 1500 deg^2 [Jones et al., 2021].

Pan-STARRS observes through six broadband filters, $grizy_{\mathrm{P1}}$, but YSE uses only the $griz$ filters. PS1 can observe to a depth of $gri \approx 21.5$ mag and $z \approx 20.5$ mag, spanning a wavelength range of $3943.40 - 9346.00$ Å, up to a redshift of $z \approx 0.2$. YSE provides increased coverage in the iz bands, providing opportunities to observe transients at redder wavelengths. A lot of rare classes and subclasses of transients have low luminosity, are fast evolving, or are reddened. These rare

classes and subclasses include for example subclasses of type Ia SNe, tidal disruption events, and low-luminosity transients. Observing at longer wavelengths will allow YSE to increase the amount of rare transient discoveries. A reason it is preferable to observe at longer wavelengths, is due to the presence of dust between the observer and the transient. To minimize the effect of dust in the Milky Way, YSE avoids observations in the galactic plane.

Most importantly for this thesis, YSE will observe a great number of type Ia SNe. Because low redshift type Ia SNe can be used as probes for the large-scale structure of the universe, these are of great interest. A high amount of already made low-z Ia SNe observations are also subpar when compared to today's standards, as they were compiled in a time when the uncertainty on cosmological observations were not in the order of milli-magnitudes. As such, replacing these legacy observations with more precise measurements of Ia SNe are of great interest for studies making use of Ia SNe.

YSE will also be able to provide important data for future facilities. The Vera C. Rubin Observatory (previously named and hereafter denoted LSST), named after Vera C. Rubin who did pioneering work on galactic rotation rates, is expected to see first light in 2022. LSST will, among other things, observe the sky for transients like PS1, however it will not be able to produce a low-z sample of transients. This means LSST will have to rely on external low-z data sets, when making cosmological measurements. Furthermore, as time is of the essence when observing transients to determine potential followup observations or full LC classifications, there is a need to be able to identify interesting transients out of a large sample. YSE will be able to provide training data for machine learning algorithms aimed at identifying these rare transients. The multi-color LCs observed by PS1 and PS2 will be most useful to have in the training data, as there is a lack of coverage of LCs in the iz bands from other current time-domain surveys.

1.6.1 YSE-PrioritiZe

YSE-PrioritiZe (hereafter YSE-PZ) is a web-based application built on a MySQL database. The data from PAN-STARRS observations go through an extensive sorting process to find bona fide transients. This involves both machine learning algorithms trained on slow-moving asteroids to recognize 'good' objects, as well as a manual vetting process. If a transient is deemed real, it is sent to both the transient name server and YSE-PZ. YSE-PZ thus contains the data of what is deemed to be real transients from all of YSE. The data for every transient is available on its individual summary page.

YSE-PZ also ingests photometric data from other surveys. For example, the YSE survey tries to interleave observations with those of the Zwicky Transient Facility, increasing the ability to identify young transients. This can help to better visualize the LC of a given transient, because of the potential for an increase in photometric data when observations from the two surveys are combined.

To access large amounts of data, YSE-PZ makes use of a query explorer. In the query explorer, one can write an SQL script to sort YSE data by tags. By doing this, the user can construct their own table of data, containing specific parameters of interest for any transient included in the chosen tags.

2 Method

The data used in this thesis is from YSE-PZ. Because I want only data from type Ia SNe, the SQL script to gather the data from the query explorer includes a requirement, that a given transient has been spectroscopically classified as a type Ia SN. Also, the script includes the requirements, that the photometric data points are from YSE, and that an observation is made with the GPC1 camera of the PS1 telescope.

The data output from the script does not exclude data points from filters different from the desired *griz* filters. To make sure this data is not included in further analysis, further data filtration is done in Python, where measurements made with other filters are discarded. The Python script also removes measurements with no defined magnitude or error on the magnitude. Finally, the script sorts the measurements by time from earliest to latest, and outputs a file for each SN containing the necessary data for a LC fitting program to use it. After the initial data gathering process is complete, I have data from $N = 157$ spectroscopically classified Ia SNe.

2.1 Markov Chain Monte Carlo

The work in this thesis deals with fitting a wide range of models to different kinds of data sets, such as LCs of Ia SNe, estimation of H_0, peculiar velocity models etc. In all cases, I measure the model parameters using the Markov Chain Monte Carlo (hereafter MCMC) technique.

MCMC has become an increasingly used and preferred method in many aspects of science, when working with scientific inference. An increase in the availability of computational power over the last couple of decades, has allowed for the concept of Bayesian data analysis to become much more accessible. Bayesian theory is a theory to interpret data, allowing for prior knowledge of a given model together with the observed data, to constrain the parameters of a model. This is done by computing the probability distribution function, which have led to the outcome of the observed data. At the heart of Bayesian analysis is Bayes theorem. Bayes theorem tells us, that the posterior probability distribution is directly proportional to the product of the prior distribution and the likelihood distribution:

$$P\left(\Theta|D\right) \propto P(D|\Theta)P(\Theta) \tag{5}$$

Where $P\left(\Theta|D\right)$ is the probability of the model parameters being true given the observed data (called posterior), $P\left(D|\Theta\right)$ is the probability of observing the data given the model parameters (called likelihood, hereafter LH), and $P\left(\theta\right)$ is any knowledge we have of the model prior to obtaining the observed data (called prior).

It is generally rare that an analytical solution of the posterior is obtainable, however MCMC allows for estimation of the posterior distribution, by sampling from the distribution. This then allows for estimation of parameters within the model. The MCMC method consists of two parts, namely a Markov Chain and a Monte Carlo method.

A Markov Chain is a collection of states, where the next state depends only on the current state. The transition probability matrix between the states of a Markov Chain in a discrete space can be written as

$$K_{xy} = \text{Prob}\left(X_{n+1} = y \mid X_n = x\right) \tag{6}$$

An important property of a Markov Chain, is its ability to reach a stationary distribution. A stationary distribution is a distribution of states, in which the transition probability between all the states in the stationary distribution ensures, that the next state of the Markov Chain is also within the stationary distribution. In other words, if a Markov Chain reaches a stationary distribution, it will stay in this distribution. Thus, the aim is to engineer a Markov Chain, whose stationary distribution is the target distribution from which we wish to sample. The approach to accomplish this varies for different MCMC algorithms.

The Monte Carlo aspect of MCMC is from the fact that we simulate samples from a distribution. However unlike other methods to simulate samples from a distribution, such as the Accept-Reject method, MCMC takes the information of

its current position into account, which makes it more computationally efficient. Using the law of large numbers theorem, we can say that the expectation value of a function $g(\Theta)$ over a stationary distribution π will be given by the average value of the Markov Chain.

For this thesis, I use the python package emcee to perform MCMC, as it is a well-tested and efficient MCMC sampler Foreman-Mackey et al. [2013]. The algorithm of emcee is based on an affine-invariant ensemble sampling algorithm Goodman and Weare [2010]. The algorithm works by using a number of walkers chosen by the user, each exploring the parameter space to find the stationary distribution through an iterative process. The position of each walker is updated through every step of the iterations, by evaluation of the probability of a new proposed position. The reason for choosing to use several walkers (usually in the hundreds), is that if one is dealing with a multi-modal problem, some walkers might get stuck in local probability maxima. Using a large number of walkers ensures that the algorithm will still be effective, and the results accurate, even if some low number of walkers should get trapped in a local maxima. Furthermore, increasing the number of walkers does not increase the overall computation time needed to obtain a statistically significant sample, as if one doubles the amount of walkers, the amount of samples gained is also doubled. The number of steps a walker goes through before being in the stationary distribution, is not representative of the posterior distribution we wish to sample from. Because of this, one usually defines a 'burn-in' phase consisting of a number of initial steps, which are then disregarded when estimating the parameters of a function.

2.2 Fitting light curves

To estimate the parameters of a type Ia SN from its LC, I use a LC fitting tool. Currently, there are two dominant LC fitting tools used in the literature, namely the Spectral Adaptive Lightcurve Template (hereafter SALT2) [Guy et al., 2007], and SuperNovae in object-oriented Python (hereafter SNooPy) [Burns et al., 2010]. For the main analysis of the SNe from YSE, I choose to use SNooPy. This is because SNooPy has been trained on fast-declining Ia SNe, allowing for a better estimation of the parameter correlating the shape of a LC to its peak apparent magnitude.

SNooPy is a Python package which contains tools to fit the LCs of type Ia SNe, while also leaving a lot of freedom to the user regarding what to fit and how to do it. It contains several models to fit the LCs. For this thesis however, only the 'max model' is used, because this model is the only model which returns all of the parameters wanted for further analysis of the SNe. The max model does not

assume a relationship between the different filters one wants to fit, but instead fits the maximum brightness of each LC. This means, that unless specified otherwise, the model will return a maximum magnitude in the *griz* bands, assuming data is available in all these bands for each SN. Furthermore, the max model also returns the estimated time of peak magnitude characterized by the parameter T_{max}, and a parameter to describe the luminosity-decline relation.

Since Phillips' discovery of the luminosity-decline relation and his introduction of Δm_{15}, other parameters to describe the decline of a LC has also been suggested. Overall, the correction methods are entirely based on empirical evidence. An example of such empirical evidence, is whether the fit around the Hubble line in a Hubble diagram improves when the corrections are applied. An example of a Hubble diagram can be seen in Fig 8, where the Hubble line corresponds to the theoretical line in the figure.

SNooPy allows the user to choose between two parameters to describe the luminosity-decline relation, Δm_{15} and a *stretch* parameter (also called color-stretch) [Burns et al., 2014]. The stretch parameter is denoted s_{BV}, for example, when used to describe the B and V filters. For this thesis, I use the stretch parameter when using SNooPy. The stretch parameter works by comparing the observed rest frame LC to typical (normal) templates that the model uses, stretching the template LC to match the observed LC. This does mean, that the variability of these model templates can place a restrain on the observed stretch, as no model template will completely match with observed template. The different parameters describing the shape of the LC can be related through equations describing their correlation, however these are based on empirical evidence and not theoretical derivations.

In Section 2.4 I wish to estimate the Hubble constant, which requires calibration SNe. These calibration SNe have their data in the B and V filters. Because of this, I need to know the peak magnitude in the B and V filters for the YSE Ia SNe I use. Even though the photometric data from YSE is in the *griz* filters, SNooPy allows the user to select which filters they would like to fit the observed data to. This means, that after SNooPy has performed an initial analysis in the *griz* filters, I can choose other templates to which the data should be fit, which is done through a comparison of spectral templates. I fit the observed g band with a B band template, and the observed r band with a V band template. This will therefore give me B_{max} and V_{max}, corresponding to a peak apparent magnitude in the B and V filter. This procedure does mean, that I rely on good templates for the filters. I assume that the SN templates are complete enough, so that the filter transformations are safe. The results in all sections of this thesis are obtained us-

Table 1: The parameters obtained from fitting LC's using SNooPy and SALT2.

SNooPy	s_{BV}	$\sigma_{s_{BV}}$	B_{max}	$\sigma_{B_{max}}$	V_{max}	$\sigma_{V_{max}}$	T_{max}	$\sigma_{T_{max}}$	χ^2_{red}	
SALT2	x_1	σ_{x_1}	B_{max}	$\sigma_{B_{max}}$	c	σ_c	T_{max}	$\sigma_{T_{max}}$	χ^2_{red}	Cov

ing this conversion in filters, unless stated otherwise. The results of an alternative calibration, where I work with results from the g and r templates, can be seen in Section 3.4.

The standard fitting feature in SNooPy uses a Levenberg-Marquardt least-squares method to fit the LC. This is a method used to solve non-linear least squares problems, such as minimization problems in least squares curve fitting. This fitting procedure allows for initial estimates, or starting positions, of the parameters for further analysis. SNooPy has a built-in MCMC feature based on emcee, which I use to estimate the parameters of a LC. Thus, the results of the initial fit can be used for the starting positions of the walkers in emcee.

A problem when fitting anything observed at a redshift, is that the spectral energy distribution (SED) is shifted towards longer wavelengths. To account for this, SNooPy calculates K-corrections using SED templates from [Hsiao et al., 2007], which weigh in when estimating the maximum observed magnitude in each filter. Furthermore, SNooPy uses the right ascension and declination of a SN to correct for the effect of dust in the Milky Way, by using Schlegel maps [Schlegel et al., 1998].

The fit result of each SN is appended to a single file, containing all of the relevant information from the fit of every SN. A list of the appended parameters for both SNooPy and SALT2 can be seen in Table 1. The 'Cov' parameter in the SALT2 row represents the covariances between all of the other LC fit parameters. While SALT2 allows the user to directly obtain these, SNooPy does not. To get the covariance between the parameters from SNooPy, I manually calculate the covariances based on the tracefile of the walkers from the MCMC for each SN.

Before fitting the LCs with SNooPy, I had data from $N = 157$ SNe. After fitting, I am left with fit results of $N = 112$, excluding SN 2020xqb. This SN is discarded from all samples for further analysis. The reason for manually discarding this SN is explained in Section 4.1. This means, that 44 SNe were unsuccessful in fitting. The most likely reason a SN might not yield a successful fit is because of its LC. If there are too few measurements to define the LC, SNooPy will not be able to conclude anything about the shape, and hence the parameters, of the LC. How-

ever, even though a LC should only contain data after its peak magnitude (after T_{max}), SNooPy is still able to accurately reconstruct the LC and determine its defining parameters, provided it contains enough measurements. This is because the defining features of a type Ia SN are observable some time after its peak in magnitude. However, if the LC of a SN has been perturbed by the variability of its host galaxy, SNooPy will not be able to accurately reconstruct the LC of the SN, unless steps are taken to manually remove the noise in the measurements from the host galaxy. An example of this is SN 2020pki, whose photometric data and LC fit is shown in Figure A.1 in appendix A. It is clear that in all of the filters, the photometric data points have been exposed to noise. Manually accounting for the noise reveals, that 2020pki can be further classified as a 91bg-like Ia SN, which is a subclass of a type Ia SN. SNe within this subclass show a lower luminosity than we would expect when compared to the shape of their LC. 2020pki will be automatically excluded from the sample of SNe, due to requirements implemented on the SNe. This is explained in Section 2.3.2.

Two examples of LCs fit with SNooPy can be seen in Fig 2. As can be seen from **(a)**, SNooPy does not need to fit all of the data points of the LC. Some of the data points located a substantial amount of time after T_{max} does not need to be included in the fit, because they do not contribute much information to constrain the defining parameters of the LC.

2.3 Hubble diagram

A Hubble diagram is a figure showing the distance modulus μ as a function of redshift. Using the data obtained from fitting the Ia SNe with SNooPy, I can work towards creating such a plot for the YSE SNe. All of the redshifts for the SNe are from NED, and are in the restframe in which the CMB is isotropic.[2]

2.3.1 Measurements of redshift

The most accurate measurements of a SN redshift comes from a spectroscopically determined redshift of the spectrum of its host galaxy. It can then safely be assumed that the SN has the same redshift. The YSE-PZ summary page for a transient includes quick access to the Sloan Digital Sky Survey[3] and Nasa/IPAC Extragalactic Database[4] for the transient. From SDSS and NED, one can check

[2] https://ned.ipac.caltech.edu/velocity_calculator
[3] http://skyserver.sdss.org/dr16/en/home.aspx
[4] https://ned.ipac.caltech.edu/

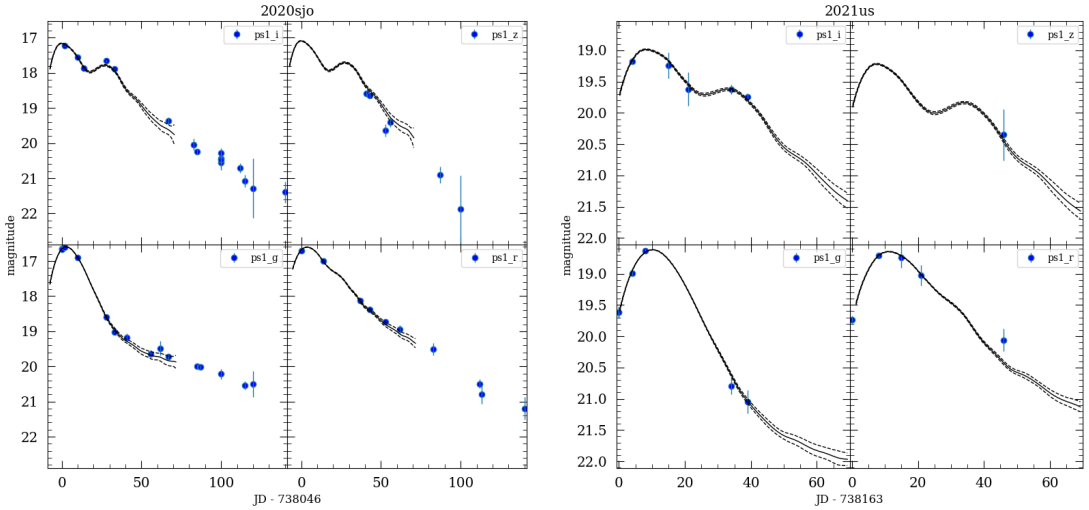

Figure 2: Examples of the *griz* filters of PS1 fit with SNooPy for **(a)** SN 2020sjo and **(b)** 2021us. The magnitude is plotted as a function of julian days (time). For both SNe, all the photometric data points are shown in their measured filters, while the PS1_g and PS1_r filters are fit with a B and V band template, respectively.

if the redshift of the transient is spectroscopically determined. The uncertainty of spectroscopically determined redshifts from the host galaxy spectrum can be of the order of $\sim 10^{-5}$, as seen in the SDSS redshift error of an objects optical spectra. It can thus be assumed to be negligible. Of the 112 SNe which were successfully fit with SNooPy, $N_{spec} = 55$ have a spectroscopically determined redshift from their host galaxy.

If we wish to use a Ia SN to constrain cosmological parameters, it is of great importance that we know its redshift to a high accuracy. If the uncertainty of the redshift is too great, it can cause a bias in the determination of cosmological parameters. In [Steinhardt et al., 2020], they use the Pantheon sample of Ia SNe to create two subsamples: a subsample containing only SNe with redshift measurements from their hosts, and a subsample containing only SNe with redshift measurements from their individual SN spectrum. They find, that the two samples yield statistically significant different best-fit cosmological parameters, including a difference of 2.5σ when measuring H_0. Because of this, they argue that combining two samples with different ways of obtaining the redshift for the SNe can be flawed, but the superior technique relies on redshift measurements obtained from the host. Although 2.5σ is not an extreme difference, because H_0 is a parameter we wish to determine very accurately, especially due to the present tension between measurements, it is

important to have a spectroscopically measured redshift of the host galaxy when measuring H_0.

In this section as well as in Section 2.4, I will use a sample consisting only of SNe with a spectroscopically measured redshift from the host galaxy. The impact on the results of including SNe without a redshift from the host galaxy, is explored in Section 2.5. Hereafter, 'Spec' is defined as the sample of SNe with spectroscopically determined redshifts from their hosts, and 'All' is defined as the full sample of SNe, including those which have their redshift measurement from their spectrum.

2.3.2 Ensuring the quality of the Ia SN sample

Even though a SN was fit successfully, it does not necessarily mean the quality of the fit is good. If SNe with fit values unrepresentative of the actual SN properties are included in a sample, it will skew the final results. To counteract this, quality cuts in the fit parameters are usually implemented to ensure the quality of the SN sample, as is done in [Betoule et al., 2014], [Riess et al., 2018], and [Khetan et al., 2020]. The cuts implemented on the samples used in this thesis, unless specified otherwise, are:

$$\begin{array}{lll} (1)\ -0.3 < \text{color} < 0.3 & & (2)\ -3 < x_1 < 3 \\ (3)\ \sigma_{T_{max}} < 2 & (4)\ \chi^2_{red} < 2 & (5)\ 0.02 < z \end{array} \quad (7)$$

In (2), x_1 is the term correlating the peak flux to the LC shape in the SALT2 LC fitting tool. x_1 can approximately be converted to the stretch parameter of SNooPy by:

$$x_1 = -0.006 + 5.98\,(s_{BV} - 1) - 5.55\,(s_{BV} - 1)^2 \quad (8)$$

Even though the correlation between x_1 and s_{BV} is strongest for $s_{BV} > 0.7$ [Burns et al., 2014], I will assume in this thesis that the equation holds for all of my SNe.

In (4), χ^2_{red} is the reduced chi-squared for the fit of the LC as a whole. Cut (5) is implemented because SNe at a redshift of $z \lesssim 0.02$ have their motion dominated by peculiar velocities, making their redshift measurements uncertain.

An example of a SN which failed multiple of these quality cuts, SN 2020onu, is shown in Figure 3. 2020onu failed cuts (1), (2), and (3). The sparse sampling with data only after the defining features of the actual LC means, that SNooPy has difficulties estimating T_{max}. This further leads to uncertainties in the peak

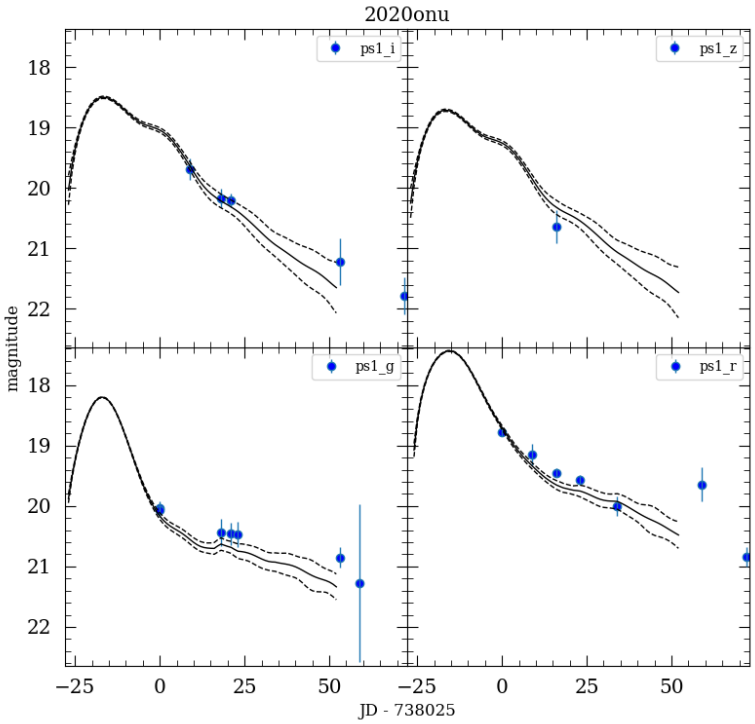

Figure 3: SNooPy's fit of the LC of SN 2020onu

magnitudes, and hence also the color and s_{BV}. These quality cuts are also the reason, that the previously mentioned 91bg-like Ia SN 2020pki was automatically discarded from the sample. SNe which belong to a subclass of type Ia SN will typically exhibit this deviance from normality in their LC parameters, and hence not pass the quality cuts.

After applying the quality cuts, the SN sample consists of $N = 30$ SNe. Plots of the cuts and how the remaining SNe are distributed with respect to these can be seen in Figure 4. The amount of SNe which fail to pass the different quality cuts, as well as the total number of discarded SNe, can be seen in Table 2. LC fits of the SNe are shown in appendix G.

2.3.3 Creating the Hubble diagram

As mentioned in Section 1.3, the peak luminosity of a type Ia SN varies. Because of this, they need to be standardized if they are to be used as standard candles. As such, we need to consider the stretch and color of a SN. The apparent peak magnitude in the B band is modeled as:

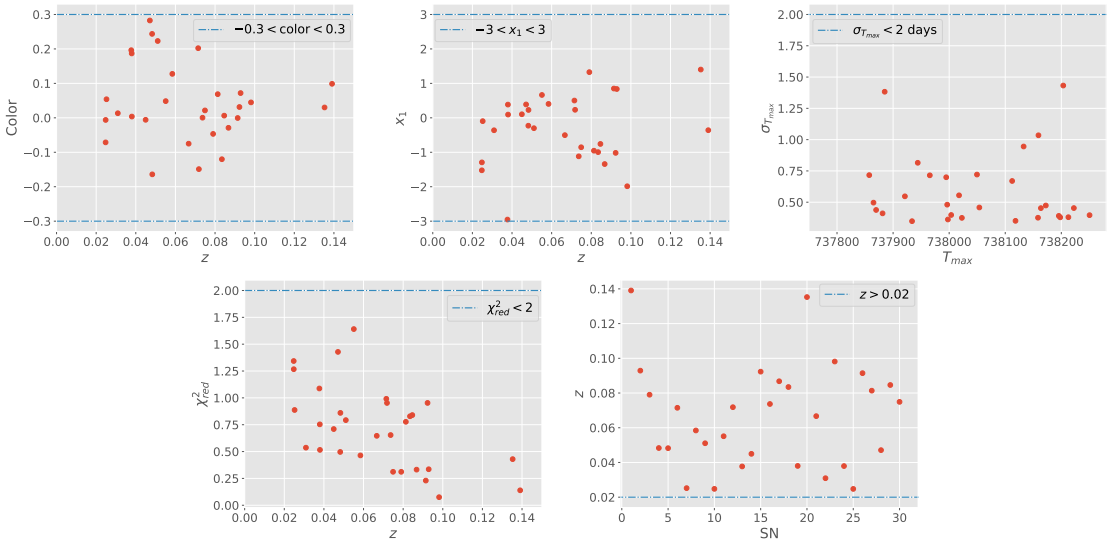

Figure 4: Distribution of the SNe in the Spec sample, after the quality cuts have been implemented. Each red dot represents a SN, where every subfigure contains $N = 30$ SNe.

Table 2: Amount of SNe which failed the different quality cuts. The 'Multiple' column depicts that a SN failed 2+ of the requirements. Because of this, the sum of **Quantity** adds up to more than the value of **Total**, as a SN can be counted in multiple columns.

Failed	Color	x_1	$\sigma_{T_{max}}$	χ^2_{red}	z	Multiple	**Total**
Quantity	9	7	7	9	9	14	**25**

$$m_B^T = P^0_{mod} + P^1 (s_{BV} - 1) + R (m_B - m_V) + \mu_{mod} \tag{9}$$

P^0_{mod} correlates the absolute magnitude of the SN to the apparent magnitude, P^1 correlates the stretch of the LC to its peak magnitude, and R correlates the peak magnitude with the color $m_B - m_V$.

The last term in Eq. 9, μ_{mod}, is a modified distance modulus, given by $\mu_{mod} = \mu(z) + 5\log_{10}(H_0)$. In a geometrically flat universe with a Robertson-Walker metric, the distance modulus can be defined to the second order as:

$$\mu(z) = 5\log_{10}\frac{cz}{H_0}\left[1 + \frac{1}{2}(1 - q_0)\, z - \frac{1}{6}\left(1 - q_0 - 3q_0^2 + j_0\right) z^2\right] + 25 \tag{10}$$

where $q_0 = -a\dot{a}^{-2}\ddot{a}$ is the deceleration parameter, described by the scale factor of the universe $a(t_0)$. $j_0 = a^2\dot{a}^{-3}\dddot{a}$ is the cosmic jerk, which describes when the universe went from being matter dominated to Λ dominated. For this thesis, I

have adopted the ΛCDM model best-fit values of $q_0 = -0.55$ and $j_0 = 1$ for these parameters. Even though this distance modulus is an approximation which requires an assumption about q_0 and j_0, the change that would be induced by varying these would be minimal [Dhawan et al., 2020]. As can be seen in Eq. 10, the distance modulus depends on H_0. This means, that if we wish to find the absolute value of $\mu(z)$, we need information to calibrate the zero point of the Ia SNe. The calibration usually comes in the form of Cepheids, as described in section 1.2.2. However, as I do not use any distance calibrators for now, I will have only the relative distances between the SNe, which means that I can not say anything about H_0. As such, H_0 enters into the measurement of P^0 as:

$$P^0_{mod} = P^0 - 5\log_{10}(H_0) \tag{11}$$

Having now defined the model of the apparent B band magnitude, m_B^T, the free parameters P^0_{mod}, P^1, and R can be estimated. To do so, I use a Bayesian inference model with a MCMC, as described in Section 2.1. The LH is usually considered in a log-likelihood form (hereafter LLH). There are several reasons for this. A few major reasons are, that it allows for addition instead of multiplication, and in the case of a Gaussian LH, it allows us to avoid computing the exponential. Both of these reasons save computational time, which for some problems can be of great importance. The prior of the model I use in the MCMC is flat, while the LLH is given by:

$$\ln \mathcal{L}_{cosmo} = -\frac{1}{2}\sum_{j=1}^{N_{SN}} \frac{\left(m_B^j - m_B^T\right)^2}{\sigma^2_{cosmo,j}} - \frac{1}{2}\sum_{i=j}^{N_{SN}} \ln 2\pi\sigma^2_{cosmo,j} \tag{12}$$

where m_B^j is the observed magnitude for each SN in the B band, and m_B^T is the modeled magnitude as given by Eq. 9. The variance σ_{cosmo}, with correlation between parameters denoted by C, is given by:

$$\sigma^2_{cosmo,j} = C_{(mb,mb),j} + P^{1^2}C_{(s_{BV},s_{BV}),j} + R^2C_{(c,c),j} - 2P^1C_{(m_B,s_{BV}),j} \\ -2RC_{(m_B,c),j} + 2P^1RC_{(s_{BV},c),j}$$

where the correlation terms containing the color can be expanded to produce correlation terms relating to the peak magnitudes in the B and V filters. Furthermore, an intrinsic scatter is added to the variance. The intrinsic scatter accounts for systematic uncertainties from effects not considered in the analysis, as well as potential peculiar velocities of the objects. Physically, it is the precision to which we can measure the distance modulus to a given SN with the model used. This parameter will also be estimated in the MCMC. This yields the formula for the cosmological variance of the sample:

$$\sigma^2_{cosmo,j} = \sigma^2_{m_B,j} + P^{1^2}\sigma^2_{s_{BV},j} + R^2\left(\sigma^2_{m_B,j} + \sigma^2_{m_V,j} - 2C_{(m_B,m_V),j}\right) - 2P^1 C_{(m_B,s_{BV}),j}$$
$$-2R\left(\sigma^2_{m_B,j} - C_{(m_B,m_V),j}\right) + 2P^1 R\left(C_{(s_{BV},m_B),j} - C_{(s_{BV},m_V),j}\right) + \sigma^2_{int} \tag{13}$$

Usually it is reasonable to assume that some of the correlation terms are negligible. For example, we would not expect $C_{(m_B,m_V)}$ which describes the correlation between magnitude measurements made in the B and V filter, to have a considerable contribution to the overall variance, as the filters should be independent. Even so, all of the correlations are included for completeness. The result of the MCMC can be seen in Figure 7.

Using the results of the MCMC, the Hubble diagram can now be created. By rearranging Eq. 9, we can obtain the modified distance modulus, corrected for the effects of stretch and color:

$$\mu_{mod} = m_B - P^0_{mod} - P^1(s_{BV} - 1) - R(m_B - m_V) \tag{14}$$

The uncertainty of μ_{mod} is given by σ_{cosmo} from Eq. 13. The results can be seen in Section 3.1.

2.4 Estimating H_0 with Ia SNe

As previously mentioned, we need distance calibrated SNe if we wish to estimate H_0, and this calibration can be performed by the use of Cepheids. One of the most prominent sample of Cepheids is the SH0ES sample [Riess et al., 2016]. This sample consists of 19 Ia SNe, all of which have measurements in the B and V filters. The fit values from SNooPy of the LCs from these calibration SNe, as well as the associated distance moduli and corresponding error, can be seen in Table 3.

To perform the calibration of the SNe, a LLH for the calibration sample needs to be implemented in addition to the cosmological LLH from Eq. 12. This LLH can be defined as:

$$\ln \mathcal{L}_{calib} = -\frac{1}{2}\sum_{i=1}^{N_{calib}} \frac{\left(m^i_B - m^T_B\right)^2}{\sigma^2_{calib,i}} - \frac{1}{2}\sum_{i=1}^{N_{calib}} \ln 2\pi\sigma^2_{calib,i} \tag{15}$$

Table 3: The best-fit parameters from SNooPy, and Cepheid estimated distance modulus, for the 19 Ia SNe from the SH0ES sample. μ_{ceph} is taken from Table 5 of [Riess et al., 2016].

Supernova	m_B [mag]	σ_{m_B} [mag]	m_V [mag]	σ_{m_V} [mag]	s_{BV}	$\sigma_{s_{BV}}$	μ_{ceph} [mag]	σ_μ [mag]
SN1981B	11.974	0.012	11.876	0.019	0.925	0.03	30.906	0.053
SN1990N	12.651	0.013	12.574	0.019	0.976	0.030	31.532	0.071
SN1994ae	13.066	0.013	12.933	0.019	1.124	0.030	32.072	0.049
SN1995al	13.342	0.019	13.173	0.024	1.077	0.044	32.498	0.090
SN1998aq	12.322	0.013	12.414	0.019	0.941	0.030	31.737	0.069
SN2001el	12.826	0.012	12.598	0.019	0.947	0.030	31.311	0.045
SN2002fk	13.206	0.012	13.209	0.019	1.189	0.030	32.523	0.055
SN2003du	13.494	0.012	13.55	0.019	1.017	0.03	32.919	0.063
SN2005cf	13.25	0.012	13.246	0.019	0.948	0.030	32.263	0.102
SN2007af	13.164	0.012	13.058	0.019	0.919	0.030	31.786	0.046
SN2007sr	12.744	0.018	12.569	0.020	1.026	0.031	31.290	0.112
SN2009ig	13.477	0.014	13.371	0.020	1.135	0.032	32.497	0.081
SN2011by	12.89	0.015	12.821	0.021	0.948	0.031	31.587	0.070
SN2011fe	9.931	0.012	9.947	0.019	0.936	0.030	29.135	0.045
SN2012cg	12.115	0.012	11.942	0.020	1.189	0.048	31.08	0.292
SN2012fr	11.977	0.012	11.943	0.019	1.121	0.030	31.307	0.057
SN2012ht	12.395	0.013	12.576	0.019	0.853	0.030	31.908	0.043
SN2013dy	12.756	0.013	12.553	0.02	1.131	0.032	31.499	0.078
SN2015F	12.823	0.012	12.696	0.019	0.866	0.03	31.511	0.053

where the variance of the calibration sample is:

$$\sigma^2_{calib,i} = \sigma^2_{\mu_{calib},i} + \sigma^2_{m_B,i} + P^{1^2}\sigma^2_{s_{BV},i} + R^2\left(\sigma^2_{m_B,i} + \sigma^2_{m_V,i} - 2C_{(m_B,m_V),i}\right) - 2P^1 C_{(m_B,s_{BV}),i} - 2R\left(\sigma^2_{m_B,i} - C_{(m_B,m_V),i}\right) + 2P^1 R\left(C_{(s_{BV},m_B),i} - C_{(s_{BV},m_V),i}\right) + \sigma^2_{int} \tag{16}$$

equal to that given by Eq. 13, except for the addition of a $\sigma^2_{\mu_{calib}}$ term, which comes from the uncertainty of the distance modulus obtained from the calibration. The total LLH will then be: $\ln\mathcal{L} = \ln\mathcal{L}_{calib} + \ln\mathcal{L}_{cosmo}$.

While Cepheids are a great tools for distance calibration, they are mostly found in late-type galaxies (spiral galaxies). Another way of calibrating distances are by the use of SBF, as described in Section 1.2.3. The SBF method is best used with stellar populations dominated by evolved stars, meaning early-type galaxies (elliptical galaxies) are ideal for SBF measurements.

There are several advantages to SBF calibrations [Khetan et al., 2020]. For example, the use of late-type galaxies for distance calibration means, that we need to make fewer corrections for dust, as the more evolved galaxies usually contain less dust. The distance to which we can observe SBF is also considerably greater than that of Cepheids. Furthermore, the observational aspects of SBF are also easier when compared to Cepheids, as they require only a galaxy image, and not high resolution stellar photometry or periodic observations of the galaxies in which the Cepheids are located.

Table 4: The best-fit parameters from SNooPy and SBF estimated distance moduli for the 26 Ia SNe. μ_{SBF} is taken from Table 2 of [Khetan et al., 2020], except for SN1981B and SN1991T, which was provided to me by Luca Izzo from DARK.

Supernova	m_B [mag]	σ_{m_B} [mag]	m_V [mag]	σ_{m_V} [mag]	s_{BV}	$\sigma_{s_{BV}}$	μ_{SBF} [mag]	σ_μ [mag]
SN1970J	14.868	0.013	14.62	0.020	0.916	0.030	33.582	0.151
SN1980N	12.460	0.012	12.335	0.019	0.848	0.030	31.590	0.050
SN1981B	11.974	0.018	11.877	0.020	0.925	0.038	31.090	0.050
SN1981D	12.487	0.048	12.327	0.046	0.852	0.051	31.590	0.050
SN1983G	12.804	0.015	12.621	0.020	1.189	0.030	31.920	0.197
SN1991T	11.589	0.012	11.402	0.019	1.189	0.030	31.090	0.050
SN1992A	12.531	0.012	12.501	0.019	0.777	0.030	31.632	0.075
SN1992bo	15.761	0.013	15.748	0.019	0.715	0.031	34.270	0.150
SN1994D	11.770	0.012	11.828	0.019	0.785	0.030	31.320	0.120
SN1995D	13.386	0.014	13.256	0.019	1.259	0.031	32.600	0.150
SN1996X	13.076	0.013	13.081	0.019	0.893	0.030	32.260	0.190
SN1997E	15.174	0.013	15.082	0.020	0.795	0.031	33.500	0.150
SN1998bp	15.371	0.014	15.073	0.020	0.600	0.032	33.100	0.150
SN2000cx	13.135	0.012	13.070	0.019	0.907	0.030	31.922	0.212
SN2003hv	12.456	0.015	12.545	0.020	0.766	0.030	31.566	0.304
SN2006dd	12.271	0.014	12.288	0.020	0.951	0.031	31.590	0.050
SN2007on	13.048	0.013	12.933	0.019	0.568	0.031	31.526	0.072
SN2008Q	13.459	0.014	13.512	0.019	0.805	0.032	31.922	0.212
SN2011iv	12.449	0.013	12.393	0.020	0.659	0.031	31.526	0.072
SN2012cg	12.114	0.012	11.942	0.020	1.188	0.052	31.020	0.180
SN2012fr	11.976	0.012	11.943	0.019	1.121	0.030	31.510	0.030
SN2014bv	14.045	0.030	13.824	0.029	0.598	0.044	32.190	0.494
SN2015bp	13.703	0.023	13.669	0.029	0.690	0.038	31.737	0.315
SN2016coj	13.205	0.017	12.983	0.020	0.884	0.031	31.922	0.258
SN2017fgc	13.621	0.013	13.346	0.0190	0.958	0.030	32.536	0.133
SN2018aoz	12.515	0.013	12.590	0.0190	0.841	0.030	31.795	0.101

As previously mentioned, however, the SBF measurements used in this thesis all

have their zero point calibrated using Cepheids. This means, that the SBF calibrations does not offer an independent method of measuring distances, but it is rather a complimentary method to Cepheids. The SBF method is still very useful however, as it allows for an increase in calibration measurements, which is much needed when working with Ia SNe. The SBF calibration sample consists of 26 Ia SNe.
The data for the LCs of the Ia SNe in the SH0ES and SBF sample was graciously provided to me by Luca Izzo from DARK. As I have the data defining the LCs, I can fit the two calibration samples using SNooPy to get the LC parameters. The SNooPy fit parameters for each SN and its associated distance modulus can be seen in Table 3 for the SH0ES sample, and in Table 4 for the SBF sample.

For both Table 3 and 4, the uncertainties of all the individual fit parameters for all of the SNe are very similar. For such well-defined LCs as these calibration SNe have, there is a very low statistical uncertainty associated with the parameters. However, the systematic uncertainty that SNooPy estimates for each parameter must also be taken into account, which is why the errors are so similar. The systematic uncertainty dominates the error budget, as it is usually several times greater than the statistical uncertainty for these SNe. The systematic error is insensitive to the quality and quantity of the data in a LC. It comes from the fact that the LC templates SNooPy uses, are not in perfect correspondence with the observed data we wish to fit, and so when comparing these it gives rise to the error. This is why all uncertainties for the individual parameters are very similar.

It should be noted, that the SH0ES and SBF samples I use share three SNe, meaning the samples are not completely independent. Even though the Ia SNe in the two samples are mainly from different types of galaxies, the scale of the morphology on which a galaxy is characterized is not discrete, meaning there is room for overlap.

As I now have means to determine an absolute value of the distance modulus from Eq. 10 for the YSE SNe, I can estimate H_0 using MCMC. The procedure resembles that of Section 2.3.3, except H_0 is now left as a free parameter instead of being contained within P^0_{mod}. The result of the MCMC using the SH0ES sample and the SBF sample can be seen in Section 3.2.

2.5 Exploring redshift uncertainty

As mentioned in Section 2.3.1, the accuracy to which we know the redshift of a Ia SN plays a big role with regards to its usability. If no spectrum of the host galaxy is available, we must then resort to other methods to determine the redshift.

A way to get an estimate of the redshift, is to look at the spectrum of the SN itself and use a cross-correlation technique [Blondin and Tonry, 2007]. The way this is performed, is by comparing the observed SN spectrum to a SN spectrum of a known type and age at zero redshift. A wavelength scaling quantity involving the redshift of the observed SN is then determined, based on the value which maximizes the cross-correlation between the two SN spectra. This can allow for redshift estimations with errors of the order $\sigma_z \lesssim 0.01$. While a small part of the error might come from motions associated with the galaxy within which the SN is, the largest part of the error stems from the templates used to compare the observed SN spectrum. These templates are not perfect, and finding a template which closely matches the observed SN spectrum can be difficult, thus resulting in errors on the redshift.

To investigate this error for the SNe without spectroscopically measured redshifts in my sample, I use the All sample of Ia SNe from YSE. An updated plot showing the distribution of the SNe after performing the quality cuts from Eq. 7 can be seen in Figure 5. A table showing the numbers of discarded SNe from each cut can be seen in Table 5. This All sample consists of $N = 64$ SNe.

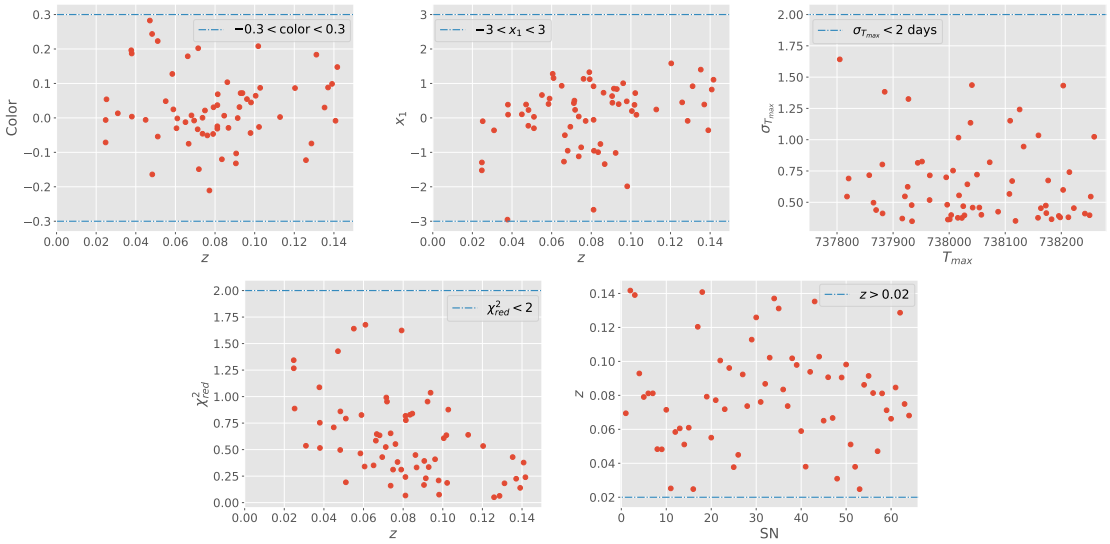

Figure 5: Distribution of the full sample of SNe passing the quality cuts. Each red dot represents a SN, where every subfigure contains $N = 64$ SNe

To estimate the error associated with the redshift, it can be included as a parameter in the MCMC. σ_z is entered into the total variance by error propagation. The new variance then becomes:

Table 5: Amount of SNe which failed the different quality cuts for the full SNe sample. The 'Multiple' column depicts, that a SN failed 2+ of the requirements. Because of this, the sum of **Quantity** adds up to more than the value of **Total**, as a SN can be counted in multiple columns.

Failed	Color	x_1	$\sigma_{T_{max}}$	χ^2_{red}	z	Multiple	**Total**
Quantity	15	9	18	15	9	19	**48**

$$\sigma^2_{cosmo,j} = \sigma^2_{m_B,j} + {P^1}^2\sigma^2_{s_{BV},j} + R^2\left(\sigma^2_{m_B,j} + \sigma^2_{m_V,j} - 2C_{(m_B,m_V),j}\right) - 2P^1C_{(m_B,s_{BV}),j}$$
$$- 2R\left(\sigma^2_{m_B,j} - C_{(m_B,m_V),j}\right) + 2P^1R\left(C_{(s_{BV},m_B),j} - C_{(s_{BV},m_V),j}\right) + \sigma^2_{int} + \left(\frac{d}{dz}\,\mu(z)\,\sigma_z\right)^2 \tag{17}$$

where the last term involving the uncertainty of the redshift is only applied, when a SN does not have its redshift from the host. The results of using the All sample and estimating σ_z can be seen in Section 3.3.

2.6 Peculiar velocities as tracer of mass density

To use peculiar velocities as probes for the underlying density fields requires as broad and deep a catalogue of galaxies as possible. [Carrick et al., 2015] uses the 2M++ galaxy catalogue to reconstruct the density and radial velocity fields out to a redshift of $z \sim 0.07$. Using the reconstructed density and radial velocity fields, we can compare the velocity field predictions to observed peculiar velocity data, which can be measured via. distance indicators such as type Ia SNe. This in turn allows us to estimate cosmological parameters.

I use the model from [Carrick et al., 2015], which is computed for a fiducial ΛCDM model with $f\sigma_{8,\mathrm{lin}} = 0.401 \pm 0.024$. When using peculiar velocities to infer σ_8, it is sensitive to potential non-linear evolution. This non-linear evolution has been corrected for, in order to be able to compare $f\sigma_8$ to other results obtained at higher redshift. Comparing this model to the SN data from YSE, I can effectively determine the $f\sigma_{8,\mathrm{lin}}$ via. the amplitude of peculiar velocities.

To perform the comparison, I use a Forward likelihood method [Pike and Hudson, 2005]. The Forward LH method compares the predicted redshift of a galaxy to the observed redshift, and maximizes the probability of a galaxy having the observed redshift. As mentioned in Section 1.5, the observed redshift of an object has a

contribution from the recessional velocity and from peculiar velocities. We can use this to define the predicted redshift as:

$$1 + z_{pred} = \left(1 + z_{cos}(\boldsymbol{r})\right)\left(1 + \frac{1}{c}\left(\gamma \boldsymbol{v} + \boldsymbol{V}_{\text{ext}}\right)\hat{\boldsymbol{r}}\right) \tag{18}$$

where the reconstructed velocity and flow model is represented by the second term. $\boldsymbol{v}$ is the peculiar velocity prediction from the reconstruction, and $\boldsymbol{V}_{\text{ext}}$ is a residual bulk flow, which contains contributions to the peculiar velocity from structures outside of the 2M++ redshift surveys volume. The γ that is measured using this method is a rescaling factor of the fiducial β value estimated in [Carrick et al., 2015]. It is not to be confused with the $\gamma \approx 0.55$ from the power of Ω_m for the ΛCDM model, as these are totally unrelated quantities.

The cosmological redshift, z_{cos}, can to a second order approximation be defined as:

$$z_{cos} = \frac{1}{1 + q_0}\left[1 - \sqrt{1 - \left(\frac{2H_0 r}{c}\right)(1 + q_0)}\right] \tag{19}$$

where instead of H_0, I use the dimensionless Hubble parameter h, which is set to be $h = H_0/\left(100 \text{ km s}^{-1} \text{ Mpc}^{-1}\right)$. r is the distance to the object for which to predict the redshift. For the highest redshift I use in the approximation ($z = 0.07$), the uncertainty introduced by neglecting higher order terms is ~ 21 km s^{-1}, which is much smaller than the precision of the peculiar velocity model.

The Forward LH method also corrects for inhomogeneous Malmquist bias. Malmquist bias is an observational effect which leads to a preference of detection of bright objects. The inhomogeneity arises from the fact, that on scales of ~ 100 Mpc the density distribution of matter in the universe is not homogeneous. To correct for the inhomogeneous Malmquist bias requires integrating along our line of sight to the boundary of the 2M++ survey. This takes the inhomogeneities into account, which are given by the reconstructed density field.

In addition to fitting for the flow model, we can jointly fit for the parameters calibrating type Ia SNe from the distance indicator [Boruah et al., 2020]. With the distance indicator parameters $\Theta = (P^0, P^1, R)$, the probability of observing a SN at redshift z_{obs} in the Forward LH method is given by:

$$P\left(z_{obs}|\boldsymbol{v}, \boldsymbol{V}_{\rm ext}, \gamma, \Theta\right) = \int_0^\infty dr P(z_{obs}|r, \boldsymbol{v}, \boldsymbol{V}_{\rm ext}, \gamma) P(r|\Theta) \tag{20}$$

where $P(z_{obs}|r, \boldsymbol{v}, \boldsymbol{V}_{\rm ext}, \gamma)$ is given by:

$$P(z_{obs}|r, \boldsymbol{v}, \boldsymbol{V}_{\rm ext}, \gamma) = \frac{1}{\sqrt{2\pi\sigma_v^2}} \exp\left(-\frac{\left(cz_{obs} - cz_{pred}\right)^2}{2\sigma_v^2}\right) \tag{21}$$

σ_v is the uncertainty in the peculiar velocity from non-linear perturbations. This is assumed to be $\sigma_v = 150$ km s^{-1} as found in [Carrick et al., 2015] by comparison of N-body simulations.

$P(r|\Theta)$ is the radial distribution, and is assumed given by:

$$P(r|\Theta) = \frac{1}{N(\Theta)} r^2 \exp\left(-\frac{\left[\mu(r) - \mu(\Theta)\right]^2}{2\sigma_\mu^2(\Theta)}\right)\left[1 + \delta^g(\boldsymbol{r})\right] \tag{22}$$

where $N(\Theta)$ is a normalization term to normalize the probability, $\sigma_\mu(\Theta)$ is the error in the distance modulus of the tracer, i.e. Eq. 13, and $\delta^g(\boldsymbol{r})$ is the overdensity in the galaxy field from the reconstruction of the density field. $\mu(r)$ is computed as:

$$\mu(r) = 25 + 5\log_{10}(d_L)$$

where d_L is the luminosity distance given by: $d_L = r(1 + z_{pred})$.

As can be seen Eq. 18, γ is obtained by comparing the observed velocity field data that I have from YSE to the model of [Carrick et al., 2015], by scaling their velocity field. The γ that I obtain can therefore be thought of as an indirect measurement of β from Eq. 3. γ can be converted to constrain $f\sigma_{8,\rm lin}$ by the relation:

$$\gamma = \frac{f\sigma_{8,\rm lin}}{f\sigma_{8,\rm lin,(Carrick)}} \tag{23}$$

Hereafter, the linear growth I obtain will be written as $f\sigma_8$, with the implicit understanding that non-linear evolution has been accounted for, and so I will omit from specifically denoting this.

MCMC can now be used to estimate the rescaling factor γ, external bulk flow $\boldsymbol{V}_{\rm ext}$, and the global parameters, by sampling from Eq. 20. I do this using the SNe from YSE, but also with a combined sample of YSE and the Foundation sample [Jones et al., 2019]. The results can be seen in Section 3.5.

2.7 Comparison of SALT2 and SNooPy

When measuring the distance-redshift relation using calibration Ia SNe, a big part of the error budget is attributed to the process of the calibration itself, as can be seen in Table 7 of [Riess et al., 2016]. While this may be reasonable, there is little knowledge of how using different light curve fitting tools impacts the fit results of the observed LC's, and hence the cosmological analysis. As mentioned in Section 2.2, there are two dominant LC fitting tools, namely SALT2 and SNooPy. To compare them, I implement the SALT2 LC fitting tool using the Python package sncosmo[5].

While two of the parameters SNooPy takes as inputs are the observed magnitude and observed magnitude error, SALT2 equivalently takes the observed flux and observed flux error. The conversion between apparent magnitude and flux is given by:

$$m = -2.5 \log_{10}(f) + zp \Rightarrow f = 10^{\frac{zp-m}{2.5}} \tag{24}$$

where f is the flux. zp is the zero point, which sets a conversion between the provided fluxes and the actual magnitude. For PS1, I adopt a zero point of $zp = 27.5$ for all filters. The uncertainty on the flux is given by:

$$dm = \frac{2.5}{\ln(10)} \frac{df}{f} \Rightarrow \sigma_f = \frac{\ln(10)}{2.5} \frac{f}{\sigma_m} \tag{25}$$

Examples of SALT2 fits can be seen in Figure 6. For comparability, the figure shows the same two SNe as in Figure 2. The observed PS1_g and PS1_r bands have again been fit with a B and V template, respectively. The B and V filter bands used by SNooPy are from the Carneige Supernova Project[6]. I implement these into my application of SALT2, so that the two LC fitting tools fit the LCs with the same bands.

The SALT2 model I use to perform the fits covers a wavelength range of $2500-8000$ Å [Guy et al., 2007], which is why the fit suddenly cuts off at a specific point in **(a)**. There is however still enough information to determine the defining features of the LC.

To correlate the peak of a LC to its shape, SALT2 uses the x_1 parameter, which can be correlated to the color-stretch parameter of SNooPy by Eq. 8. Because of this, the modeled apparent B band magnitude for a SN given by the SALT2

[5] https://sncosmo.readthedocs.io/en/stable/
[6] https://csp.obs.carnegiescience.edu/data/filters

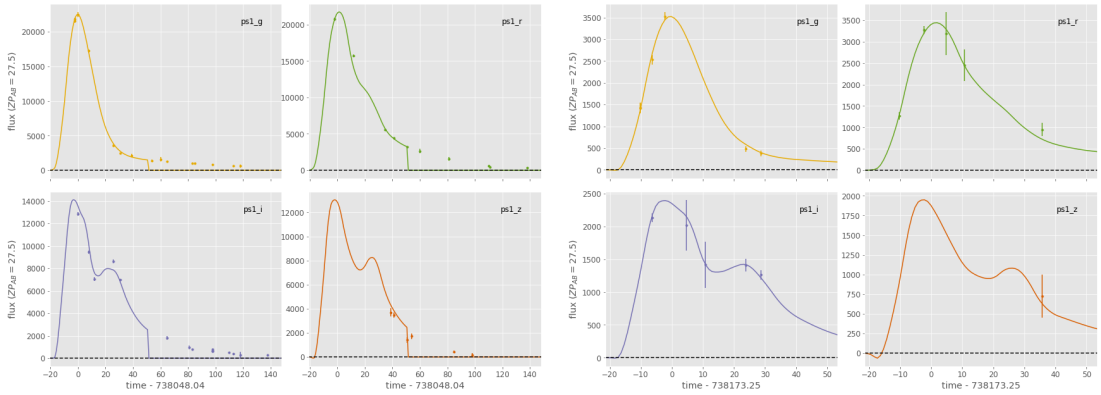

(a) **(b)**

Figure 6: Examples of the *griz* filters of PS1 fit with SALT2 for **(a)** 2020sjo and **(b)** 2021us. The g and r bands have been fit with a B and V band template, respectively.

parameters is not the same as I use for SNooPy, but rather it is given by the Tripp formula [Tripp, 1997]:

$$m_B = M - \alpha x_1 + Bc + \mu \tag{26}$$

where c is the color of the SN, and M and μ becomes equivalent to P^0_{mod} and μ_{mod}, respectively, if there are no zero point calibrations performed. The letter denoting the color correction term in the Tripp formula is usually written as β, however to avoid confusion with the β parameter related to the model of peculiar velocities, this color correction term is instead written as B.

The variance of the distance modulus using SALT2 parameters is given by:

$$\sigma^2_{cosmo,j} = \sigma^2_{m_B,j} + \alpha^2\sigma^2_{x_1,j} + B^2\sigma^2_{c,j} + 2\alpha C_{(m_B,x_1),j} - 2BC_{(m_B,c),j} \\ -2\alpha BC_{(x_1,c),j} + \sigma^2_{int} \tag{27}$$

I use SALT2 to perform a similar analysis of the global parameters of the Ia SNe from YSE, as described in Section 2.3.3. The results of the comparison can be seen in Section 3.6.

3 Results

3.1 Standardization of Ia SNe and the Hubble diagram

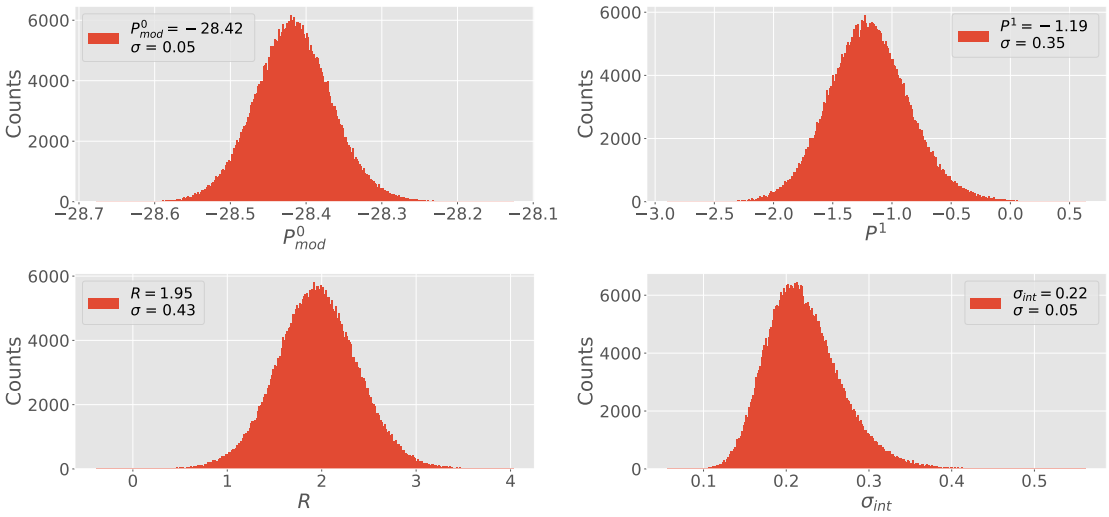

Figure 7: Estimation of the four parameters from Eq. 9 using MCMC in the BV filters. The mean value and standard deviation of the distribution for each parameter is shown in the legend.

The estimation of the parameters included in the modeled apparent magnitude in Eq. 9 obtained using MCMC can be seen in Figure 7. Using these values for P^0_{mod}, P^1, R, and σ_{int} in combination with Eq. 14, I can create the Hubble diagram. The result is shown in Figure 8. When accounting for the effects of stretch and color in every SN measurement, the errors become visually bigger in **(b)**, as we would expect.

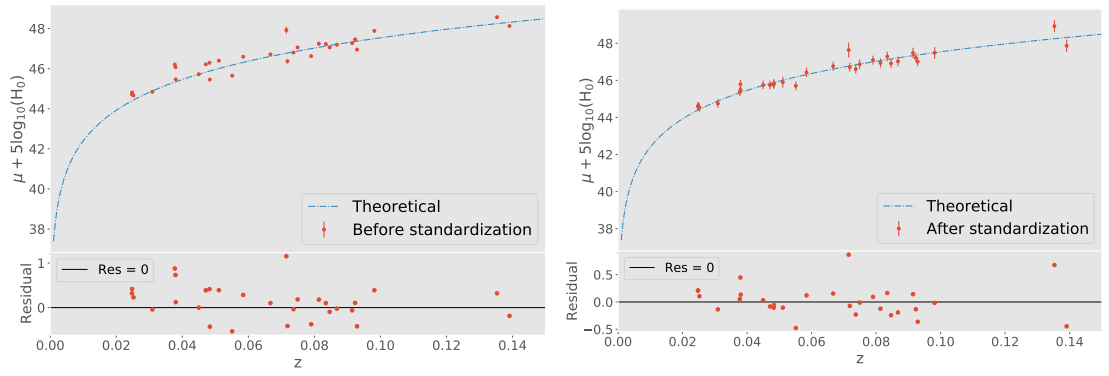

(a) **(b)**

Figure 8: Hubble diagram for the $N = 30$ SNe which pass the quality cuts, and has a redshift from their host. For both plots, a theoretical expectation line has been plotted. **(a)** shows the distribution before standardization, and **(b)** shows the distribution after standardization.

We expect the scatter around the theoretical prediction to decrease after standard-

ization, and for the scatter to be normally distributed around a value of zero. To confirm this is the case, Figure 9 shows a histogram comparing the scatter before and after standardization. The scatter visually decreases, although it can be hard to justify this is the case due to the low sample size. However, as can be seen in the legend, $\sigma_{after} < \sigma_{before}$, which is in alignment with expectations, confirming the decrease in the scatter. The exact values for all of the estimated parameters and the residuals are shown in Table 7.

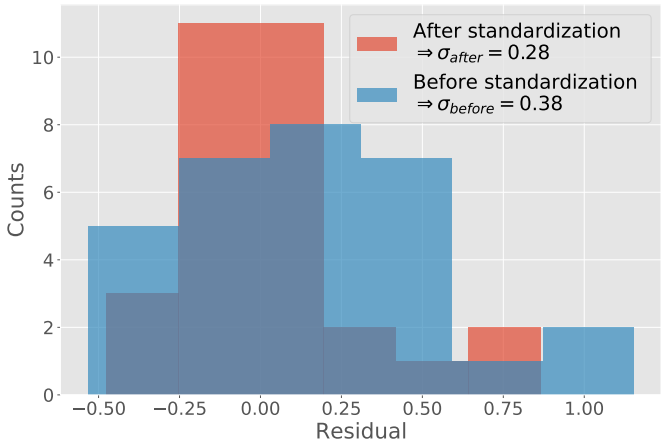

Figure 9: Histogram of the residual distribution before and after standardization. The histogram contains of $N_{\text{bins}} = 6$ bins, with the value of the standard deviation for each distribution in the legend. σ_{after} includes both the measurement errors and σ_{int} for the Spec sample seen in Table 7.

As can be seen in both Figure 8 and 9, there are some outliers for which the standardization does not have a big impact. A reason a SN might not be receive more of a correction to its apparent magnitude from the standardization process, can be because of the uncertainties on the parameters from its LC fit. If a SN has large uncertainties on its LC parameters, it will not contribute a large amount to constrain the global parameters from the MCMC fit. This results in less of a correction after standardization. This in combination with the needing a large correction to align with the theoretical expectation, can result in outliers.

3.2 H_0 estimation with SNooPy

As described in Section 2.4, H_0 can be measured by leaving it as a free parameter in the MCMC, if we use distance calibration measurements. As I have the data defining the LCs of these calibration measurements from Table 3 and 4, I now estimate H_0 using first the SH0ES sample. The result of the Cepheid calibrated

H_0 measurement can be seen in Figure 10.

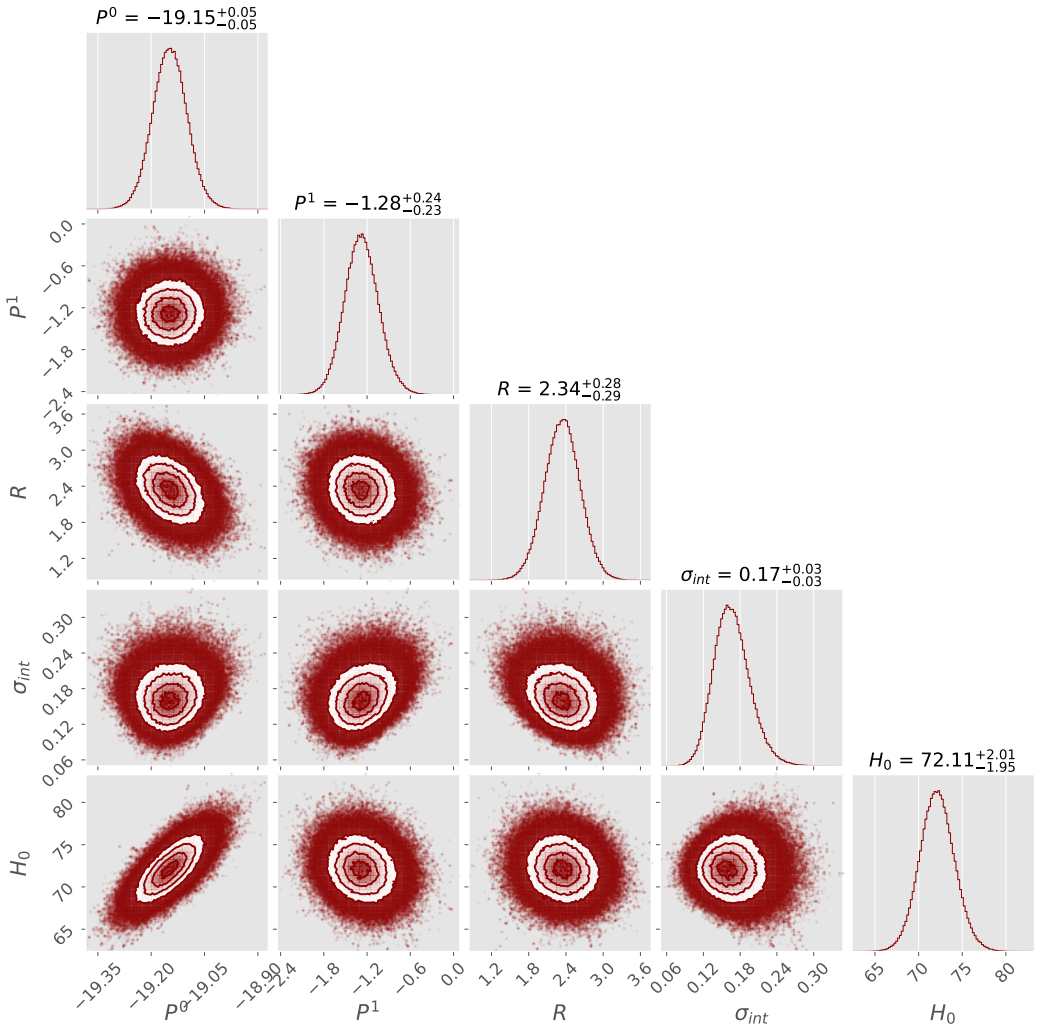

Figure 10: Cornerplot of the posterior distributions from MCMC for the four global parameters $P^0, P^1, R, \sigma_{int}$, and the cosmological parameter H_0. The values were obtained using the SH0ES calibration sample. A median value and uncertainty for each parameter can be seen in the title of the histogram for the specific parameter.

The best-fit value obtained using the SH0ES calibration sample for the Hubble constant is $H_0 = 72.11 \pm 2.02$ km s^{-1} Mpc^{-1}. This value is lower than the value obtained in [Riess et al., 2021] of $H_0 = 73.2 \pm 1.3$ km s^{-1} Mpc^{-1}. The measurements are however still consistent.

A way to visualize the luminosity relation with the stretch and color, is to compare the absolute magnitude of the calibration SNe corrected for the stretch and color. This is shown in Figure 11.

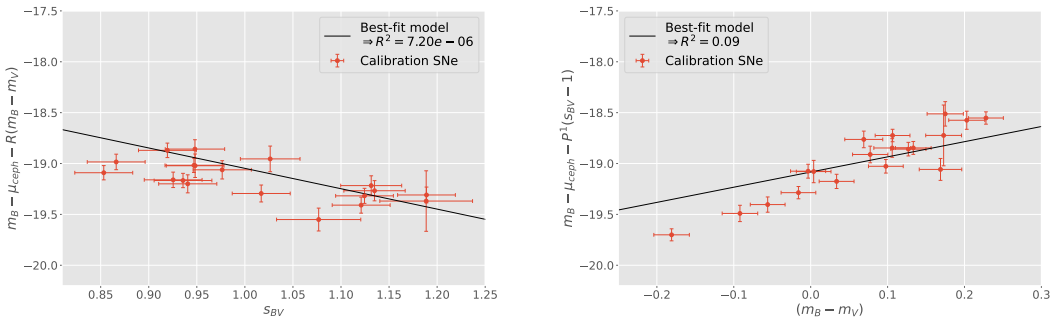

(a) **(b)**

Figure 11: Luminosity correlation plots for the SH0ES calibration sample. Figure **(a)** shows the absolute magnitude corrected for color vs stretch, and Figure **(b)** the absolute magnitude corrected for stretch vs. color. The values of the global parameters are from the MCMC results of Figure 10. R^2 of the model is shown in the legend of each figure.

The absolute magnitude is defined as $M = m - \mu$, whereas for the best-fit model it is given by P^0 from Figure 10. The coefficient of determination, R^2, can be seen in both plots. This statistic tells us about the quality of the best-fit model with respect to the data, by quantifying the proportion of the variance in the dependent variable that is predictable from the independent variable (s_{BV} and $m_B - m_V$). Ideally R^2 attains a value of unity, which means that all of the variance of the model can be predicted from the independent variable. A value of $R^2 = 0$ means, that the model is equally as good of a fit to the data as a horizontal line. In both **(a)** and **(b)**, R^2 takes on quite low values, especially in **(a)**, which means that the best-fit model is not a great fit to the observed data. Even though this might be the case, visually it does seem there is a correlation between the luminosity with respect to color and stretch of the SH0ES Ia SNe.

To investigate how big of a role the cosmological sample size plays with regards to the uncertainty of H_0, we can compare the uncertainty of H_0 estimated using the SH0ES sample to the expected uncertainty. I do this by estimating the relative error in the distance. The distance modulus as a function of distance goes as:

$$\mu(r) \sim 5 \log_{10}(r)$$

which lets us write up the relative error in the distance as:

$$\frac{dr}{r} = \frac{\sigma_{int} \ln(10)}{5\sqrt{N}} \tag{28}$$

where $1/\sqrt{N}$ corrects for the sample size, and I have used $d\mu = \sigma_{int}$. Using $N = 30$ for my sample size, and $\sigma_{int} = 0.17$ from Figure 10, I find:

$$\frac{dr}{r} = 0.014 = 1.4\%$$

which means that solely from the cosmological sample, we would expect a contribution to the total error budget of approximately 1.4% of the estimated value. Furthermore, a comparable error is expected from the calibration sample, as the results from [Riess et al., 2016] are limited by the calibration precision. The total expected error is then approximately:

$$\sigma_{tot} \approx \sqrt{0.014^2 + 0.014^2} \approx 2\%$$

I find an uncertainty of $\sim 2.8\%$ associated with my measurements of H_0 using the SH0ES sample, indicating that perhaps the error associated with the calibration might be larger. Nonetheless, the approximate expected error is of similar order.

As can be seen in Eq. 28, the contribution from the error of the cosmological sample to the total error budget decreases with sample size. For example, if I had a sample size of $N = 100$ SNe, the error from the cosmological sample would be $\sim 0.8\%$. This would not necessarily guarantee a lower error of the MCMC parameters however, as the quality of the SNe in the sample size is also important. Thus, if the SNe added to a sample size are of good quality, we would expect better constraints on the MCMC parameters.

I now perform a similar analysis using the SBF calibration sample, to compare the results obtained using different forms of calibration, even though these are not totally independent. A cornerplot of the result can be seen in Figure 12.

Figure 13 shows the luminosity relation for the SBF sample. The R^2 for both figures lie between the two R^2 values obtained using the SH0ES sample, meaning their values are rather low as well. As such, it would seem there is a lot of the variance in the model which can not be explained by the stretch and color. It should be noted, that the errors associated with the luminosity correlation plots for both calibration samples are quite big, leaving room for improvement if tighter constraints can be placed on the measurements.

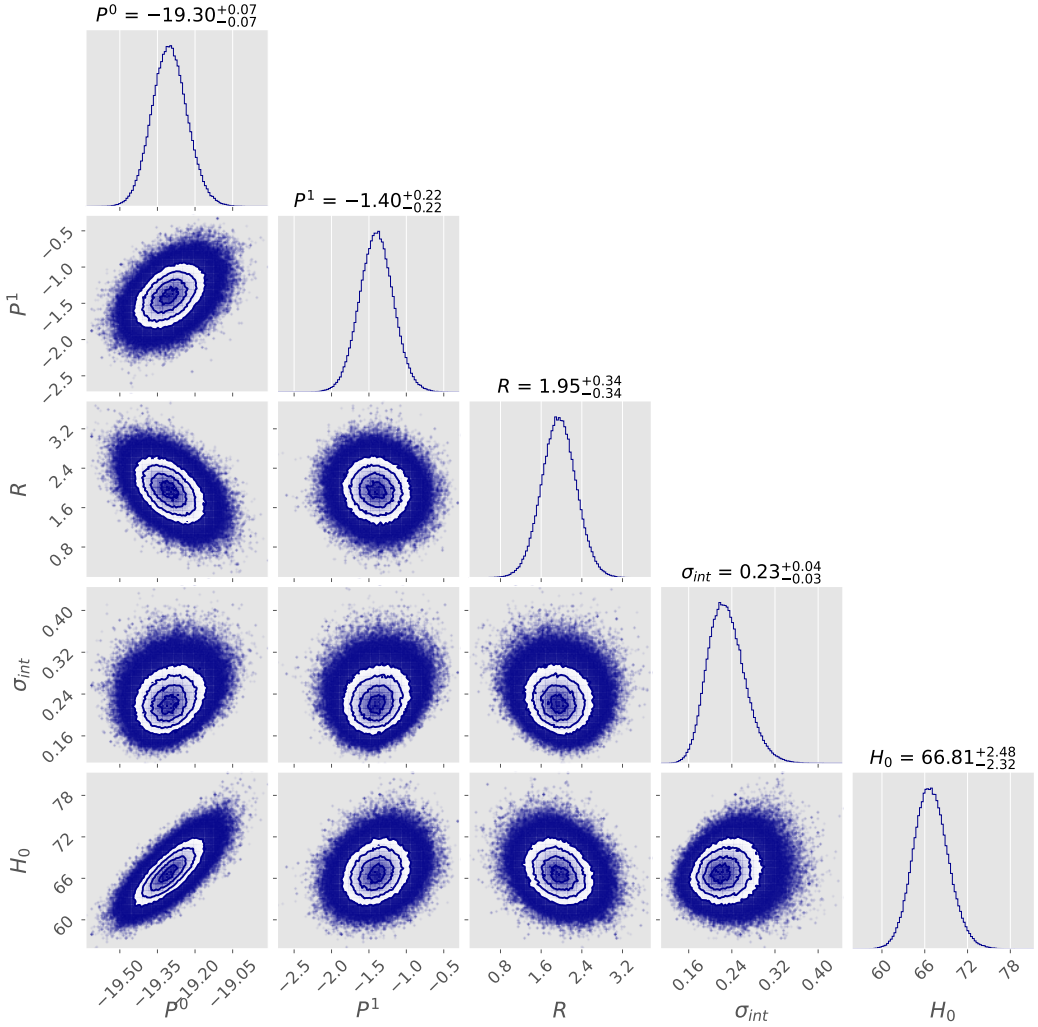

Figure 12: Cornerplot of the posterior distributions from MCMC for the four global parameters $P^0, P^1, R, \sigma_{int}$, and the cosmological parameter H_0. The values were obtained using the SBF calibration sample. A median value and uncertainty for each parameter can be seen in the title of the histogram for the specific parameter.

A table for comparison containing the values for all of the global parameters as well as H_0 can be seen in Table 6. The SBF calibration sample indicates a larger need for stretch correction, as the value of P^1 has decreased slightly, however still well in agreement with the value obtained using the SH0ES calibration sample. Furthermore, the color correction term R is lower, and now is not consistent to within 1σ of the R value obtained using SH0ES. One can speculate, that the decrease in R in the SBF sample compared to the SH0ES sample is not unexpected.

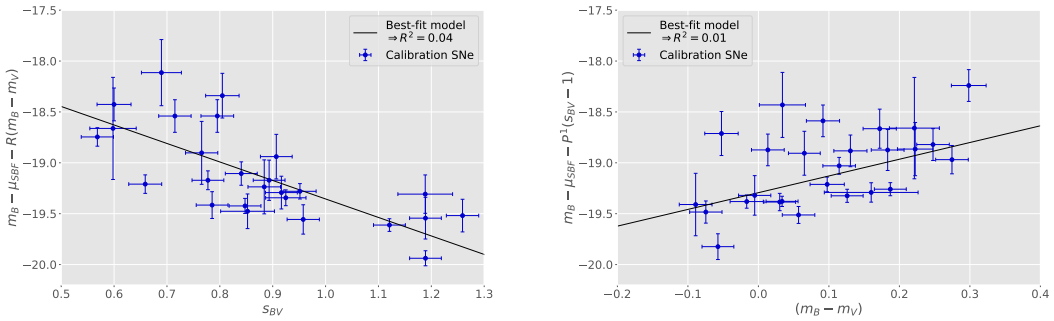

(a) **(b)**

Figure 13: Luminosity correlation plots for the SBF calibration sample. Figure **(a)** shows the absolute magnitude corrected for color vs. stretch, and Figure **(b)** the absolute magnitude corrected for stretch vs color. The values of the global parameters are from the MCMC results of Figure 12. R^2 of the model is shown in the legend of each figure.

As mentioned earlier, the host galaxies of the SBF SNe are all early-type galaxies, which generally contains less dust when compared to late-type galaxies. As such, the need for a color correction could be smaller for these galaxies, and as R reflects the total color correction from all sources, a change in the amount of dust in the host galaxies should be reflected in the parameter, if this is the case.

There is also a difference in σ_{int} between the two samples, as this parameter is only consistent at the 1.41σ level. σ_{int} reflects the quality of the calibration, and tells us the precision to which we can measure the distance modulus per single SN. This means, that the calibration of the SH0ES sample using Cepheids is better. As previously mentioned, SBF calibrations require an additional step of calibration before arriving at estimates of Ia SNe distances. This extra step of calibration introduces more room for errors, which is why we intrinsically expect the calibration using the SH0ES sample to be better.

Perhaps the most interesting change is in H_0. The values are consistent at the 1.67σ level, although because the two measurements share the cosmological sample of Ia SNe, they are not strictly independent. Looking at the P^0 value of the two samples gives a more independent comparison of the calibration samples, as this parameter is tied to the zero point calibration of the Ia SNe. The two values of P^0 are consistent at the 2.56σ level.

As mentioned earlier, the value of H_0 I obtain using the SH0ES sample is consistent to within 1σ of the value obtained by [Riess et al., 2021], whereas the value for H_0 using the SBF sample is consistent only at the 2.3σ level. The value of

Table 6: The different MCMC fit results of the global parameters and the Hubble constant for the SH0ES and SBF calibration sample

Calibration	N_{SN}	P^0 [mag]	P^1 [mag]	R	σ_{int} [mag]	H_0 [km s^{-1} Mpc^{-1}]
SH0ES	30	-19.15 ± 0.05	-1.28 ± 0.24	2.34 ± 0.29	0.17 ± 0.03	72.11 ± 2.02
SBF	30	-19.37 ± 0.07	-1.40 ± 0.23	1.95 ± 0.34	0.23 ± 0.03	66.81 ± 2.45

H_0 obtained by Planck [Aghanim et al., 2020] is $H_0 = 67.4 \pm 0.5$ km s^{-1} Mpc^{-1}, which is in good agreement with the value I obtain using the SBF sample.

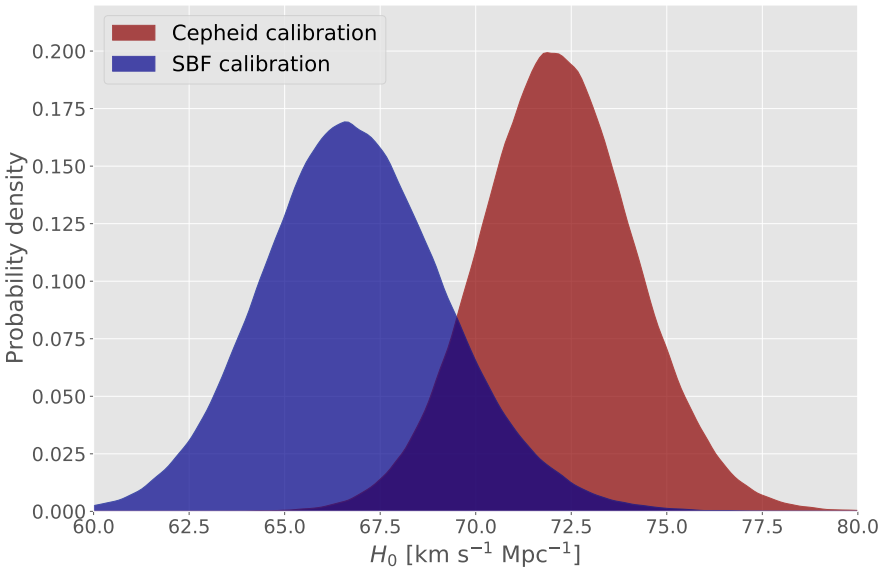

Figure 14: The probability density distribution of H_0 for the Cepheid and SBF calibration samples. The probability density is estimated using a Gaussian Kernel Density Estimation.

To visually compare the distributions for H_0, I have used a Gaussian Kernel Density Estimator (KDE) to estimate the probability density function (PDF) of the distributions, which is shown in Figure 14. The PDF specifies the probability that, in this case, H_0 will fall within a particular range of values. The probability is then given by the integral between the set of values, meaning the integral of the entire PDF is equal to unity. As can be seen in the figure, there is an overlap where the two distributions agree, but for the most part they are separated. The Cepheid calibration distribution also has a slightly higher peak, corresponding to the tighter constraint on H_0 obtained using the SH0ES sample, when compared to the SBF sample.

3.3 Full SN sample and redshift uncertainty

The MCMC result of using the All sample of SNe, while also estimating σ_z implemented by Eq. 17, can be seen in Figure 15. The Hubble diagram with residuals for the full SNe sample is shown in Figure 16.

Table 7 shows the values obtained for the global parameters, using both the Spec sample and the All sample.

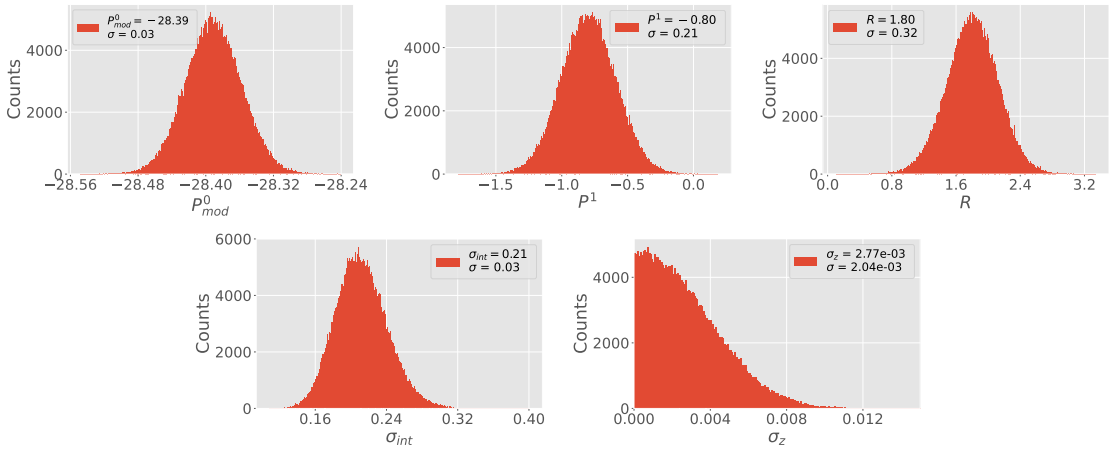

Figure 15: Estimation of the five parameters global parameters using MCMC in the BV filters for the full SNe sample. The mean value and standard deviation of the distribution for each parameter is shown in the legend.

From Table 7, the value of the estimated uncertainty of the redshift σ_z proves to have an upper limit value of $\sigma_z \approx 0.005$, while also being consistent with 0. This means, that the SNe without a redshift measurement from their host in the All sample, does not show a trend of having a significant uncertainty associated with their redshift, even though the redshift might be estimated from the SN spectrum. As such, it makes no sense to include σ_z in further analysis, seeing as it is not statistically significant.

Looking at the global parameters the two samples share, overall the estimates from the MCMC is quite similar. The biggest notable difference is in P^1, where the two values are barely consistent at the 1σ level. The smaller uncertainties on all of the global parameters from All sample can in part be attributed to the fact, that the sample contains more than twice the amount of SNe compared to the Spec sample. Even so, the uncertainties are not much higher for the Spec sample, which can mean the LCs of the SNe in that sample are of higher quality, resulting in LC parameters which are determined to a higher accuracy. The intrinsic scatter takes

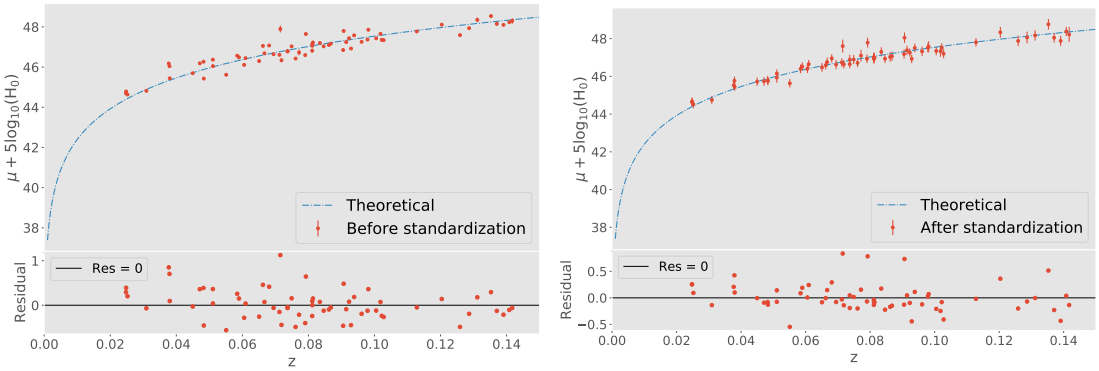

(a) **(b)**

Figure 16: Hubble diagram for the full sample of $N = 64$ SNe. For both plots, a theoretical expectation line has been plotted, as well as the residuals. **(a)** shows the distribution before standardization, and **(b)** shows the distribution after standardization.

on an almost similar value, which means the two samples are nearly equally well calibrated, even though they differ by more than a factor of two in sample size. The standard deviation of the residuals after standardization for the two samples are very similar as well, indicating the samples end up being almost equally well calibrated. The change in the standard deviation of the residuals is largest for the Spec sample however, which tells us that the standardization process was slightly more effective for this sample, even though it is still slightly worse calibrated when compared to the All sample.

Table 7: The MCMC fit results of the global parameters for the two samples of SNe in the BV filters. The 'All' sample includes an estimate of the redshift uncertainty. 'Residual std.' is the standard deviation of the residuals *after* standardization.

Sample	N_{SN}	P^0 [mag]	P^1 [mag]	R	σ_{int} [mag]	σ_z	Residual std.	ΔRes. std.
Spec	30	-28.42 ± 0.05	-1.19 ± 0.35	1.95 ± 0.43	0.22 ± 0.05		0.28	0.10
All	64	-28.39 ± 0.03	-0.80 ± 0.21	1.80 ± 0.32	0.21 ± 0.03	$(2.77 \pm 2.04) \times 10^{-3}$	0.26	0.07

3.4 Fitting g and r filters

While fitting the SNe with a B and V band template in SNooPy was a necessity to estimate the Hubble constant, a more natural choice would be to fit the LCs with a g and r band template, as these are the filters in which the photometric data is originally measured. This is the only part of the thesis, in which results are presented for the g and r filters.

Because the fits are now performed in different templates than previously, it is not a guarantee that the same SNe will pass the quality cuts. SNe which passed the quality cuts in BV filters might not pass the cuts now, meaning the SNe sample could be different. This turns out to be the case. After the cuts I now have a total sample of $N_{All} = 56$ SNe, where $N_{Spec} = 27$ have a spectroscopically measured redshift from their host.

The global parameters for the All and Spec sample are shown in Table B.1, and the Hubble diagrams in Figure B.1, of appendix B. For the All sample, σ_z is again consistent with zero, and so it has not contributed to the error budget in the creation of the Hubble diagram. Comparing the values of the parameters obtained to those in the BV filters, there is a decrease in σ_{int} for the Spec sample, meaning the Spec sample in the gr filters is calibrated more accurately compared to in the BV filters. There is also a significant change in P^1 for the All sample. This result is significantly different from all other values of P^1 estimated in this thesis.

Because the SN samples between the BV and gr filters are not exactly identical, one has to be careful when comparing the results. In the Spec sample they share 25 SNe, while in the All sample they share 52 SNe. Due to the fact that the samples of SNe are not identical, we can not safely attribute any change in the global parameters to the change in filters. However, because the other global parameters obtained in the Spec sample for the gr filters resemble the results of both samples in the BV filters, it seems to suggest there are some SNe in the gr All sample which drive P^1.

Removing the clear outlier SN 2020kvl, which is highlighted in the Hubble diagram in Figure B.1 **(b)**, does not resolve the issue of a high P^1 value. On the contrary, it increases further. Upon further investigation by manual exclusion of potential odd SNe, P^1 appears to be driven towards 0 by the six SNe: 2019wka, 2020ann, 2020ewx, 2020juq, 2020kbl and 2021iok. Removing these six SNe results in $P^1 = -1.12 \pm 0.30$, much more in alignment with other values of P^1 estimated in this thesis. This shows, that switching between filters is a process that requires care, as the results are not guaranteed to be the same.

3.5 Cosmological parameters from peculiar velocities

All of the results obtained in this section are for the BV filters. Furthermore, only SNe from the Spec sample will be used, as an accurate redshift is of great importance. This means, that the sample initially consists of 30 SNe.

Because the reconstructed density and velocity field I use from [Carrick et al., 2015] extends to a redshift of $z \approx 0.07$, SNe with a redshift of $z > 0.07$ are initially discarded. The result of including SNe with $z > 0.07$ is explored in Section 3.5.1. This is needed to make accurate predictions using the model, as including SNe with a higher redshift than the threshold could yield false results. This also means, that requirement (5) from Eq. 7 concerning the quality cuts does not apply to the selection. Even though the motion of SNe at low redshift is usually dominated by peculiar velocities, these are taken into account in the model, so any SN previously discarded due to this can now be included in the sample. The Spec sample for the BV filters contains 9 SNe with $z < 0.02$, but none of them pass the other quality cuts which are still implemented. After implementing the new cuts with a change in the redshift requirement, the sample consists of $N = 15$ SNe.
For the prior, I use the values of the external bulk flow obtained in [Carrick et al., 2015] of $\boldsymbol{V}_{\text{ext}} = (89, -131, 17)$, which I implement in the form of a weak Gaussian prior. The Gaussian is centered at these values, with a dispersion of 200 km s^{-1}. The choice of the dispersion value is arbitrary, but this choice is meant to rid of models with a $\boldsymbol{V}_{\text{ext}}$ far from that of [Carrick et al., 2015], while also serving as an anchor for these values.

Using the sample of 15 SNe, I use MCMC to estimate the global parameters, the bulk velocity $\boldsymbol{V}_{\text{ext}}$, and the relationship between gravitational acceleration and peculiar velocities γ. Using Eq. 23, I can convert the estimated value I obtain for the rescaling factor γ into $f\sigma_8$. The result can be seen in Figure 17.

3.5.1 Exploring the impact of different samples

While only the SNe with $z < 0.07$ should be included in estimating $\boldsymbol{V}_{\text{ext}}$ and γ, the discarded SNe can still contribute in constraining the global parameters. By combining the LLH of [Boruah et al., 2020] and [Khetan et al., 2020] from Eq. 20 and 12 respectively, the 15 SNe which were included in the initial sample will still estimate both the global and cosmological parameters, while the 15 SNe which were previously discarded due to their redshift will estimate only the global parameters. This means, that the new LLH will be given by:

$$\ln \mathcal{L}_{\text{tot}} = \ln P\left(z_{obs} | \boldsymbol{v}, \boldsymbol{V}_{\text{ext}}, \beta, \Theta\right) + \ln \mathcal{L}_{cosmo} \tag{29}$$

where I insert $h = H_0/(100 \text{ km s}^{-1} \text{ Mpc}^{-1})$ into Eq. 10 to be used in $\mathcal{L}_{cosmo}$. The first LLH is for SNe with $z < 0.07$, and the second LLH is for SNe with $z > 0.07$.

To make sure this combination of LLHs preserves the functional shape of the original LLH, while also still having a clear global maxima, I check the shape for

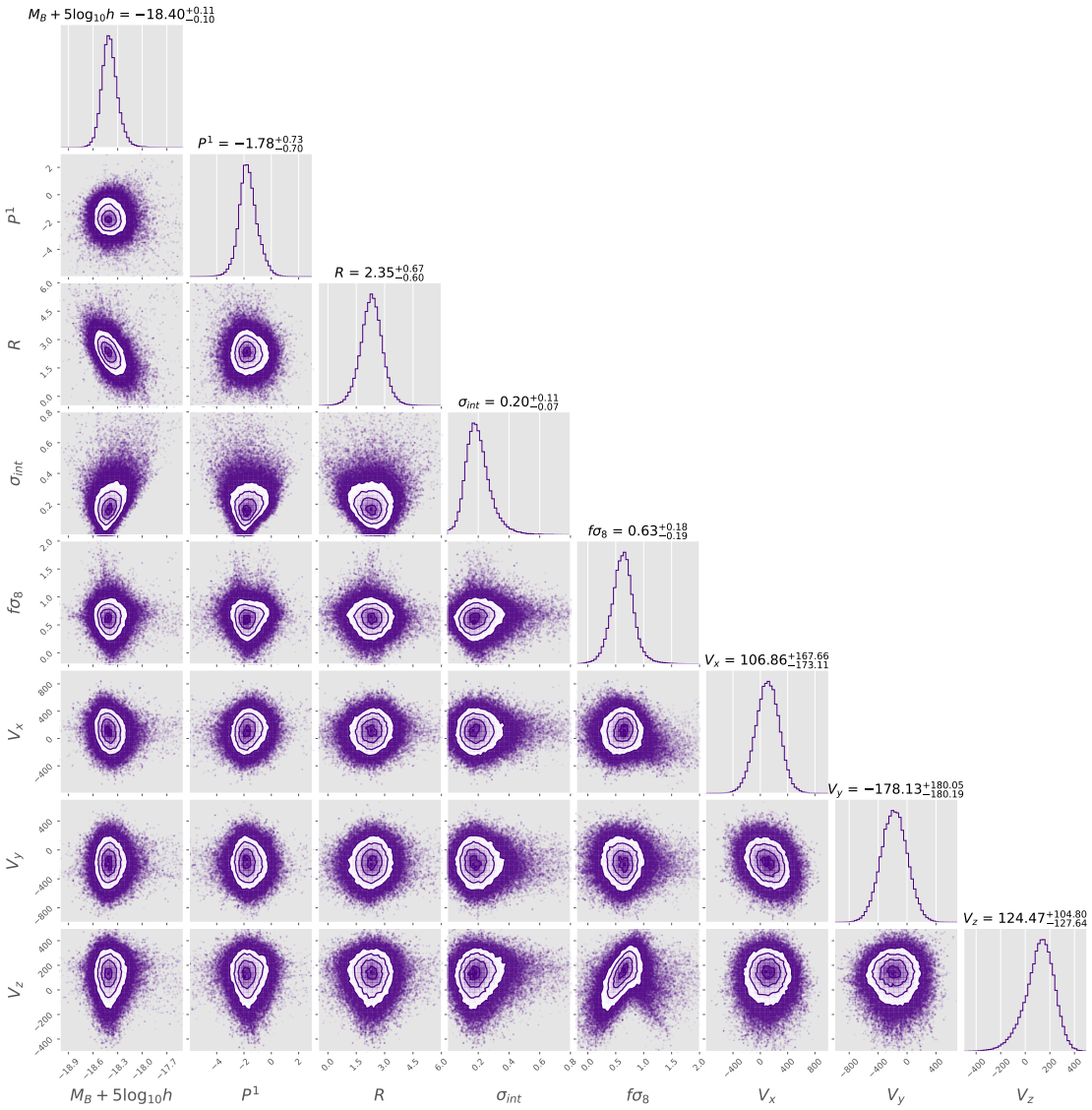

Figure 17: Cornerplot of the four global parameters, the bulk velocity and $f\sigma_8$, using the sample of 15 SNe from YSE.

different values of all the parameters to be estimated. As can be seen in Figure C.1 in appendix C, the functional shape of the LLH has not changed, and it still has a clearly defined global maxima. Furthermore, the combined LLH has tighter constraints on the parameters, as we would expect. I therefore conclude, that the approach to estimate the parameters using MCMC with Eq. 29 is valid. The sample now consists of $N = 30$ SNe, and the results can be seen Figure D.1 in appendix D.

Lastly, I add a subsample of the Foundation sample to my sample of 30 SNe [Jones et al., 2019]. The subsample of the Foundation sample I use consists of 125 spectroscopically classified Ia SNe, all with a redshift of $z < 0.07$. This brings the total sample size to $N = 155$ SNe.

While all of the SNe from the Foundation sample will contribute in constraining $\boldsymbol{V}_{\text{ext}}$ and γ, and therefore also $f\sigma_8$, there is a caveat which must be taken into consideration. Because the Ia SNe I use from the Foundation sample were fit using the SALT2 LC fitting tool, the parameters defining their LCs are not the same as the parameters I have from SNooPy which defines the LCs of the YSE SNe. Therefore, it is not safe to compare the global parameters between the YSE and the Foundation sample, as they are dependent on the LC fitting tool. This means, that when using the conjoined sample of YSE and Foundation SNe, it is important to use the correct formula for the modeled magnitude and the associated variance.

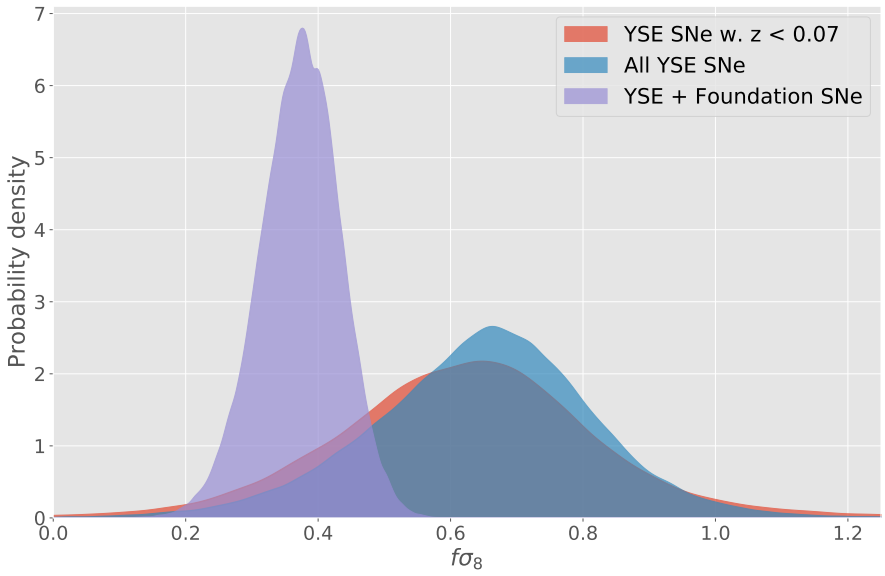

Figure 18: Gaussian Kernel Density Estimate for the three different sample distributions of $f\sigma_8$.

Furthermore, because I do not have the correlation terms of the LC parameters from SALT2 for the Foundation sample, the variance includes only the correlation terms which contains the color. As previously mentioned, however, this exclusion of correlation terms usually results in a negligible difference.

Table 8: The result of using the Forward likelihood method to estimate $f\sigma_8$ and $\boldsymbol{V}_{\text{ext}}$ for the three different Ia SN samples.

Sample	N_{SN}	$f\sigma_8$	V_x [km s^{-1}]	V_y [km s^{-1}]	V_x [km s^{-1}]
YSE ($z < 0.07$)	15	0.63 ± 0.20	106.86 ± 172.12	-178.13 ± 181.91	124.47 ± 122.30
YSE (All)	30	0.66 ± 0.17	146.21 ± 160.79	-202.83 ± 178.07	135.71 ± 112.98
YSE + Foundation	155	0.37 ± 0.07	-62.47 ± 59.35	-265.93 ± 56.84	61.81 ± 43.37

In total I fit for 12 parameters: four global YSE parameters, four global Foundation parameters, and four cosmological parameters. The result can be seen in Figure D.2 in appendix D.

To visually compare the estimated values for $f\sigma_8$, I have used a Gaussian KDE to show the PDF of the $f\sigma_8$ distribution for each of the three Ia SN samples, which is shown in Figure 18. Table 8 shows the values of $f\sigma_8$ and the three components of $\boldsymbol{V}_{\text{ext}}$ obtained for the samples.

3.6 SNooPy vs. SALT2: comparison of standardization

When making the comparison between SALT2 and SNooPy, I perform the analysis for two different samples of SNe:

(1) All SNe in the sample are shared. This means, that to be in this sample, a given SN has to pass the quality cuts for both its SNooPy and SALT2 LC fit parameters. This sample is denoted 'Shared'.

(2) The SNe in the sample for each LC fitting tool have to pass only the quality cuts for the fitting tool in which the SN is. This means, that there will be SNe that are not shared between the two samples. This sample is denoted 'Maximal'.

The result of the standardization can be seen in Figure 19, and a table containing all of the estimated parameters, as well as residuals, can be seen in Table 9.
Because both samples for both LC fitting tools in the histograms have 8 bins, the distributions can look uneven. This is due to the fact that if a sample has a larger scatter, the bins need to stretch further. This is why in both cases, the SNooPy bins look wider.

As seen in Table 9, the Shared sample consists of 36 SNe. The parameter relating to color correction for SNooPy, R, seems a bit low, however the uncertainty is also quite high. The intrinsic scatter between the two LC fitting tools is interesting,

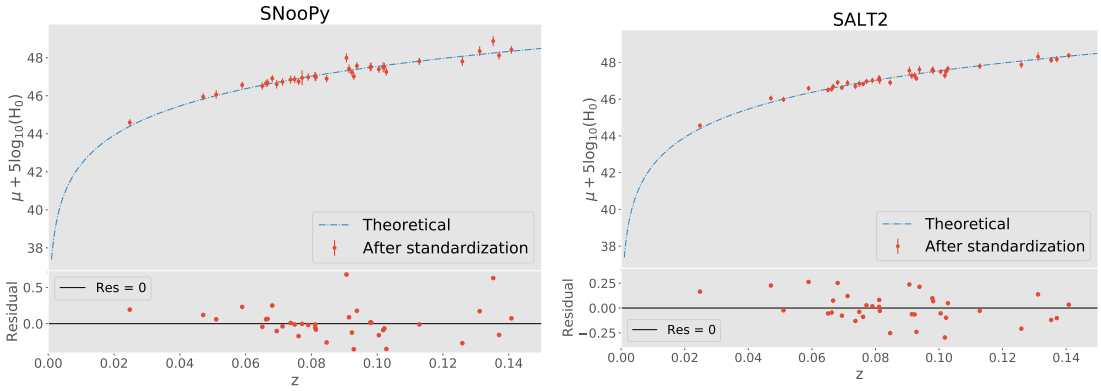

(a) **(b)**

Figure 19: Hubble diagram for the Shared sample for SNooPy and SALT2. The sample consists of $N = 36$ SNe. For both plots, a theoretical expectation line has been plotted, as well as the residuals. **(a)** shows the result for SNooPy, and **(b)** shows the result for SALT2.

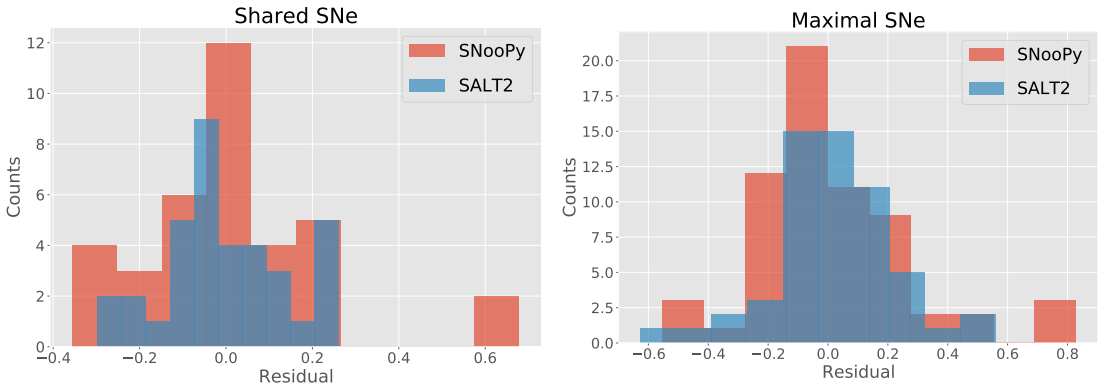

(a) **(b)**

Figure 20: Histograms with $N_{bins} = 8$ bins comparing the residuals for SNooPy and SALT2 after standardization. **(a)** shows the result for the Shared sample, and **(b)** shows the result for the Individual sample. The amount of SNe in each sample, and the standard deviation of the residuals, can be seen in Table 9.

as there is a difference. SALT2 has a lower intrinsic scatter, indicating that it does a better job at calibrating the Shared sample. Visually it can also be seen in Figure 19, where the deviations of SALT2 from the theoretical expectation in **(b)** is smaller compared to SNooPy in **(a)**. This is further proven by the fact, that the spread of the residuals takes on a lower value than in SNooPy, despite having roughly the same spread before the standardization process.

There are two major outliers in Figure 19 **(a)**, which uses SNooPy parameters for the LCs, that are not outliers for SALT2 in **(b)**. These two outliers, placed at $z \approx 0.09$ and $z \approx 0.13$, are SN 2020zbr and SN 2020tqz. Regarding a difference in the 2020zbr LC parameters between the two LC fitting tools, SALT2 estimates a color for 2020zbr of 0.1, while SNooPy estimates a color of -0.1. Regarding a difference in 2020tqz, SNooPy estimates a high stretch for the LC, while SALT2 estimates a very mild stretch. In both cases, when compared to theoretical expectation after standardization, SALT2 appears to find a more correct value of the color for 2020zbr and stretch for 2020tqz. The errors in the color and stretch for the two SNe show no abnormalities when compared to the rest of the sample.

Table 9: The MCMC fit results of the global parameters and the residuals after standardization for the **Shared** and **Maximal** samples for SNooPy and SALT2. Because the two do not share all parameter notation, where they differ the SNooPy parameter and SALT2 parameter, respectively, are separated by a comma.

Shared	N_{SN}	P^0_{mod} [mag]	P^1, α [mag]	R, B	σ_{int} [mag]	Residual std.	ΔRes. std.
SNooPy	36	-28.38 ± 0.04	-1.08 ± 0.28	1.12 ± 0.41	0.17 ± 0.04	0.21	0.06
SALT2	36	-28.32 ± 0.04	0.14 ± 0.02	1.94 ± 0.34	0.12 ± 0.02	0.14	0.12
Maximal SNooPy	64	-28.39 ± 0.03	-0.78 ± 0.20	1.81 ± 0.32	0.21 ± 0.03	0.26	0.07
Maximal SALT2	56	-28.30 ± 0.05	0.10 ± 0.03	2.28 ± 0.37	0.18 ± 0.02	0.20	0.11

The results of using the Maximal sample for each LC fitting tool does not result in a drastic improvement, even though the sample sizes increase. The value of R for SNooPy takes on a value closer to what we would expect, but P^1 increases and takes on a value further from what we would expect compared to in the Shared sample. SALT2 still performs better in the standardization process, as can be seen by σ_{int} and the residuals. Interestingly, the value of σ_{int} increases for both SNooPy and SALT2 for the Maximal sample, indicating that the calibration is actually worse than it was for the Shared sample for both LC fitting tools, despite an increase in the sample size.

4 Discussion

4.1 Manual exclusion of SN

Although the quality cuts exclude SNe whose data is in some way sub-optimal, they are not perfect. It is possible for SNe to pass the quality cuts, even though the fit of their LC is poor. This can in turn result in poor results from the MCMC, meaning a single outlier which does not get automatically detected, can have a big impact on the whole sample. The outlier will however usually be clearly visible on the figures which follow the MCMC analysis. For the data used in this thesis, SN 2020xqb is one such outlier which does not get discarded by the quality cuts, for both the BV and gr samples. It does, however, not have a spectroscopically determined redshift from its host, so for the Spec samples in all filters it does get discarded. But if this SN is not manually discarded, 2020xqb will have a big impact on the results.

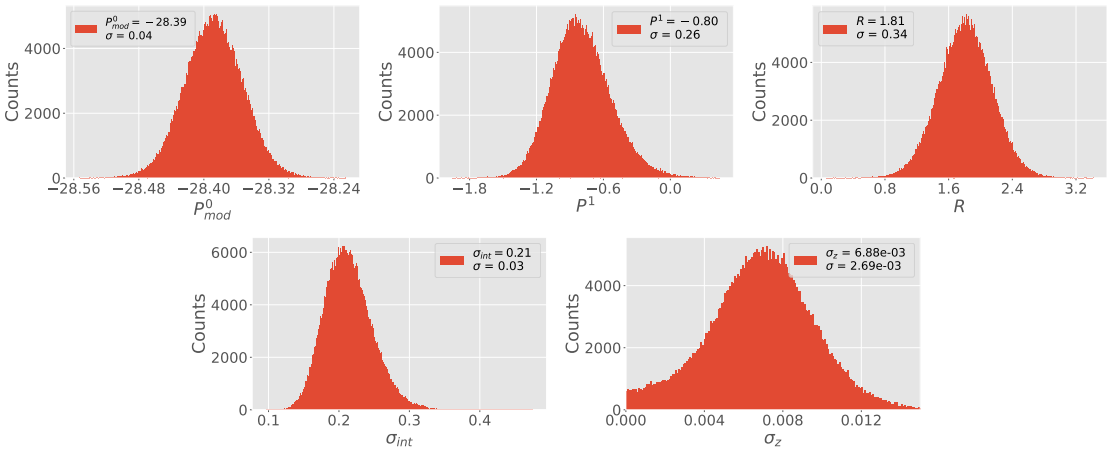

Figure 21: MCMC histograms for the All sample in the BV filters, including SN 2020xqb which was previously discarded manually.

Leaving SN 2020xqb in the sample, will result in an estimate of the redshift uncertainty σ_z, which is not consistent with zero. This is shown in Figure 21.
When compared to the values of the All sample from Table 7, we can see that P^0_{mod}, P^1 and R experience a slight increase in the spread of their distribution, but they and σ_{int} are still consistent. However, σ_z is now significant at the 2.56σ level, meaning it can no longer be considered insignificant.

The Hubble diagram after standardization for this sample is shown in Figure 22. The estimated value of σ_z has been applied to all SNe not in the Spec sample.

From this we can see, that it is hard to say anything conclusive about properties of such SNe.

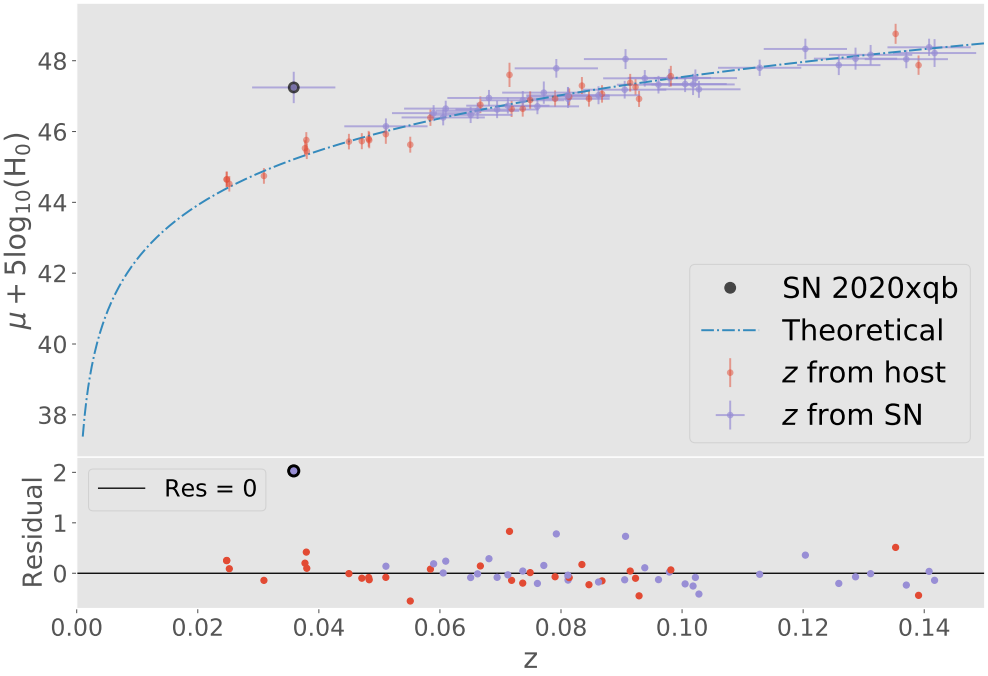

Figure 22: Hubble diagram for the All sample in the BV filters including SN 2020xqb, which is highlighted. The estimated value of σ_z has been applied to all SNe which are not in the Spec sample.

SN 2020xqb is also highlighted in the figure. As can be seen, it is still a big outlier after standardization, and in tension with the theoretical expectation at 4.58σ. Due to it being an extreme outlier, there is good reason to discard the SN from the sample manually.

Because 2020xqb was in need of a strong correction to its redshift to make the distance modulus fit with the theoretically expected value, it drove the estimate of σ_z for all SNe which are not in the Spec sample.

Looking at the fit of the SN from SNooPy, which is shown in Figure A.2 in appendix A, it does seem there is room for wrong interpretation of the LC parameters, as the fit looks to be pretty poor. SN 2020xqb is a case that proves that sometimes there is need for manual inspection, even if the quality cuts manage to discard almost all of the SNe with poor LC fits.

4.2 Similarities and differences between SNooPy and SALT2

Even though the purpose of SNooPy and SALT2 is the same, they are defined in different ways, and are after all models. Because of this, it is not trivial to directly compare the results of the two. Table 1 shows the parameters which each program will estimate for a LC.

One of the main differences, is how the two programs correct for the shape of a LC. Even though both programs use a stretch parameter, they are defined differently. As can be seen from the modeled apparent magnitudes in Eq. 9 and 26, for a normal SN in SNooPy, $s_{BV} = 1$, while for a normal SN in SALT2, $x_1 = 0$. Therefore it is usually not a good idea to mix the parameters of the two fitting tools. For example, the quality cuts from Eq. 7 I implement on my SN samples which I have fit with SNooPy, contain a requirement based on the x_1 parameter from SALT2. As previously mentioned, the two parameters can be converted between one another using Eq. 8, but this is an approximation based on the fit of a correlation [Burns et al., 2014]. One could argue, that a more safe approach would have been to implement a cut using only s_{BV}, as has been done in other works. In [Khetan et al., 2020], they use a cut of $s_{BV} > 0.5$ to discard fast-declining LCs. However, when I implement this requirement for my sample of SNe instead of the original cut (3), it turns out that it changes very little. For the Spec sample, no new SNe are added, while for the All sample, 2 new SNe are added. The effect these two SNe have on the parameters derived using MCMC is almost negligible. The global parameters are unchanged at the second decimal, while the change in H_0 amounts to 0.02 km s^{-1} Mpc^{-1} for the SH0ES calibration sample, and 0.05 for the SBF calibration sample. This corresponds to a change of $(2.77 \times 10^{-4})\%$ and $(7.48 \times 10^{-4})\%$, respectively.

The color of the two models are also defined differently. To estimate the color of a SN, SALT2 uses a functional form for the flux given by[7]:

$$F(t, \lambda) = x_0 \left[M_0(t, \lambda) + x_1 M_1(t, \lambda) \right] \times 10^{-0.4 CL(\lambda) c} \tag{30}$$

The first term is aimed at describing the variability of the SN, such as a normalization term relating to the flux, x_0, and the stretch parameter, x_1. These are both a function of the rest-frame time since peak luminosity in the B band, t, and the wavelength in the rest-frame of the SN, λ. The second term aims at modeling the color of the SN, which is estimated using a color correction law $CL(\lambda)$. If the assumed color correction law is wrong, this will translate to a wrong estimation of the color for the model.

[7] https://sncosmo.readthedocs.io/en/stable/api/sncosmo.SALT2Source.html

Whereas SALT2 estimates the color by using it as a parameter in the model of the flux, the way I obtain the color from SNooPy is by taking the difference between the B and V estimated magnitudes. The color is thus not used as an explicit parameter to be determined within the model. It should be noted that this approach to getting the color is for the max model of SNooPy, which does not assume any extinction. The difference in how I use the two programs to obtain the color, can potentially result in abnormalities, such as in Figure 19. The outlier SN 2020zbr in **(a)** at $z \approx 0.09$ has a very similar fit of its LC between SNooPy and SALT2, but the two programs find a different color. If the color was obtained in the same way for SALT2 as for SNooPy, it would likely have been an outlier in **(b)** as well. However, because the color is estimated in the SALT2 model as a parameter, it results in a more accurate estimate in this instance.

Figure 23 **(a)** compares the color of the Shared sample that SNooPy and SALT2 finds for the SNe. As can be seen, there is a trend of SALT2 finding a considerably lower value of the color than SNooPy. Whereas SNooPy has a roughly even distribution of SNe above and below zero, SALT2 finds a negative color for a large part of the sample. This trend in color for SALT2 then results in most of the residuals prior to standardization being shifted towards negative values, as seen in Figure 23 **(b)**. The standardization manages to correct for this shift in residuals, however. The results after shows no similar trend and are centered around zero, as we would expect.

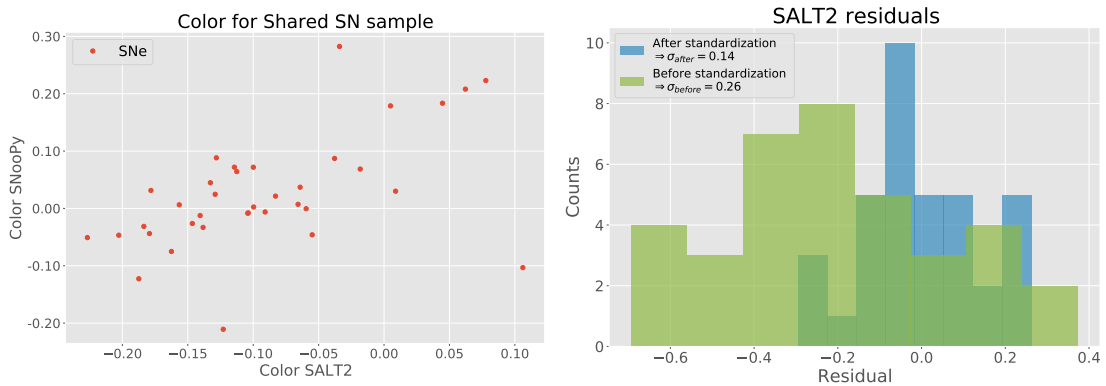

(a) **(b)**

Figure 23: **(a)** shows a comparison of the color between SNooPy and SALT2 for the Shared sample. **(b)** shows a histogram with $N = 8$ bins of the residuals for the SALT2 Shared sample before and after standardization.

In the end however, although parameters for the LC fitting tool and the global parameters derived from them may be defined differently, the intrinsic scatter es-

timated from both models can tell us, which model most accurately calibrates the sample. Going by this metric, SALT2 does a better job both when using the Shared sample, and when using the Maximal sample.

4.3 Hubble constant tension

4.3.1 Influence of host properties on Ia SNe

In Section 3.2, I used the Cepheid and SBF calibration samples to obtain estimates of H_0. It can seem odd, that the value I obtain of $H_0 = 72.11 \pm 2.02$ km s^{-1} Mpc^{-1} using the SH0ES calibration sample does not agree with the value of H_0 I obtain using the SBF calibration sample of $H_0 = 66.81 \pm 2.45$ km s^{-1} Mpc^{-1}. In addition to using a similar late-universe approach, there is also a sort of leakage of the Cepheid calibration into the SBF calibration, because the SBF sample uses Cepheid measurements to calibrate the zero point, which could further strengthen our assumption of obtaining similar H_0 values.

It is however important to note, that there is a difference between the Ia SNe of the SH0ES and SBF sample. The hosts within which the Ia SNe are found are different, except for the three SNe the two samples share. There are several differences between late-type and early-type galaxies, such as metallicity, stellar mass, luminosity etc. If these environmental factors have an impact on the Ia SNe found in the galaxies, they might explain the difference in H_0 between the two methods.

If the cosmological sample of SNe one is working with all have hosts similar to the hosts of SNe in a given calibration sample, one might expect the calibration to be more accurate, as the cosmological and calibration sample would then share more host properties. To investigate if such a correlation of hosts has an impact on the determination of H_0, an additional term can be added to the modeled apparent magnitude formula in Eq. 9 [Khetan et al., 2020][Riess et al., 2016]. This extra term is made to correct the magnitude based on the stellar mass of the host galaxy, which in turn is supposed to act as a tracer of several properties of galaxies, such as star formation rate, metallicity, and stellar population. In [Khetan et al., 2020] they find, that such a correction term does not affect the estimated value of H_0 much, which could imply that the properties of the host galaxy does not play a big role.

In this thesis, I do not include any possible dependence on the host properties of the SNe in my cosmological sample. However if the host properties of the samples do not have much impact on the estimated parameters, then the discrepancy

between the two values I obtain for H_0 using the SH0ES and SBF calibration samples can not be explained by a difference in host properties. There is still much to be done in exploring the effect of the host environment on Ia SNe however, so to completely rule out any effect of the host on the estimate of H_0 requires more investigation.

Nonetheless, if we make the assumption that the host does not have a big impact on the estimation of H_0, one can combine the SH0ES sample with the SBF sample to a single calibration sample of Ia SNe. This can then be done without experiencing a lack of quality in the combined sample due to conflict in the parameters, which could arise due to the host type difference between the two individual samples. If the two samples were in clear tension, it would not be statistically adviseable to combine them. But as they are not in tension even though there is a difference present, this difference could in theory be due to statistical fluctuations.

The result of combing the SH0ES and SBF calibration samples and redoing the H_0 analysis can be seen in Figure E.1 in appendix E. The Hubble constant of the combined sample is found to be $H_0 = 69.78 \pm 2.10$ km s^{-1} Mpc^{-1}. Not surprisingly, most of the parameters take on a value somewhere in-between the values of the two samples from Table 6. The SH0ES sample does seem to drive the values of the parameters more, which can be due to its better calibration.

4.3.2 Comparison of H_0 across methods

To review some of the values obtained for H_0 and display the tension, Figure 24 displays values of H_0 obtained using both different and a similar approaches to the one used in this thesis.

[Birrer et al., 2020] and [Wong et al., 2020] uses strong gravitational lensing time delays to measure H_0, and find a value in agreement with H_0 measured using Cepheids and Ia SNe. Although the method used by [Birrer et al., 2020] is similar, they find that the resulting value of H_0 agrees with the value obtained using the CMB from [Aghanim et al., 2020]. [Macaulay et al., 2019] use baryonic acoustic oscillations (BAO) measured from the CMB to calibrate distances to Ia SNe, and [Abbott et al., 2018] uses clustering and weak lensing data with BAO calibrated with the Big Bang Nucleosynthesis estimate of the baryonic mass density $\Omega_{baryons}$, to constrain H_0. Both of their results are in agreement with the Planck value from [Aghanim et al., 2020].
The H_0 value I obtain using the SBF sample is in best agreement with the Planck value and the values obtained using BAO. The Planck and BAO values are all

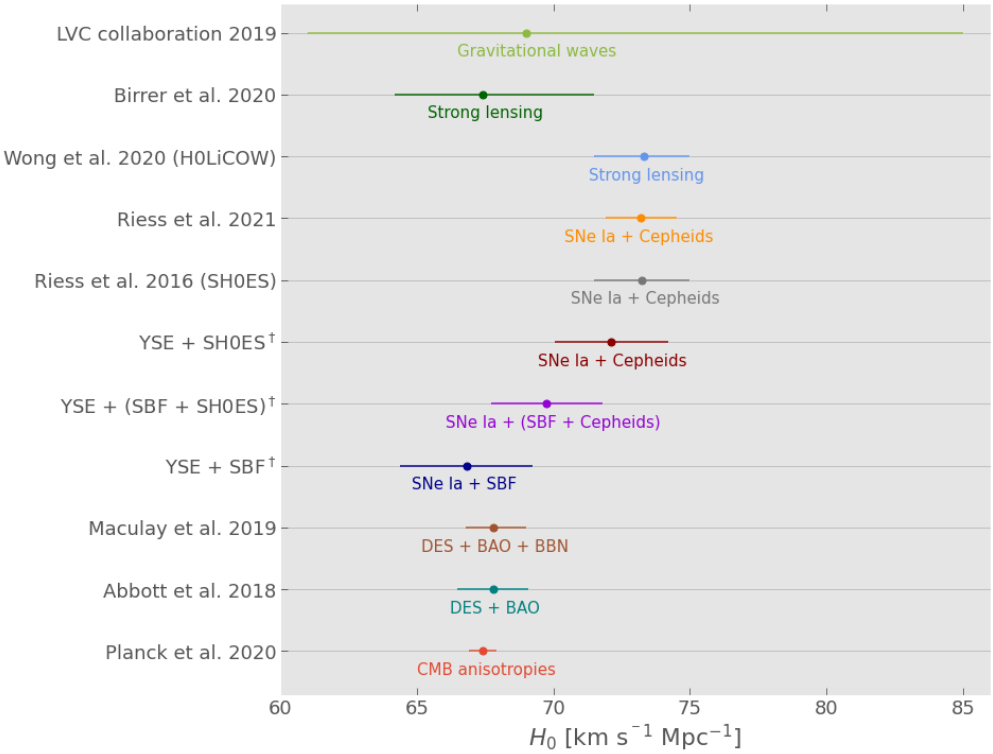

Figure 24: Comparison of values obtained for H_0 using different methods. Values obtained in this thesis are denoted with †. Values of H_0 from top to bottom are taken from the following references: [Abbott et al., 2021], [Birrer et al., 2020], [Wong et al., 2020], [Riess et al., 2021], [Riess et al., 2016], [Macaulay et al., 2019], [Abbott et al., 2018], [Aghanim et al., 2020].

obtained using different physics than what is used with the SBF sample, as they all have an early-universe approach to measuring H_0. In fact, the method used in [Macaulay et al., 2019] is sometimes referred to as the 'inverse distance ladder' approach, as it uses the CMB to calibrate distance via. the sound horizon scale.

The H_0 value I obtain using the SH0ES sample is in best agreement with other results obtained using Cepheids for calibration, as well as the result from [Wong et al., 2020] obtained using strong lensing. Apart from my measurement of H_0 using the SBF sample, there is trend of agreement between methods which uses physics from a similar time period of the universe.

While most of these different methods are independent, assumptions about the cosmology of the universe have to be made in order to estimate H_0. For example, in order to make use of Eq. 10, I assume a universe of zero curvature with a Robertson-Walker metric. Furthermore, I adopt best-fit values from the ΛCDM

model of $q_0 = -0.55$ and $j_0 = 1$, although as previously mentioned, varying these two parameters should have little impact on the final result. Even so, this means the analysis performed in this thesis is not model-independent, and the measurements obtained can therefore be thought of as indirect measurements. If the indirect measurements are based on the correct model, however, they should agree with direct measurements, if such measurements are ever obtained.

Nonetheless, Figure 24 clearly shows, that there is a tension present between the different methods used to estimate H_0. If the ΛCDM model is the correct model to describe our universe, measurements which are based upon the model need to be consistent. As of now, this is not the case for H_0, and the reasons why are still unclear. Even for the values obtained in this thesis, there is a clear difference. These differences needs to be investigated, to see if they have a natural explanation that is valid within the ΛCDM model. Despite using the exact same approach to measure H_0 in this thesis, the calibration samples that are used play a big role, and so this would be a natural place to start to try and explain the difference between the H_0 measurements I obtain. For further analysis, investigating whether the host properties of Ia SNe actually does have an impact in measurements of H_0 would be very interesting. This would require a cosmological sample containing only Ia SNe observed within late-type galaxies and early-type galaxies for the SH0ES and SBF sample, respectively. To accomplish this, while also having a sample of significant size, would require more observations of type Ia SNe from YSE. There is a good opportunity for this, as the YSE experiment is on-going. When the second telescope at Pan-STARRS, Pan-STARRS2, becomes operational, the amount of detected Ia SNe should double in size, further increasing the potential for a larger cosmological sample.

If one is working with a very small sample of Ia SNe and do not include any dependence on host properties, it could happen by chance that all SNe would share a similar host environment. This could then potentially impact the estimation of H_0, depending on which calibration sample is used. Even though I do not include any host dependence in the cosmological sample, my sample is big enough to rule out a big effect of sample bias. As such, we would not necessarily expect the difference between the H_0 estimations in this thesis to decrease much, even if a larger cosmological sample is used.

4.4 Constraints on the linear growth

Comparing the three values I have obtained for $f\sigma_8$, which are shown in Table 8, it is clear that adding the Foundation sample to the YSE sample has a big impact. While $f\sigma_8$ is not consistent with zero for the two YSE samples (YSE ($z < 0.07$))

and YSE All), the values and their corresponding uncertainties are considerably higher than for the combined YSE + Foundation sample. This is also visualized by the spread of the distributions for the two samples in Figure 18, where it can be seen that the distribution for the combined YSE + Foundation sample has a much lower spread.

The three components of the estimated bulk flow velocity are all consistent with zero for the two YSE samples. Adding the Foundation sample places tighter constraint on the bulk flow velocity, especially V_y which becomes much more significant.

As previously mentioned, determining $f\sigma_8$ is important to check if it is consistent with the ΛCDM model. The values I obtain for $f\sigma_8$ is obtained using the model of [Carrick et al., 2015], whose model is based on the ΛCDM model. Thus, if the ΛCDM model is consistent, I should obtain results similar to what we would expect using Planck cosmology.

To check this, we can assume Planck cosmology and compare different results obtained for $f\sigma_8$ at different redshift, to the expected value for the ΛCDM model. In [Aghanim et al., 2020], they find the matter fluctuation amplitude at zero redshift to be $\sigma_8 = 0.811 \pm 0.006$. As a function of redshift, σ_8 depends on the linear growth D, as $\sigma_8(z) = \sigma_8(z = 0)D$, where by definition $D(z = 0) = 1$. The linear growth can be expressed in terms of the scale factor a and the growth rate f by:

$$f = \frac{d \ln D}{d \ln a} \tag{31}$$

where $a = \frac{1}{1+z}$, and in the ΛCDM model $f \approx \Omega_m^{0.55}$. Using this, we find

$$\ln (1/D) = \int_0^z \Omega(z)_m^{0.55} \frac{dz}{1+z} \tag{32}$$

and we can then write $f\sigma_8(z)$ as:

$$f\sigma_8(z) = \Omega^{0.55} \exp (D)\sigma_8(z = 0) \tag{33}$$

The result of the theoretical expectation assuming the ΛCDM model, as well as measurements taken at different redshifts, can be seen in Figure 25.
The measurements of $f\sigma_8$ for the YSE + Foundation sample and the YSE ($z < 0.07$) sample are consistent with the prediction of ΛCDM. Because the error for both the YSE ($z < 0.07$) sample and the YSE All sample is quite big, it can alleviate some of the discrepancy between the $f\sigma_8$ measurements of these samples

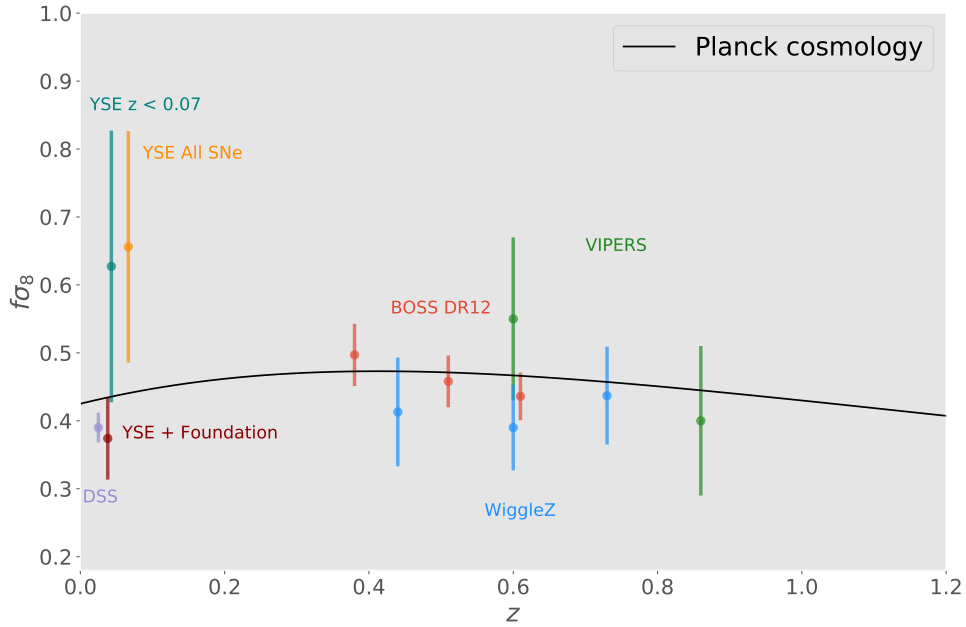

Figure 25: Comparison of the values of $f\sigma_8$ obtained in this thesis, as well as other values at higher redshift from DSS [Stahl et al., 2021], BOSS DR12 [Alam et al., 2017], WiggleZ [Blake et al., 2012] and VIPERS [De La Torre et al., 2013]. The theoretical expectation assuming Planck cosmology (ΛCDM model) is also shown.

and the expected value from Planck cosmology, and therefore also argued that the YSE All measurement of $f\sigma_8$ is also consistent with the ΛCDM model. The sample size for these two samples are also quite low when compared to the YSE + Foundation sample size, which can explain the difference in error. The error goes as $\sigma \sim 1/\sqrt{N}$, which means that if we compare the error on $f\sigma_8$ measured using the YSE + Foundation sample with $N = 155$ SNe, to the error of the YSE All sample with $N = 30$ SNe, we would expect the error of $f\sigma_8$ measured using the YSE All sample to be ~ 2.3 times bigger than the error of the YSE + Foundation sample. This is consistent with what is shown in Table 8.

To conclude whether the ΛCDM model predicts $f\sigma_8$ accurately requires very precise measurements with uncertainties of a few percent. Neither the results in this thesis, the measurement of DSS, or any of the other included measurements at higher redshift, manages to accomplish this. The measurement with the highest precision is the DSS measurement with an uncertainty of $\sim 5.9\%$. As such, there is still work to be done in the future to determine $f\sigma_8$ with the desired level of uncertainty, to conclude if what we observe agrees completely with the ΛCDM model.

It would be interesting to revisit this analysis at a later time, when YSE has acquired data from significantly more Ia SNe. According to [Jones et al., 2021], the predicted amount of Ia SNe YSE expects to observe in a year, based on simulations, is 3920. My initial sample consisted of $N = 157$ spectroscopically classified Ia SNe, and the amount of SNe from YSE which was included in the $z < 0.07$ sample was $N = 15$. This corresponds to $\sim 9.5\%$ of all Ia SNe in the initial sample. Going by this metric, and assuming that the YSE experiment will be on-going for at least two more years, the $z < 0.07$ sample size to constrain $f\sigma_8$ should increase to approximately $N \approx 760$ Ia SNe. Using a sample of this size would mean, that the uncertainty on $f\sigma_8$ using the same approach as in this thesis should be ~ 2.2 times smaller than that of the YSE + Foundation sample. There are some caveats associated with this estimate however. It can be difficult to predict the amount of expected Ia SNe to observe in a year, and the second telescope YSE plans to use for its survey, Pan-STARRS2, has yet to become operational. As such, the estimated amount of Ia SNe that should be available from YSE in two years is a rough approximation, and likely subject to change.

5 Summary

In this thesis, I have explored different aspects of the usability of LCs from type Ia SNe. What this encompasses is summarized below.

- Using data from YSE, I have fit the LCs observed in *griz* filters of all the Ia SNe contained herein. I fit the LCs with the fitting tool SNooPy, to obtain the parameters defining the LC of a Ia SN. Using these parameters, I calibrate the sample in the *BV* and *gr* filters using MCMC. This is done for two samples: one consisting only of SNe with a spectroscopically measured redshift from their host, and one containing all Ia SNe. Using the calibration parameters relating to the stretch and color of the sample, I standardize the SNe and create a Hubble diagram. Furthermore, I find that switching the photometric data from the LCs of the Ia SNe between filters does not necessarily yield identical results. Care must be taken when converting between filters, as the quality of the data in the used sample can vary with these.

- Using the full sample of SNe, I explore the impact of redshift uncertainty on the SNe with a redshift estimated from their spectrum. I find that if the quality of my sample is assured, there is no significant evidence for an uncertainty in the redshift. If the sample contains an outlier, however, it takes only a single SN to create a statistically significant uncertainty in the redshift, proving that sample quality is important.

- I make the first determination of the Hubble constant with YSE SNe, using Bayesian inference with a MCMC. This is done for two different calibration samples. The first is the SH0ES sample, which relies on Cepheids for distance measurements. The second is an SBF sample, which relies on early-type galaxy images for distance estimates and Cepheids for zero point calibration. I find the resulting values of H_0 are significantly different, although using the SH0ES sample results in a better calibration. For the SH0ES calibration sample I obtain $H_0 = 72.11 \pm 2.02$, in agreement with other measurements of H_0 obtained using late-universe physics. Using the SBF calibration sample, I find $H_0 = 66.81 \pm 2.45$, which is in agreement with measurements of H_0 obtained using early-universe physics.

- I determine the linear growth rate of structure, $f\sigma_8$, with YSE SNe. The analysis is performed for three different samples, one of which combines YSE SNe with a subsample of the Foundation sample. I find that the three measurements of $f\sigma_8$ are in agreement with the theoretical expectation of the ΛCDM model, however the measurements obtained using only YSE SNe have large errors associated with them, due to their low sample size. The

value of $f\sigma_8 = 0.37 \pm 0.07$ obtained using the combined YSE + Foundation sample results in the tightest constraint on $f\sigma_8$ between the three samples, in alignment with what we would expect from a significant increase in sample size.

- I compare the two main Ia SN LC fitting tools, SNooPy and SALT2, for my SN sample in the BV filters. Despite different methodologies, such as spectral templates and adopted interpolations, definitions of color and stretch, both calibrations are consistent. I find that for both the sample where all SNe are shared between them, and a sample where the sample size is maximized individually, SALT2 performs a better calibration of the sample.

6 References

G Pietrzyński, D Graczyk, W Gieren, IB Thompson, B Pilecki, A Udalski, I Soszyński, S Kozłowski, P Konorski, K Suchomska, et al. An eclipsing-binary distance to the large magellanic cloud accurate to two per cent. *Nature*, 495 (7439):76–79, 2013.

DW Pesce, JA Braatz, MJ Reid, AG Riess, D Scolnic, JJ Condon, F Gao, C Henkel, CMV Impellizzeri, CY Kuo, et al. The megamaser cosmology project. xiii. combined hubble constant constraints. *The Astrophysical Journal Letters*, 891(1):L1, 2020.

Henrietta S Leavitt and Edward C Pickering. Periods of 25 variable stars in the small magellanic cloud. *Harvard College Observatory Circular*, 173:1–3, 1912.

John Tonry and Donald P Schneider. A new technique for measuring extragalactic distances. *The Astronomical Journal*, 96:807–815, 1988.

Michele Cantiello, JB Jensen, JP Blakeslee, E Berger, AJ Levan, NR Tanvir, Gabriella Raimondo, Enzo Brocato, KD Alexander, PK Blanchard, et al. A precise distance to the host galaxy of the binary neutron star merger gw170817 using surface brightness fluctuations. *The Astrophysical Journal Letters*, 854(2): L31, 2018.

Steven A. Rodney, Adam G. Riess, Louis-Gregory Strolger, Tomas Dahlen, Or Graur, Stefano Casertano, Mark E. Dickinson, Henry C. Ferguson, Peter Garnavich, Brian Hayden, and et al. Type ia supernova rate measurements to redshift 2.5 from candels: Searching for prompt explosions in the early universe. *The Astronomical Journal*, 148(1):13, Jun 2014. ISSN 1538-3881. doi: 10.1088/0004-6256/148/1/13. URL http://dx.doi.org/10.1088/0004-6256/148/1/13.

O. Graur, S. A. Rodney, D. Maoz, A. G. Riess, S. W. Jha, M. Postman, T. Dahlen, T. W.-S. Holoien, C. McCully, B. Patel, and et al. Type-ia supernova rates to redshift 2.4 from clash: The cluster lensing and supernova survey with hubble. *The Astrophysical Journal*, 783(1):28, Feb 2014. ISSN 1538-4357. doi: 10.1088/0004-637x/783/1/28. URL http://dx.doi.org/10.1088/0004-637X/783/1/28.

Mark M Phillips. The absolute magnitudes of type ia supernovae. *The Astrophysical Journal*, 413:L105–L108, 1993.

Robert D Tripp. A two-parameter luminosity correction for type ia supernovae. *Astronomy and Astrophysics*, 331(3), 1997.

Nabila Aghanim, Yashar Akrami, M Ashdown, J Aumont, C Baccigalupi, M Ballardini, AJ Banday, RB Barreiro, N Bartolo, S Basak, et al. Planck 2018 results-vi. cosmological parameters. *Astronomy & Astrophysics*, 641:A6, 2020.

Adam G Riess, Stefano Casertano, Wenlong Yuan, J Bradley Bowers, Lucas Macri, Joel C Zinn, and Dan Scolnic. Cosmic distances calibrated to 1% precision with gaia edr3 parallaxes and hubble space telescope photometry of 75 milky way cepheids confirm tension with λcdm. *The Astrophysical Journal Letters*, 908(1): L6, 2021.

Supranta S Boruah, Michael J Hudson, and Guilhem Lavaux. Cosmic flows in the nearby universe: new peculiar velocities from sne and cosmological constraints. *Monthly Notices of the Royal Astronomical Society*, 498(2):2703–2718, 2020.

Eric V Linder. Exponential gravity. *Physical Review D*, 80(12):123528, 2009.

Jonathan Carrick, Stephen J Turnbull, Guilhem Lavaux, and Michael J Hudson. Cosmological parameters from the comparison of peculiar velocities with predictions from the 2m++ density field. *Monthly Notices of the Royal Astronomical Society*, 450(1):317–332, 2015.

D. O. Jones, R. J. Foley, G. Narayan, J. Hjorth, M. E. Huber, P. D. Aleo, K. D. Alexander, C. R. Angus, K. Auchettl, V. F. Baldassare, and et al. The young supernova experiment: Survey goals, overview, and operations. *The Astrophysical Journal*, 908(2):143, Feb 2021. ISSN 1538-4357. doi: 10.3847/1538-4357/abd7f5. URL http://dx.doi.org/10.3847/1538-4357/abd7f5.

Daniel Foreman-Mackey, David W Hogg, Dustin Lang, and Jonathan Goodman. emcee: the mcmc hammer. *Publications of the Astronomical Society of the Pacific*, 125(925):306, 2013.

Jonathan Goodman and Jonathan Weare. Ensemble samplers with affine invariance. *Communications in applied mathematics and computational science*, 5(1): 65–80, 2010.

Julien Guy, P Astier, S Baumont, D Hardin, R Pain, N Regnault, S Basa, RG Carlberg, A Conley, S Fabbro, et al. Salt2: using distant supernovae to improve the use of type ia supernovae as distance indicators. *Astronomy & Astrophysics*, 466 (1):11–21, 2007.

Christopher R Burns, Maximilian Stritzinger, MM Phillips, ShiAnne Kattner, SE Persson, Barry F Madore, Wendy L Freedman, Luis Boldt, Abdo Campillay, Carlos Contreras, et al. The carnegie supernova project: light-curve fitting with snoopy. *The Astronomical Journal*, 141(1):19, 2010.

Christopher R Burns, Maximilian Stritzinger, MM Phillips, EY Hsiao, Carlos Contreras, SE Persson, Gaston Folatelli, Luis Boldt, Abdo Campillay, Sergio Castellón, et al. The carnegie supernova project: intrinsic colors of type ia supernovae. *The Astrophysical Journal*, 789(1):32, 2014.

EY Hsiao, A Conley, DA Howell, M Sullivan, CJ Pritchet, RG Carlberg, PE Nugent, and MM Phillips. K-corrections and spectral templates of type ia supernovae. *The Astrophysical Journal*, 663(2):1187, 2007.

David J Schlegel, Douglas P Finkbeiner, and Marc Davis. Maps of dust infrared emission for use in estimation of reddening and cosmic microwave background radiation foregrounds. *The Astrophysical Journal*, 500(2):525, 1998.

Charles L Steinhardt, Albert Sneppen, and Bidisha Sen. Effects of supernova redshift uncertainties on the determination of cosmological parameters. *The Astrophysical Journal*, 902(1):14, 2020.

MEA Betoule, R Kessler, J Guy, J Mosher, D Hardin, R Biswas, P Astier, P El-Hage, M Konig, S Kuhlmann, et al. Improved cosmological constraints from a joint analysis of the sdss-ii and snls supernova samples. *Astronomy & Astrophysics*, 568:A22, 2014.

Adam G Riess, Steven A Rodney, Daniel M Scolnic, Daniel L Shafer, Louis-Gregory Strolger, Henry C Ferguson, Marc Postman, Or Graur, Dan Maoz, Saurabh W Jha, et al. Type ia supernova distances at redshift$>$ 1.5 from the hubble space telescope multi-cycle treasury programs: the early expansion rate. *The Astrophysical Journal*, 853(2):126, 2018.

Nandita Khetan, Luca Izzo, Marica Branchesi, Radosław Wojtak, Michele Cantiello, Chandrashekar Murugeshan, A Agnello Cappellaro, M Della Valle, C Gall, J Hjorth, et al. A new measurement of the hubble constant using type ia supernovae calibrated with surface brightness fluctuations. *arXiv preprint arXiv:2008.07754*, 2020.

Suhail Dhawan, D Brout, D Scolnic, Ariel Goobar, AG Riess, and V Miranda. Cosmological model insensitivity of local h 0 from the cepheid distance ladder. *The Astrophysical Journal*, 894(1):54, 2020.

Adam G Riess, Lucas M Macri, Samantha L Hoffmann, Dan Scolnic, Stefano Casertano, Alexei V Filippenko, Brad E Tucker, Mark J Reid, David O Jones, Jeffrey M Silverman, et al. A 2.4% determination of the local value of the hubble constant. *The Astrophysical Journal*, 826(1):56, 2016.

Stéphane Blondin and John L Tonry. Determining the type, redshift, and age of a supernova spectrum. *The Astrophysical Journal*, 666(2):1024, 2007.

RW Pike and Michael J Hudson. Cosmological parameters from the comparison of the 2mass gravity field with peculiar velocity surveys. *The Astrophysical Journal*, 635(1):11, 2005.

DO Jones, DM Scolnic, RJ Foley, A Rest, R Kessler, PM Challis, KC Chambers, DA Coulter, KG Dettman, MM Foley, et al. The foundation supernova survey: measuring cosmological parameters with supernovae from a single telescope. *The Astrophysical Journal*, 881(1):19, 2019.

S Birrer, AJ Shajib, A Galan, M Millon, T Treu, A Agnello, M Auger, GC-F Chen, L Christensen, T Collett, et al. Tdcosmo-iv. hierarchical time-delay cosmography–joint inference of the hubble constant and galaxy density profiles. *Astronomy & Astrophysics*, 643:A165, 2020.

Kenneth C Wong, Sherry H Suyu, Geoff CF Chen, Cristian E Rusu, Martin Millon, Dominique Sluse, Vivien Bonvin, Christopher D Fassnacht, Stefan Taubenberger, Matthew W Auger, et al. H0licow–xiii. a 2.4 per cent measurement of h 0 from lensed quasars: 5.3 σ tension between early-and late-universe probes. *Monthly Notices of the Royal Astronomical Society*, 498(1):1420–1439, 2020.

Eric Macaulay, RC Nichol, D Bacon, D Brout, TM Davis, B Zhang, B A Bassett, D Scolnic, A Möller, CB D'Andrea, et al. First cosmological results using type ia supernovae from the dark energy survey: measurement of the hubble constant. *Monthly Notices of the Royal Astronomical Society*, 486(2):2184–2196, 2019.

TMC Abbott, FB Abdalla, J Annis, K Bechtol, J Blazek, BA Benson, RA Bernstein, GM Bernstein, E Bertin, D Brooks, et al. Dark energy survey year 1 results: a precise h0 estimate from des y1, bao, and d/h data. *Monthly Notices of the Royal Astronomical Society*, 480(3):3879–3888, 2018.

BP Abbott, R Abbott, TD Abbott, S Abraham, F Acernese, K Ackley, C Adams, RX Adhikari, VB Adya, C Affeldt, et al. A gravitational-wave measurement of the hubble constant following the second observing run of advanced ligo and virgo. *The Astrophysical Journal*, 909(2):218, 2021.

Benjamin E Stahl, Thomas de Jaeger, Supranta S Boruah, WeiKang Zheng, Alexei V Filippenko, and Michael J Hudson. Peculiar-velocity cosmology with types ia and ii supernovae. *arXiv preprint arXiv:2105.05185*, 2021.

Shadab Alam, Metin Ata, Stephen Bailey, Florian Beutler, Dmitry Bizyaev, Jonathan A Blazek, Adam S Bolton, Joel R Brownstein, Angela Burden, Chia-Hsun Chuang, et al. The clustering of galaxies in the completed sdss-iii baryon oscillation spectroscopic survey: cosmological analysis of the dr12 galaxy sample. *Monthly Notices of the Royal Astronomical Society*, 470(3):2617–2652, 2017.

Chris Blake, Sarah Brough, Matthew Colless, Carlos Contreras, Warrick Couch, Scott Croom, Darren Croton, Tamara M Davis, Michael J Drinkwater, Karl Forster, et al. The wigglez dark energy survey: Joint measurements of the expansion and growth history at z$<$ 1. *Monthly Notices of the Royal Astronomical Society*, 425(1):405–414, 2012.

S De La Torre, L Guzzo, JA Peacock, E Branchini, A Iovino, BR Granett, U Abbas, C Adami, S Arnouts, Julien Bel, et al. The vimos public extragalactic redshift survey (vipers)-galaxy clustering and redshift-space distortions at z 0.8 in the first data release. *Astronomy & Astrophysics*, 557:A54, 2013.

A Light curves of SN 2020pki and SN 2020xqb

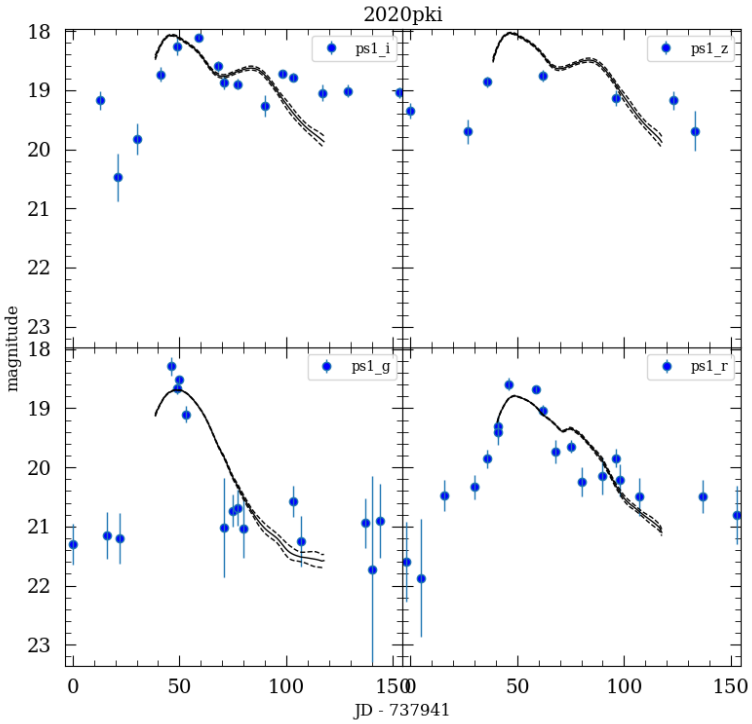

Figure A.1: Light curve of SN 2020pki with best fit for the four PS1 filters. The photometric data points of the SN have clearly been exposed to noise, most likely in the form of variability from its host galaxy.

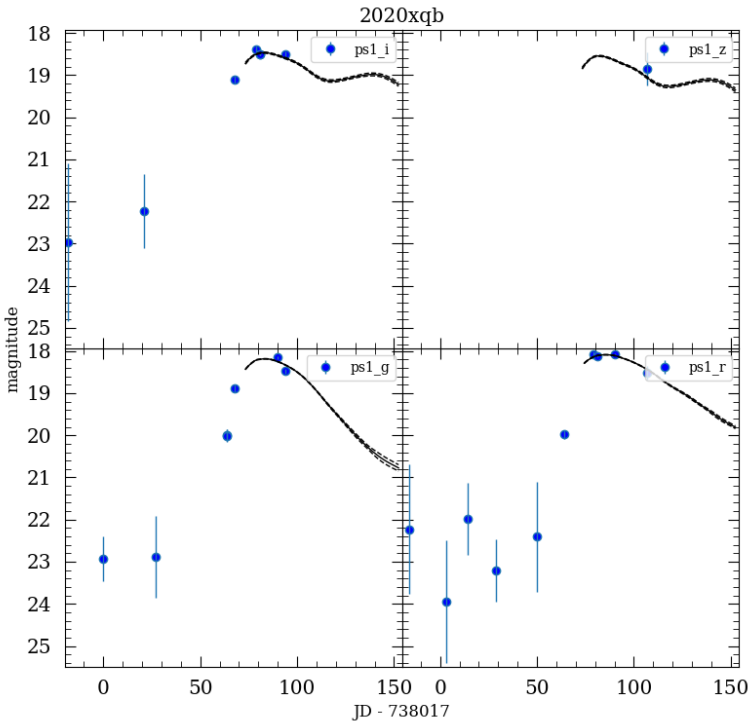

Figure A.2: Light curve of SN 2020xqb with best fit for the four PS1 filters. The SN was manually discarded from the SN sample, as it was a clear outlier in the Hubble diagram.

B Results of fitting *gr* filters

Table B.1: The MCMC fit results of the global parameters for the two samples of SNe in the *gr* filters. The 'All' sample includes an estimate of the redshift uncertainty. 'Residual std.' is the standard deviation of the residuals *after* standardization.

Sample	N_{SN}	P^0 [mag]	P^1 [mag]	R	σ_{int} [mag]	σ_z	Residual std.	ΔRes. std.
Spec	27	-28.27 ± 0.06	-1.19 ± 0.36	2.33 ± 0.52	0.17 ± 0.05		0.27	0.04
All	57	-28.29 ± 0.05	-0.46 ± 0.25	1.88 ± 0.40	0.24 ± 0.04	$(3.44 \pm 2.69) \times 10^{-3}$	0.26	0.05

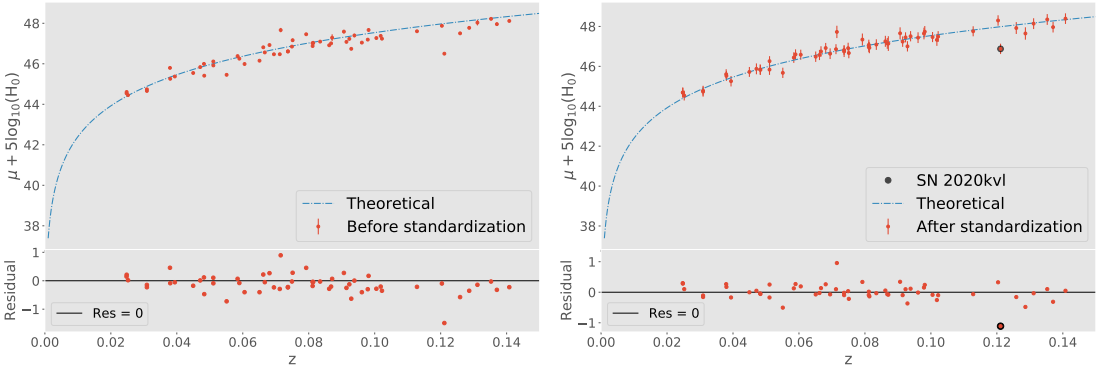

(a) **(b)**

Figure B.1: Hubble diagram for the All sample of $N = 57$ SNe in the *gr* filters. For both plots, a theoretical expectation line has been plotted, as well as the residuals. **(a)** shows the distribution before standardization, and **(b)** shows the distribution after standardization. SN 2020kvl has been highlighted in **(b)** as still being a clear outlier after standardization.

C Figures of combined LLH

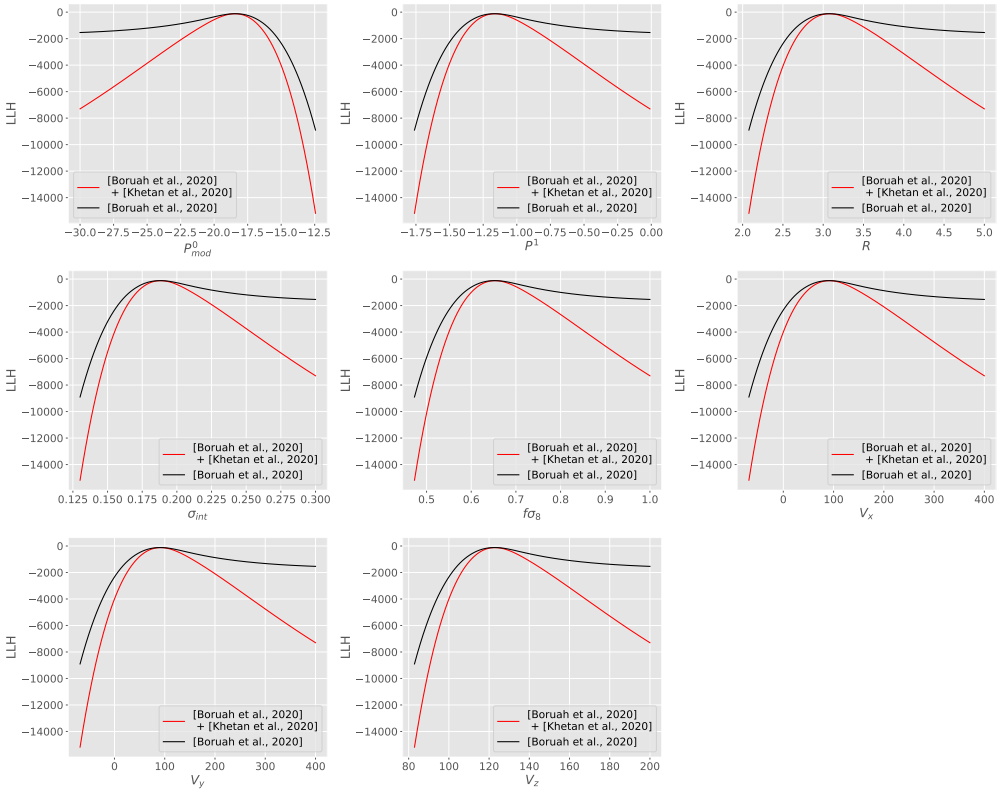

Figure C.1: The combined LLH from [Boruah et al., 2020] and [Khetan et al., 2020] compared to just the LLH from [Boruah et al., 2020], for the eight parameters to be estimated with MCMC.

D Results from using the Forward likelihood method

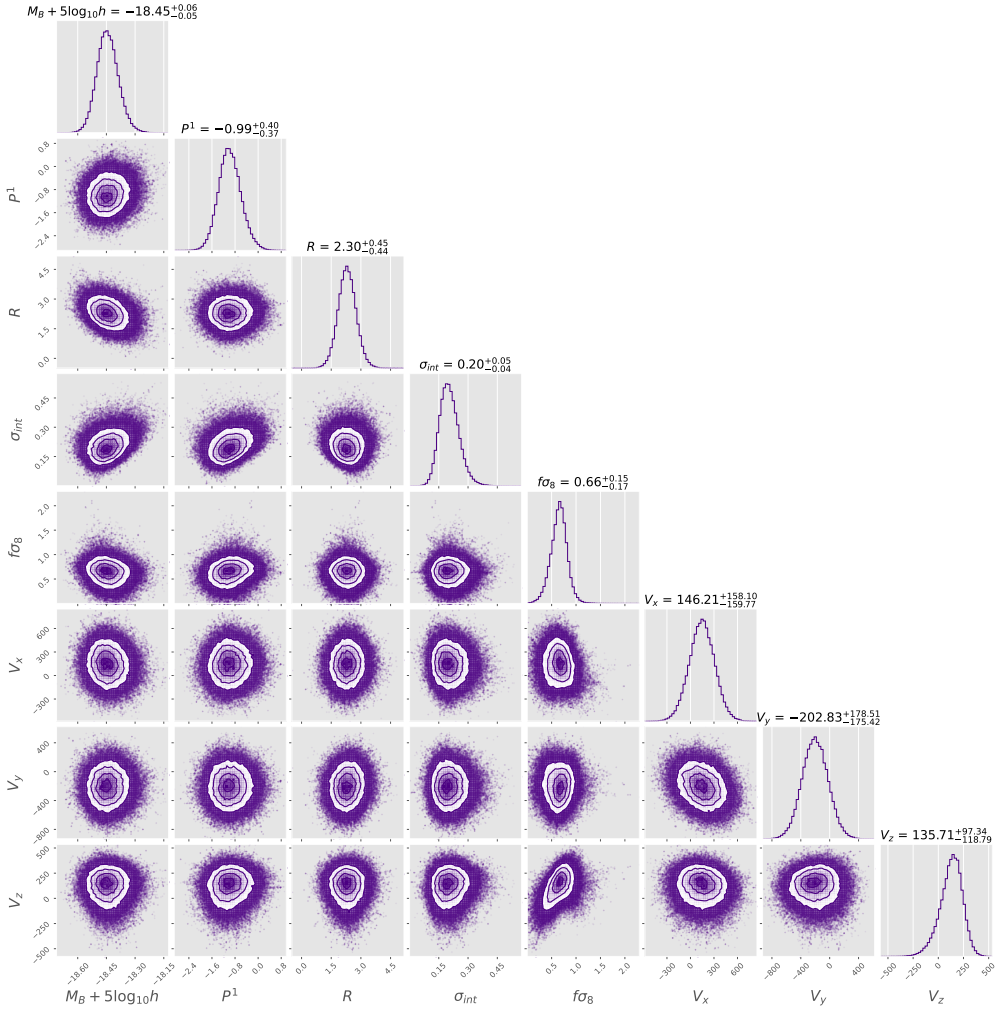

Figure D.1: Cornerplot of the MCMC parameters estimated using the sample of $N = 30$ SNe from YSE, with the combined LLH described in Section 3.5.1.

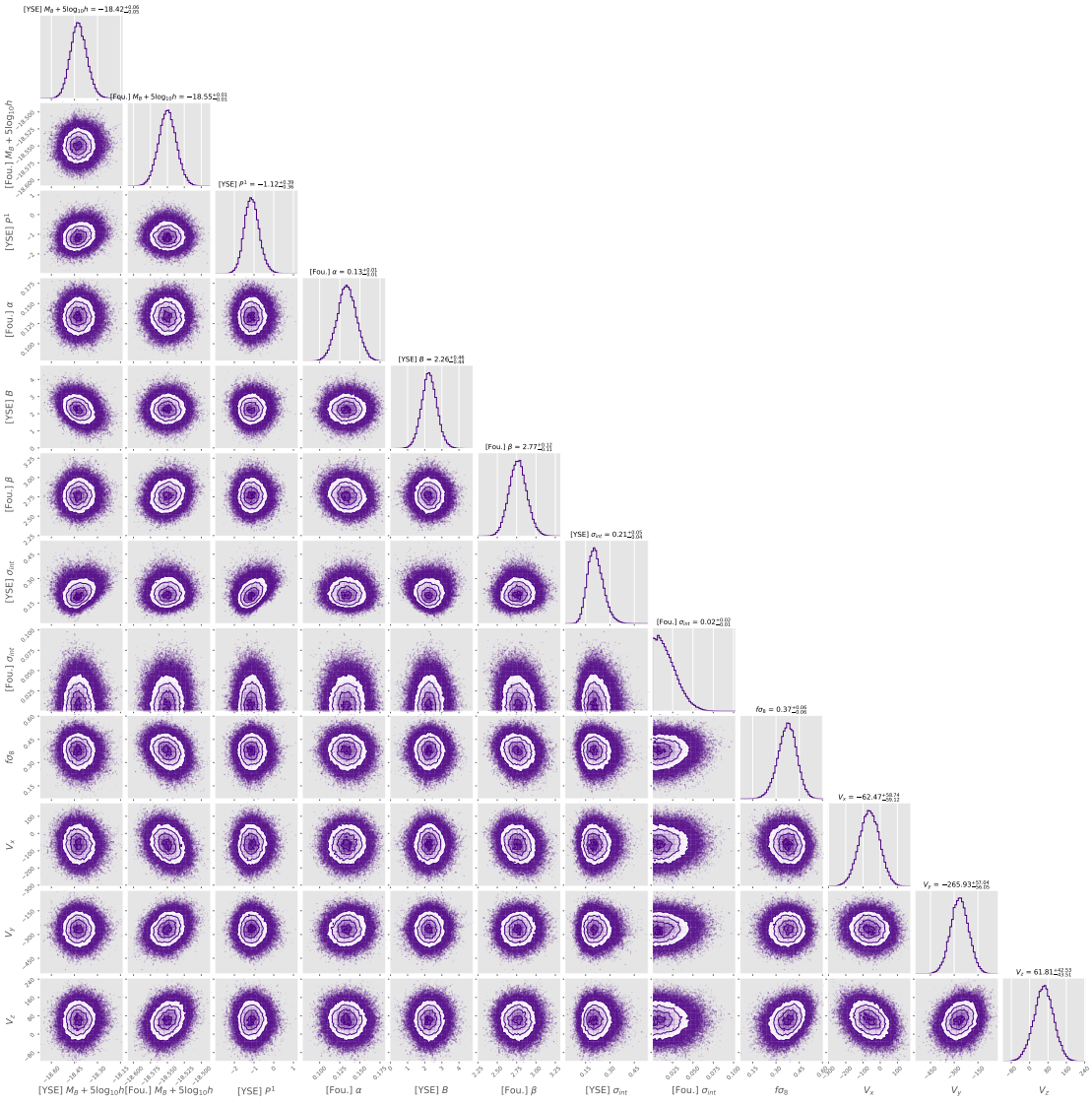

Figure D.2: Cornerplot of the MCMC parameters estimated using the sample of $N = 155$ SNe from the combined YSE + Foundation sample, with the combined LLH described in Section 3.5.1.

Table D.1: The global parameters estimated alongside $f\sigma_8$ and $\boldsymbol{V}_{\rm ext}$ for the three different samples, using the Forward likelihood method. Because the YSE and Foundation sample do not share all parameter notation, the YSE parameters from SNooPy and Foundation parameters from SALT2, respectively, are separated by a comma.

Sample	N_{SN}	$M + 5\log_{10} h$ [mag]	P^1, α [mag]	R, B	σ_{int} [mag]
YSE ($z < 0.07$)	15	-18.40 ± 0.11	-1.78 ± 0.73	2.35 ± 0.64	0.20 ± 0.09
YSE (All)	30	-18.45 ± 0.06	-0.99 ± 0.41	2.30 ± 0.47	0.21 ± 0.05
YSE + Foundation **[YSE]**	155	-18.42 ± 0.05	-1.22 ± 0.38	2.26 ± 0.46	0.21 ± 0.05
YSE + Foundation **[Found.]**	155	-18.55 ± 0.01	0.13 ± 0.01	2.77 ± 0.12	0.02 ± 0.01

E Result of the combined SBF and SH0ES calibration sample

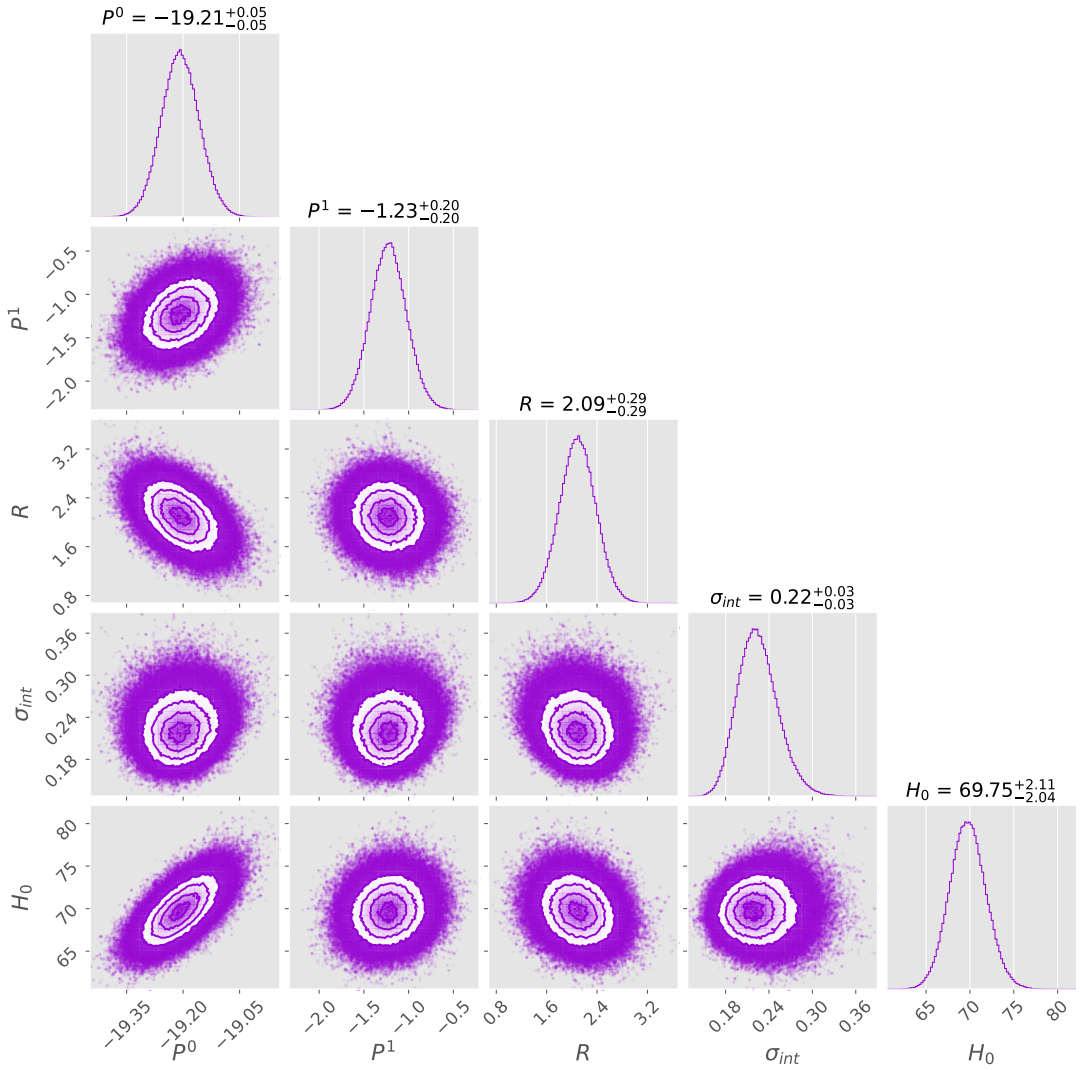

Figure E.1: Cornerplot of the global parameters and H_0 using the combined SBF and SH0ES calibration sample.

F Light curve parameters from SNooPy for the BV All sample

If a SN is also in the Spec sample, its name has been **bolded**.

Supernova	m_B [mag]	σ_{m_B} [mag]	m_V [mag]	σ_{m_V} [mag]	s_{BV}	$\sigma_{s_{BV}}$
2020aajf	18.253	0.046	18.261	0.037	0.959	0.125
2020aavd	19.906	0.142	19.758	0.141	1.240	0.208
2020abpt	19.710	0.033	19.611	0.037	0.944	0.195
22020adkc	18.533	0.040	18.461	0.029	1.167	0.059
2020adlp	18.207	0.047	18.253	0.043	1.315	0.058
2020ann	18.761	0.038	18.786	0.036	0.661	0.159
2020atv	18.671	0.032	18.634	0.041	0.992	0.130
2020dow	17.037	0.059	17.202	0.030	1.041	0.053
2020dwg	17.876	0.043	17.632	0.033	0.964	0.039
2020eci	19.504	0.171	19.302	0.119	1.093	0.212
2020ees	16.245	0.014	16.191	0.021	0.985	0.033
2020evu	18.178	0.033	18.05	0.044	1.073	0.051
2020ewx	17.720	0.056	17.750	0.038	1.296	0.045
2020ilb	17.980	0.035	17.757	0.073	0.953	0.068
2020ioz	18.055	0.019	18.056	0.029	1.254	0.037
2020jny	16.398	0.019	16.404	0.021	0.816	0.031
2020juq	19.723	0.036	19.636	0.059	1.475	0.151
2020kaj	19.846	0.041	19.854	0.044	1.163	0.081
2020kbl	19.258	0.037	19.227	0.078	1.244	0.056
2020lbf	17.228	0.059	17.179	0.042	1.127	0.050
2020lht	18.340	0.146	18.551	0.040	0.986	0.322
2020msu	19.042	0.026	18.978	0.033	1.035	0.057
2020myi	17.950	0.102	18.099	0.040	1.042	0.051
2020pf	18.866	0.052	18.812	0.037	1.210	0.140
2020ppe	17.788	0.065	17.592	0.052	0.633	0.036
2020pst	17.302	0.023	17.308	0.024	1.019	0.037
2020psv	19.044	0.061	19.012	0.029	0.851	0.046
2020pyf	18.384	0.037	18.384	0.027	0.838	0.034
2020pyy	19.383	0.047	19.380	0.037	1.043	0.061
2020qkx	19.200	0.071	19.323	0.075	1.083	0.125
2020qql	18.034	0.019	18.085	0.027	1.247	0.037
2020rii	18.773	0.035	18.802	0.057	0.810	0.063
2020rkt	18.962	0.056	18.989	0.043	1.139	0.081
2020rmy	19.759	0.074	19.671	0.064	1.071	0.086

2020rvq	19.961	0.113	19.778	0.078	1.187	0.129
2020ryb	18.808	0.033	18.928	0.053	0.854	0.060
2020ryn	18.405	0.047	18.451	0.067	1.008	0.067
2020scj	19.264	0.062	19.056	0.072	1.069	0.125
2020sia	18.977	0.068	19.021	0.055	1.089	0.105
2020skd	18.093	0.028	18.068	0.026	1.105	0.048
2020svo	17.049	0.024	17.046	0.026	1.017	0.040
2020tip	19.187	0.076	19.115	0.039	1.073	0.083
2020tqz	20.150	0.055	20.120	0.062	1.347	0.147
2020ulz	18.949	0.068	18.862	0.045	1.016	0.069
2020wux	17.909	0.026	17.921	0.033	1.191	0.054
2020zbr	19.407	0.086	19.511	0.077	1.081	0.090
2020zgc	18.294	0.045	18.369	0.048	0.922	0.053
2020zhh	16.427	0.021	16.414	0.027	0.944	0.033
2021aci	18.458	0.071	18.591	0.053	1.120	0.084
2021afj	19.468	0.071	19.423	0.096	0.734	0.073
2021agu	17.657	0.046	17.711	0.032	1.006	0.044
2021bmb	17.656	0.020	17.469	0.026	1.070	0.046
2021bsf	16.296	0.014	16.367	0.028	0.788	0.034
2021cca	18.712	0.042	18.608	0.062	1.142	0.073
2021ccl	18.854	0.041	18.854	0.030	1.170	0.133
2021dha	18.827	0.104	18.758	0.051	0.860	0.050
2021dnm	17.796	0.035	17.513	0.034	1.071	0.044
2021dpw	18.428	0.101	18.459	0.036	1.187	0.081
2021fwm	18.220	0.052	18.253	0.029	1.078	0.065
2021hlp	18.663	0.047	18.485	0.038	0.819	0.054
2021hol	18.643	0.051	18.636	0.031	0.886	0.050
2021iok	19.546	0.073	19.620	0.076	0.987	0.228
2021pl	18.641	0.062	18.620	0.060	0.873	0.051
2021us	18.684	0.036	18.677	0.038	0.860	0.041

G Light curve fits from SNooPy for the BV All sample

If a SN is also in the Spec sample, its name in the caption has been **bolded**.

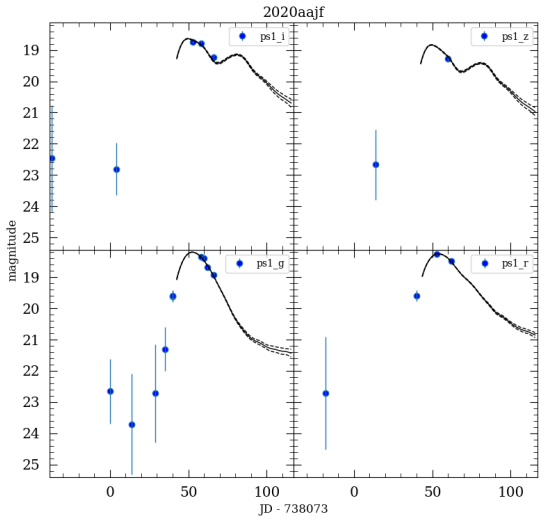

Figure G.1: SN 2020aajf

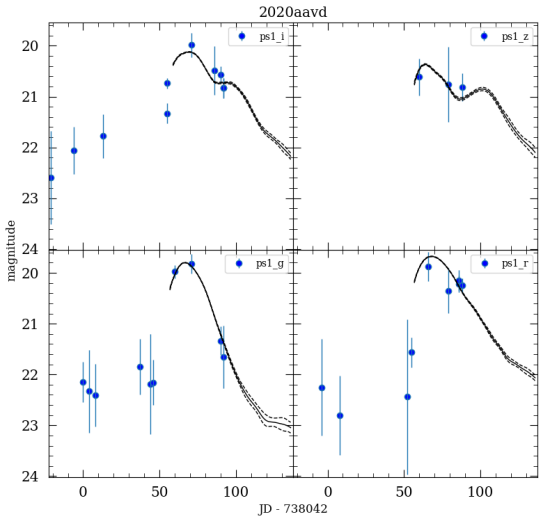

Figure G.2: SN 2020aavd

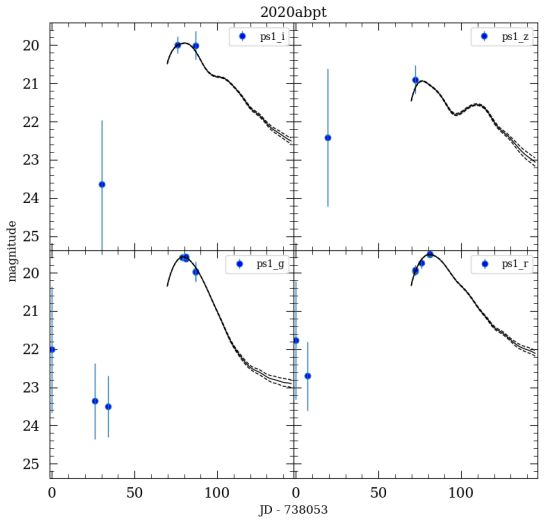

Figure G.3: SN **2020abpt**

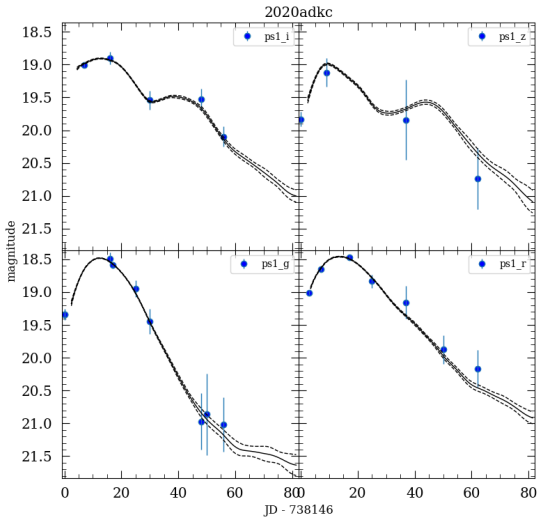

Figure G.4: SN **2020adkc**

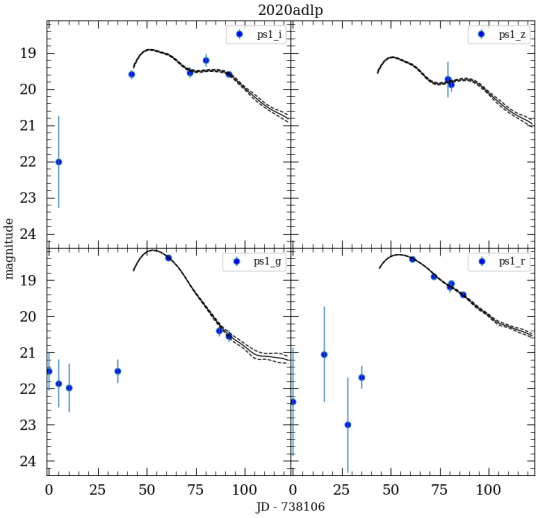

Figure G.5: SN **2020adlp**

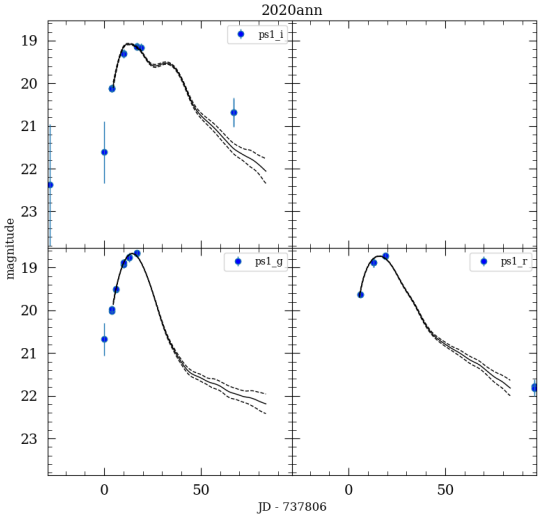

Figure G.6: SN 2020ann

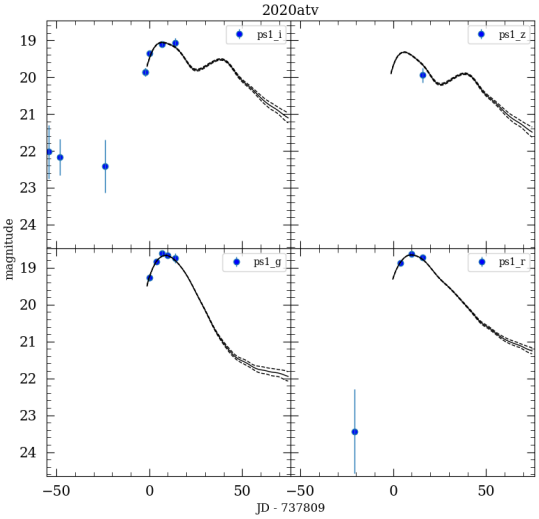

Figure G.7: SN 2020atv

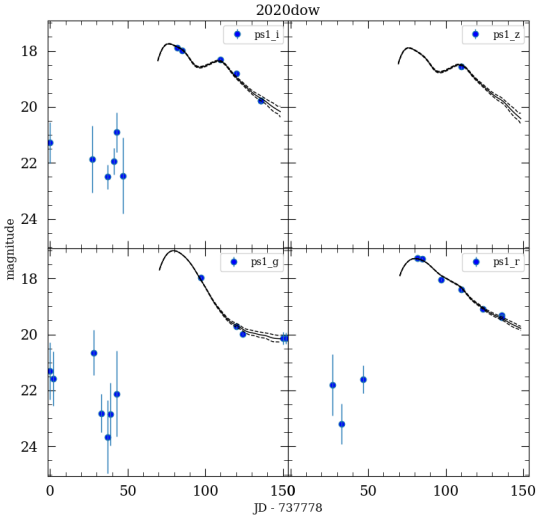

Figure G.8: SN **2020dow**

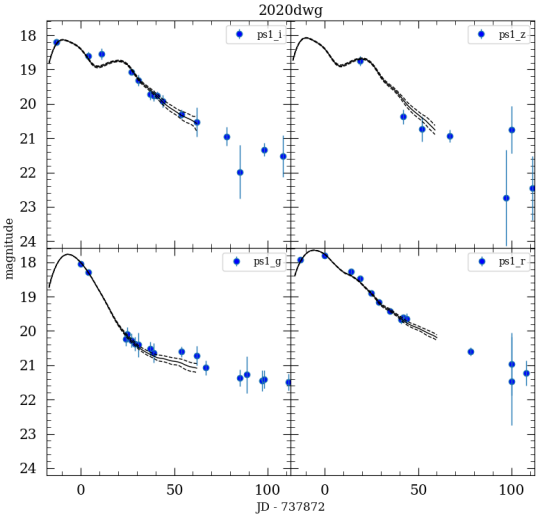

Figure G.9: SN **2020dwg**

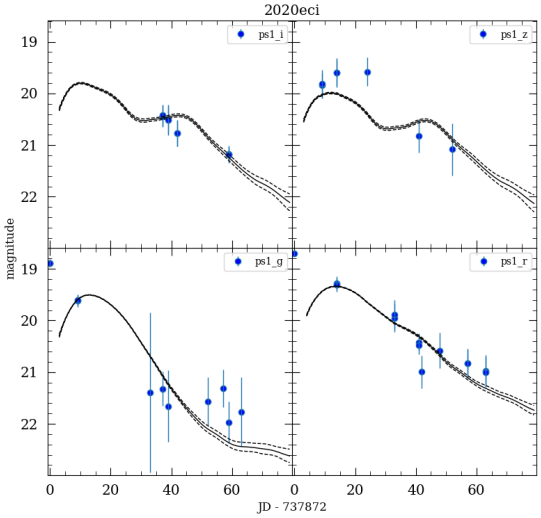

Figure G.10: SN **2020eci**

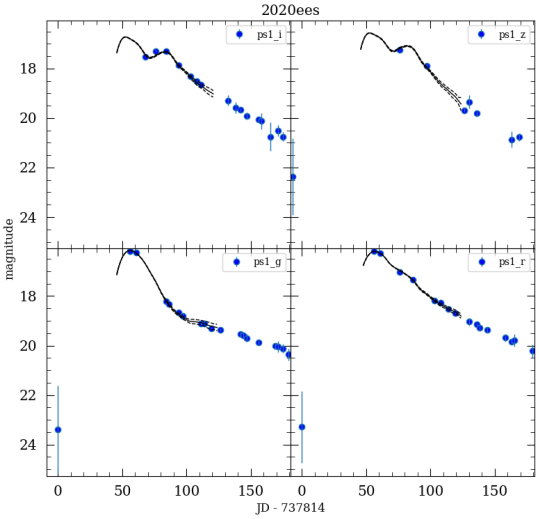

Figure G.11: SN **2020ees**

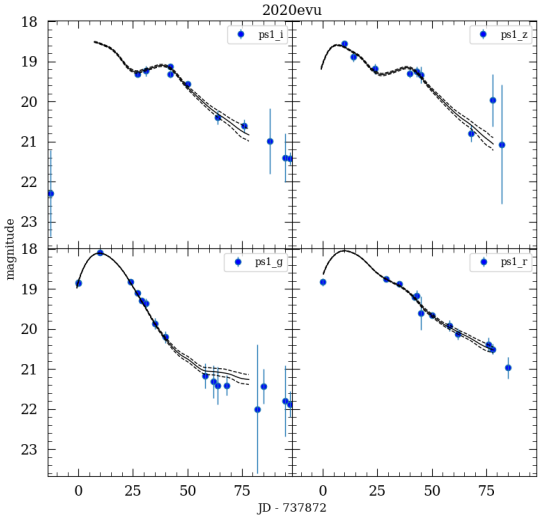

Figure G.12: SN **2020evu**

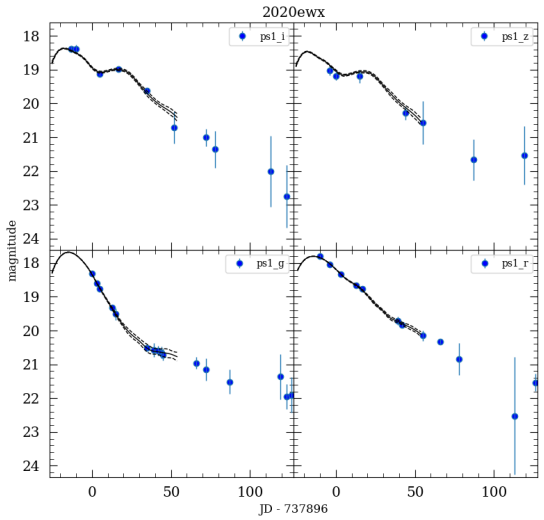

Figure G.13: SN 2020ewx

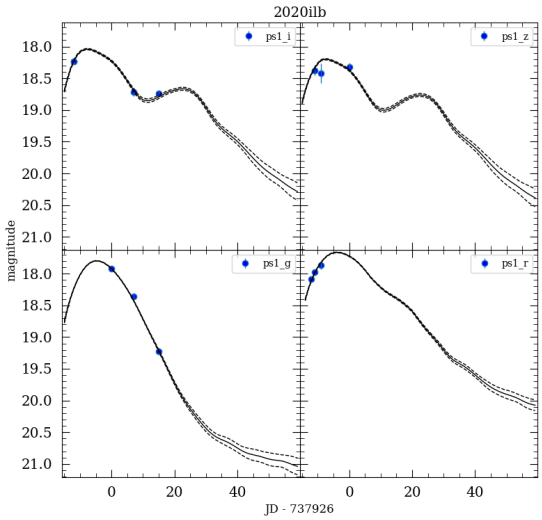

Figure G.14: SN **2020ilb**

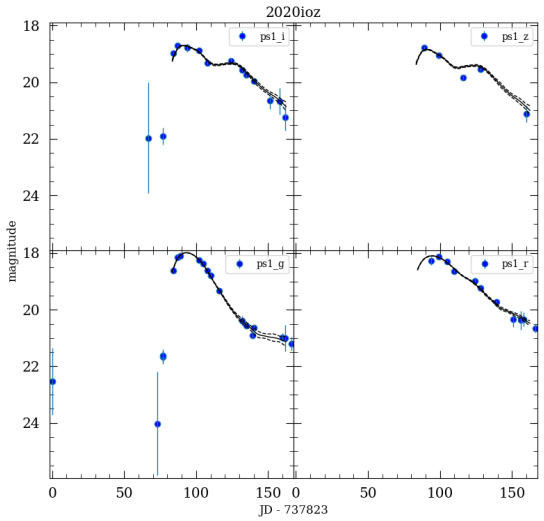

Figure G.15: SN 2020ioz

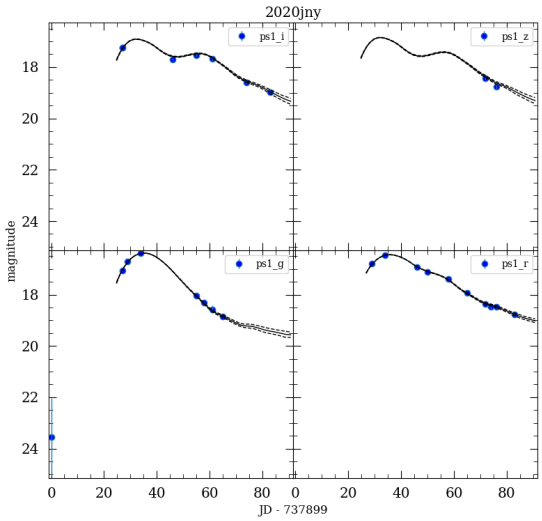

Figure G.16: SN **2020jny**

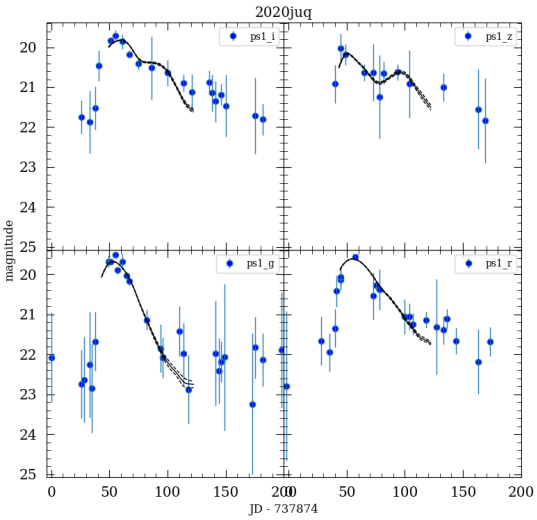

Figure G.17: SN 2020juq

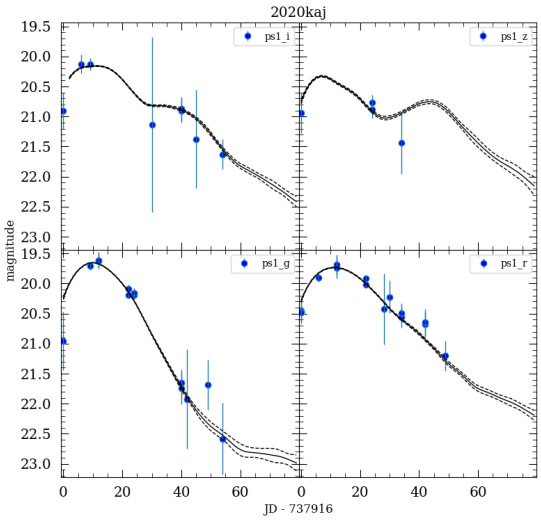

Figure G.18: SN 2020kaj

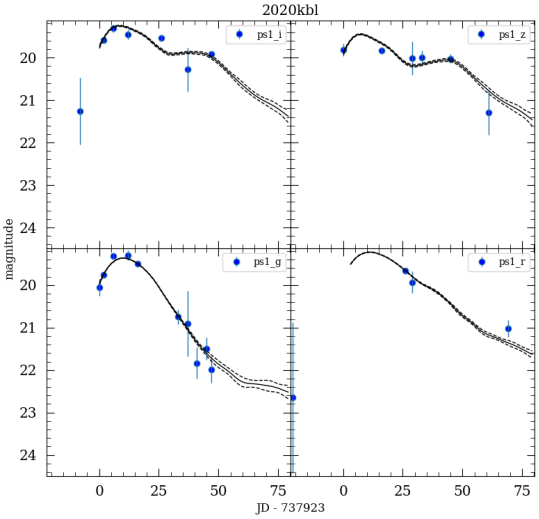

Figure G.19: SN 2020kbl

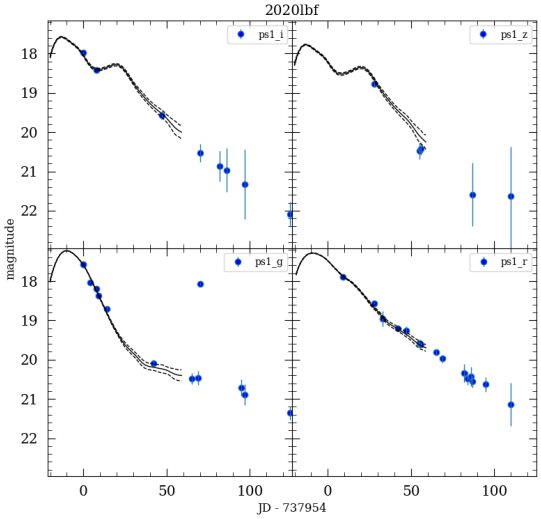

Figure G.20: SN **2020lbf**

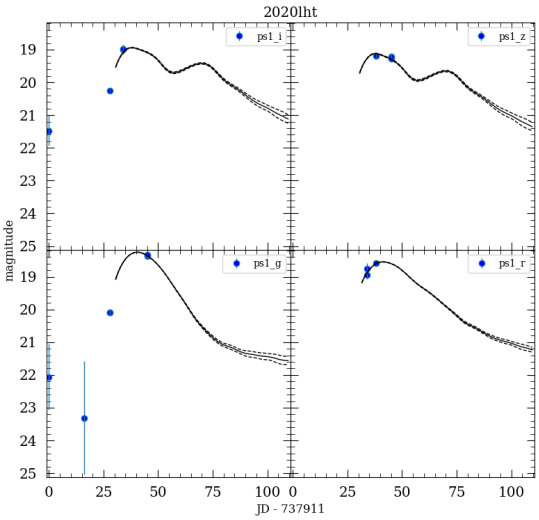

Figure G.21: SN 2020lht

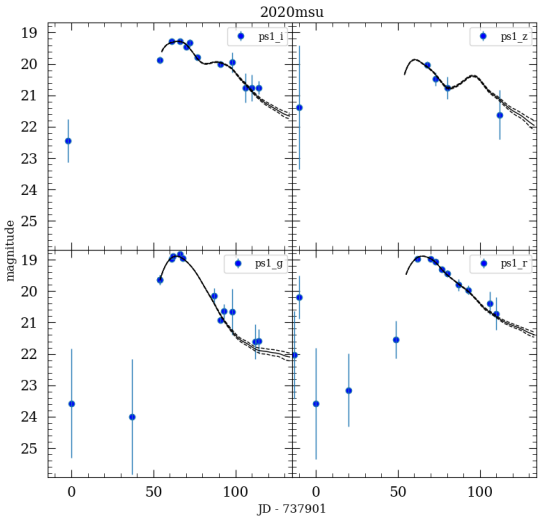

Figure G.22: SN 2020msu

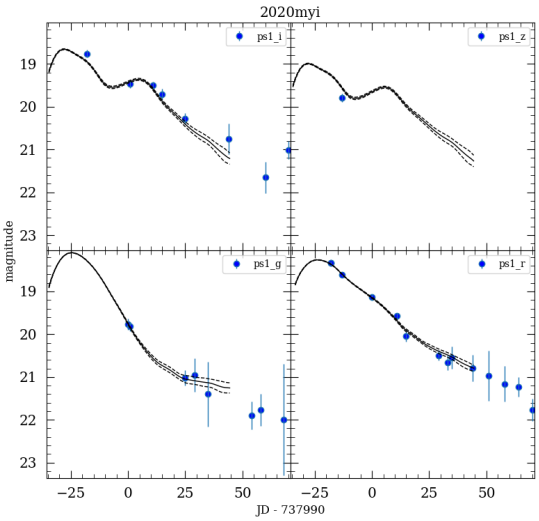

Figure G.23: SN **2020myi**

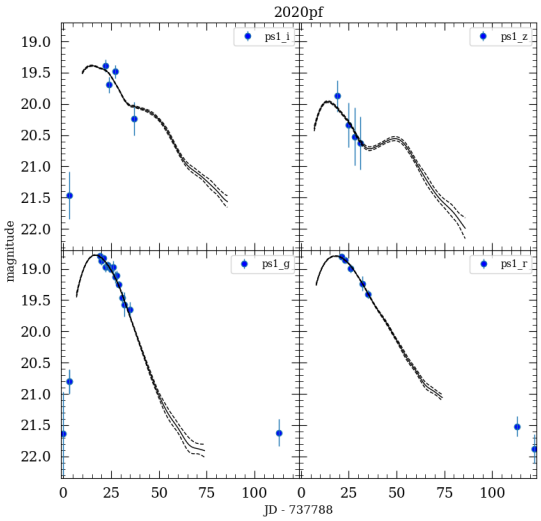

Figure G.24: SN 2020pf

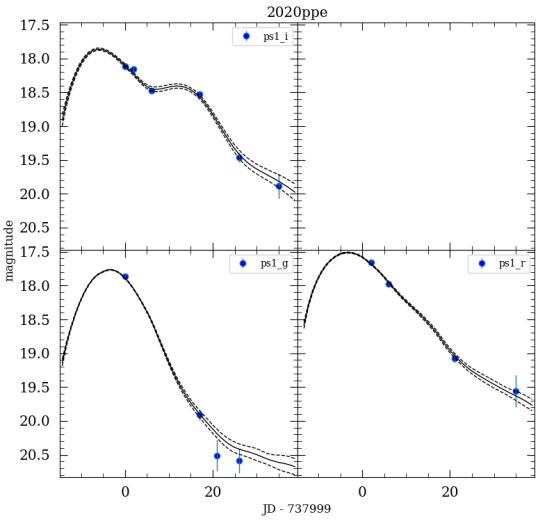

Figure G.25: SN **2020ppe**

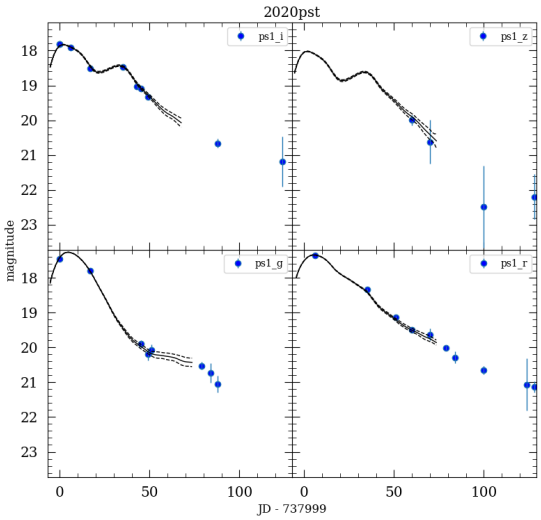

Figure G.26: SN **2020pst**

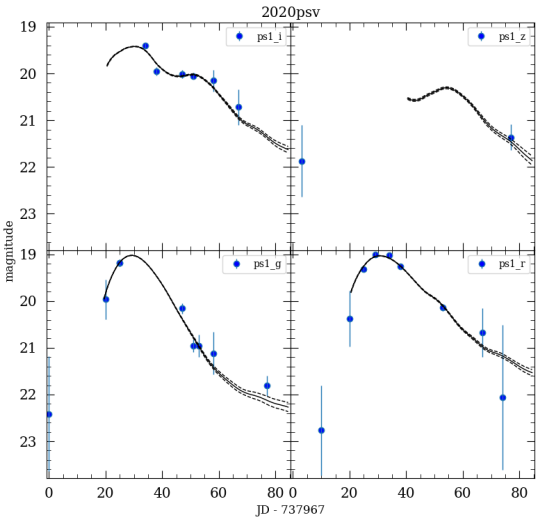

Figure G.27: SN **2020psv**

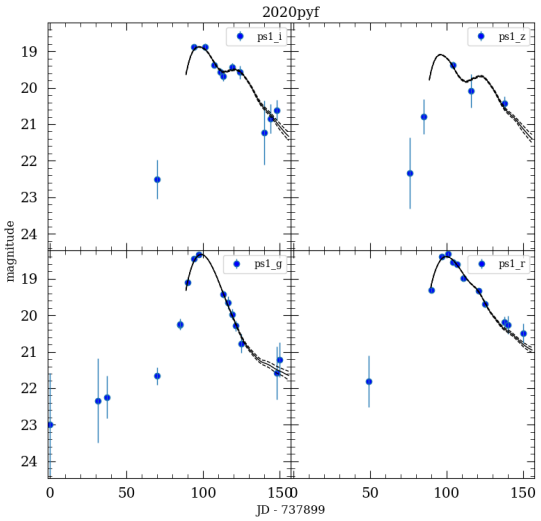

Figure G.28: SN **2020pyf**

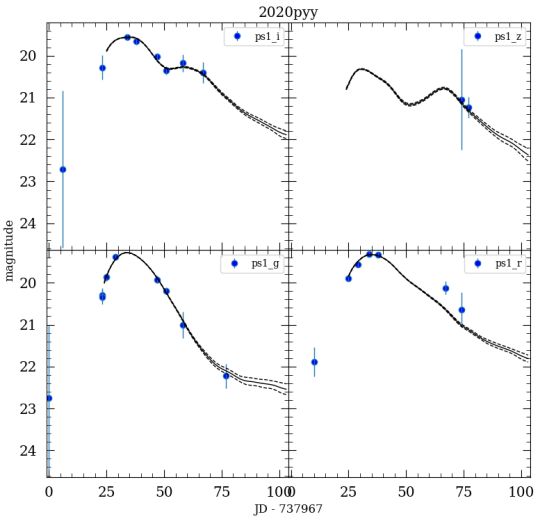

Figure G.29: SN 2020pyy

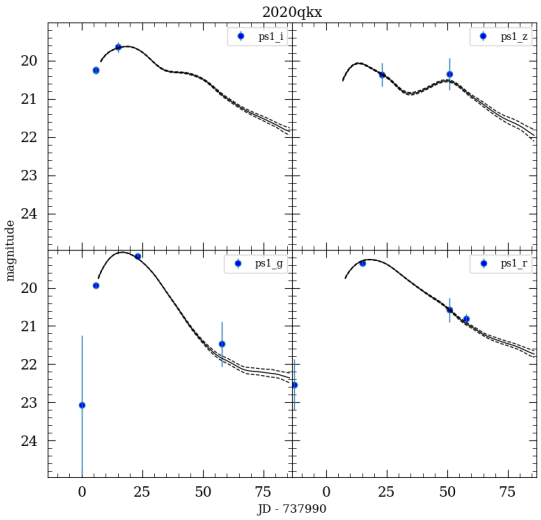

Figure G.30: SN 2020qkx

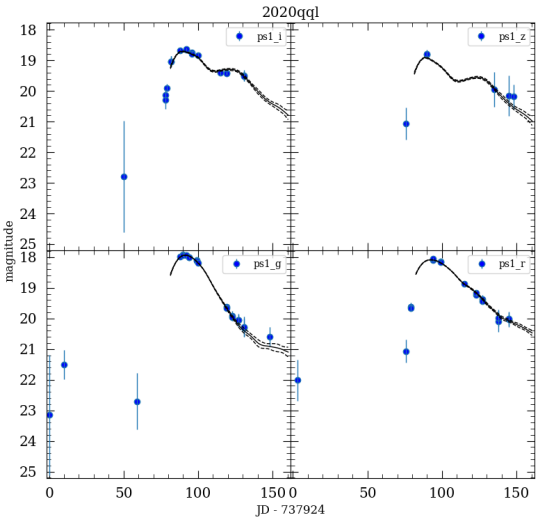

Figure G.31: SN 2020qql

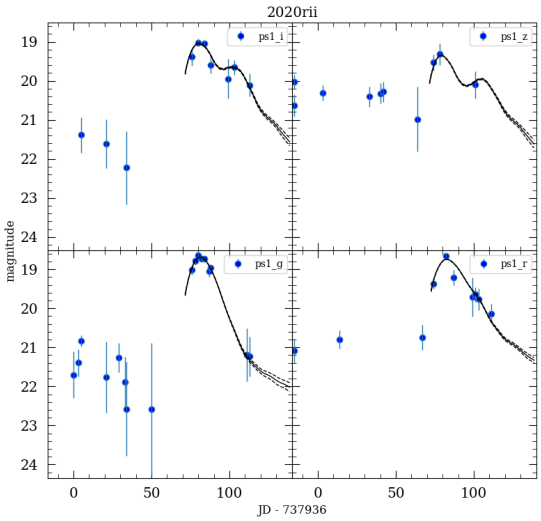

Figure G.32: SN **2020rii**

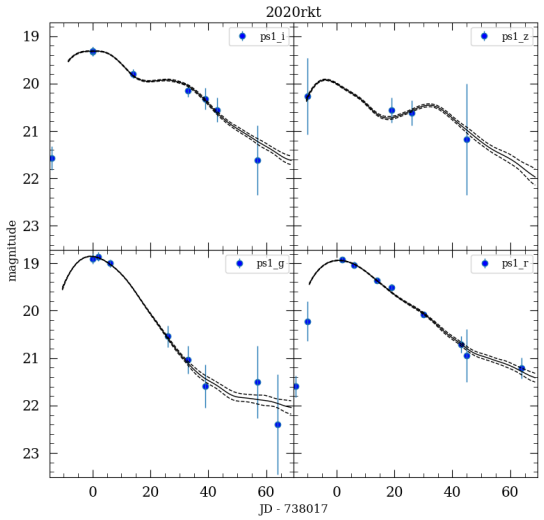

Figure G.33: SN 2020rkt

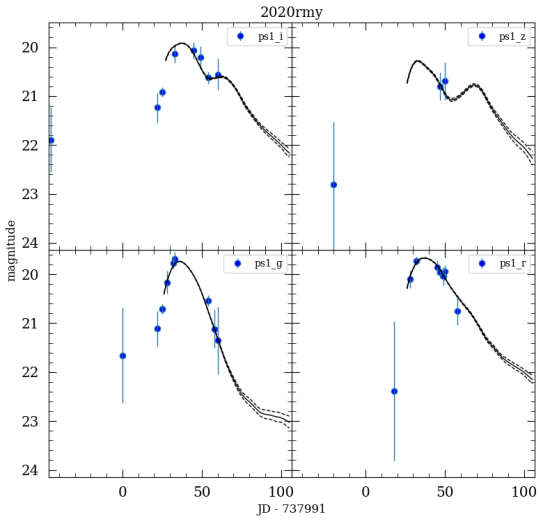

Figure G.34: SN 2020rmy

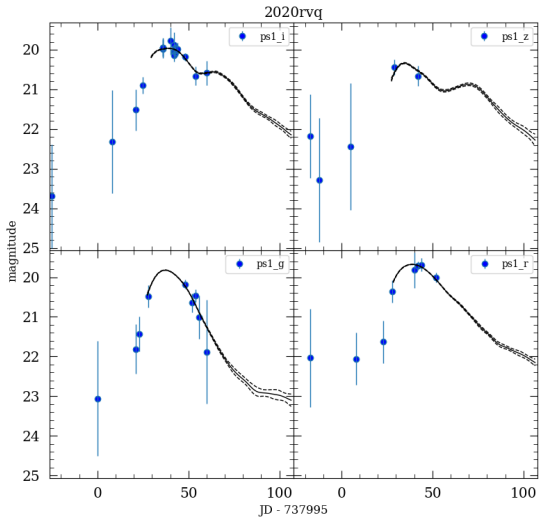

Figure G.35: SN 2020rvq

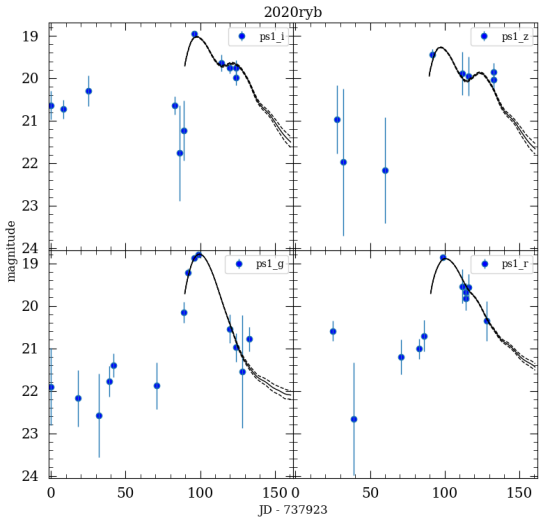

Figure G.36: SN **2020ryb**

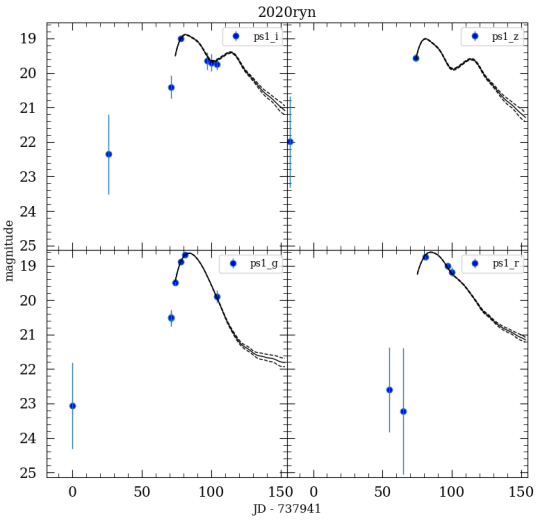

Figure G.37: SN 2020ryn

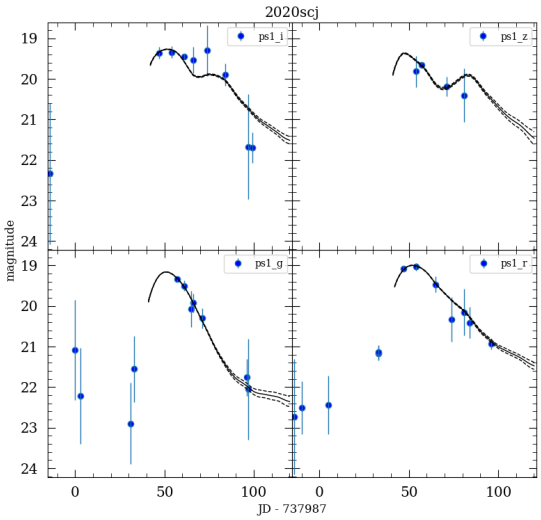

Figure G.38: SN 2020scj

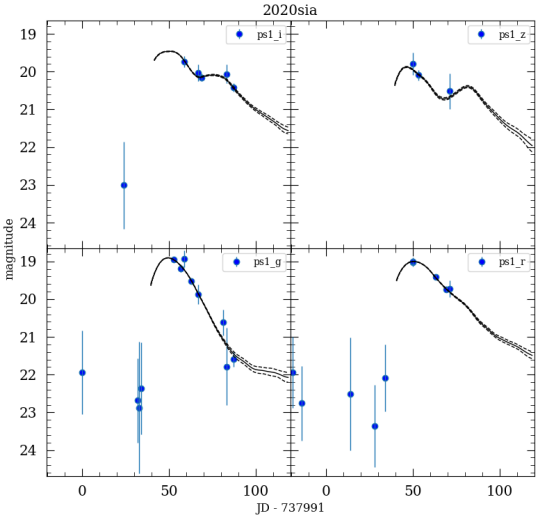

Figure G.39: SN 2020sia

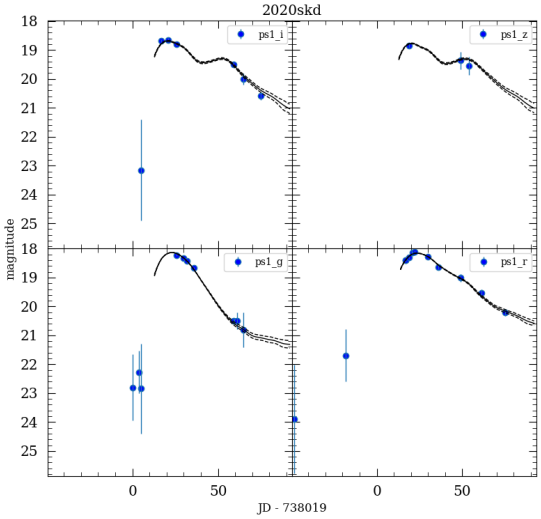

Figure G.40: SN 2020skd

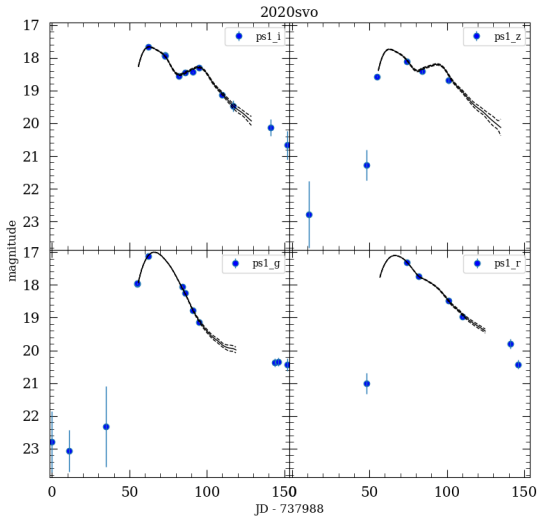

Figure G.41: SN **2020svo**

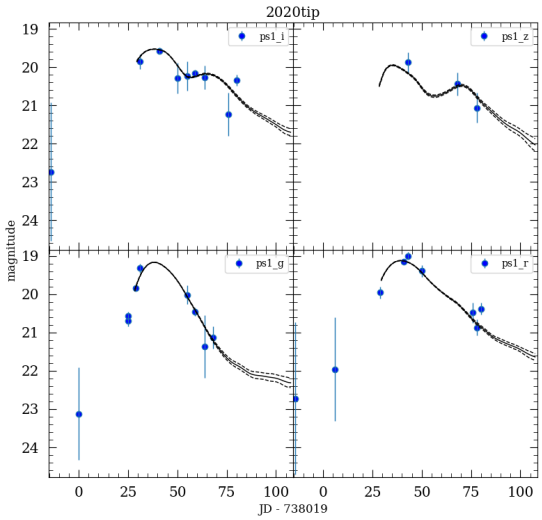

Figure G.42: SN 2020tip

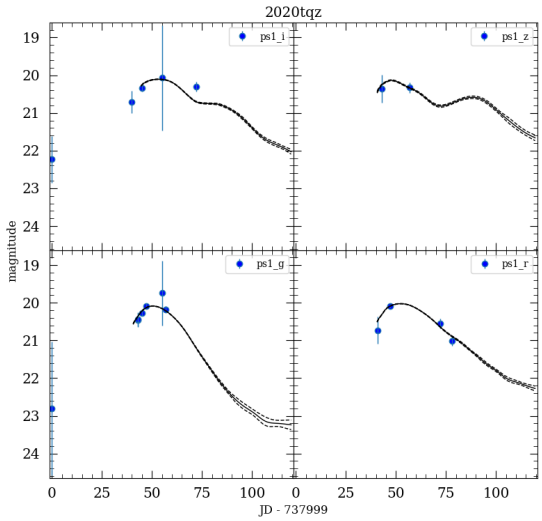

Figure G.43: SN **2020tqz**

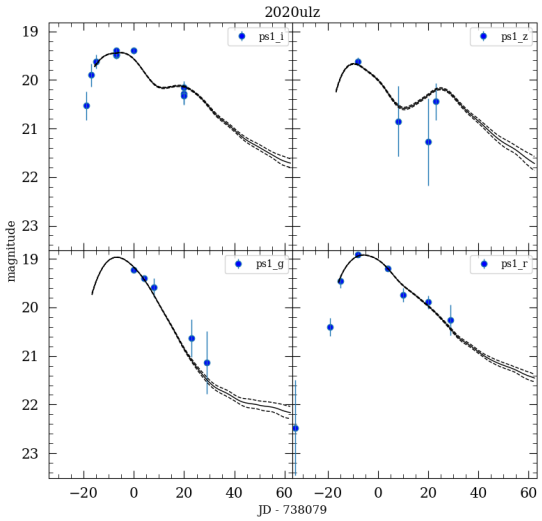

Figure G.44: SN 2020ulz

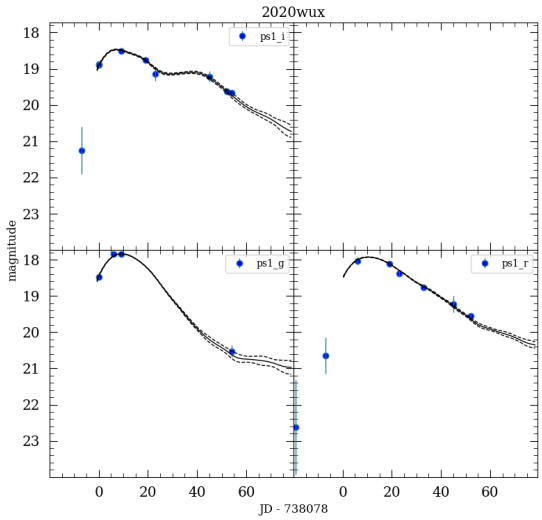

Figure G.45: SN 2020wux

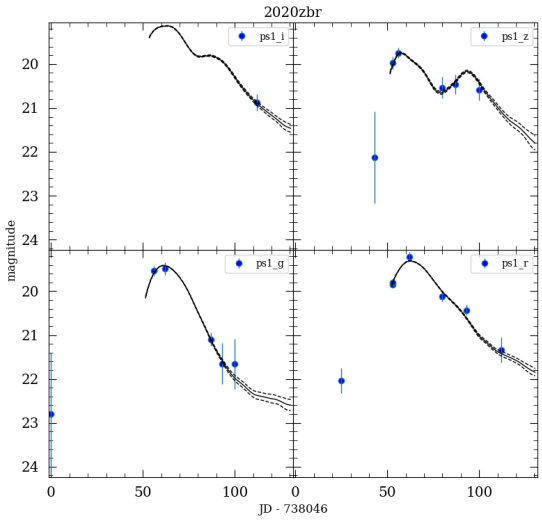

Figure G.46: SN 2020zbr

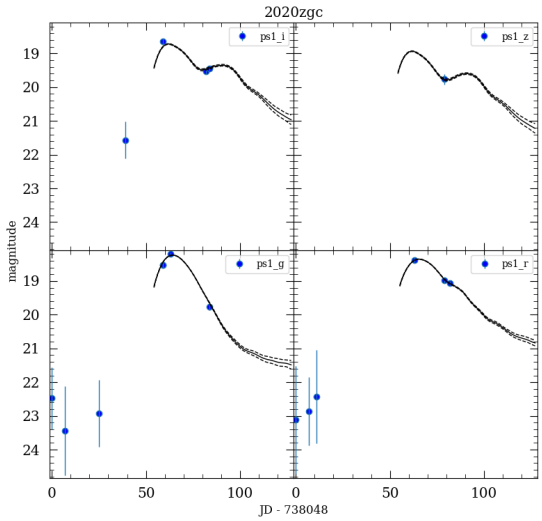

Figure G.47: SN **2020zgc**

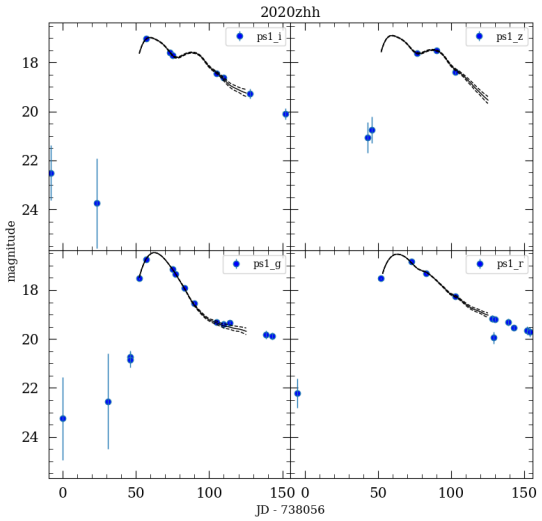

Figure G.48: SN **2020zhh**

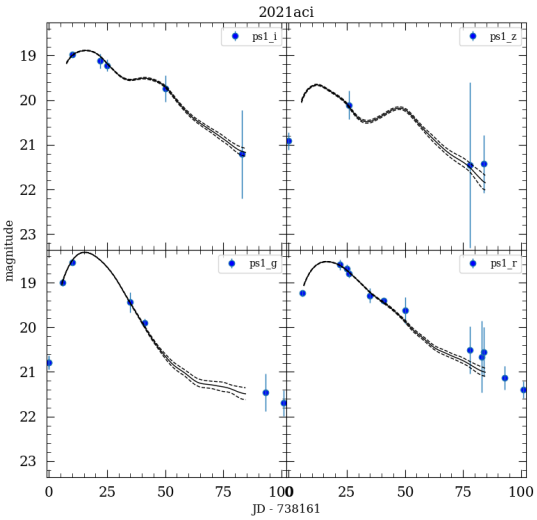

Figure G.49: SN 2021aci

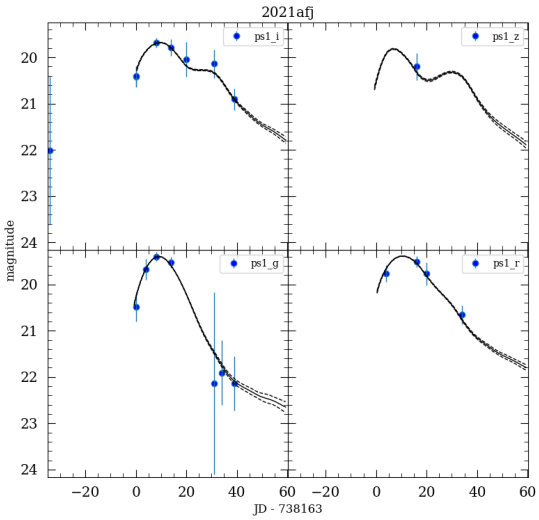

Figure G.50: SN **2021afj**

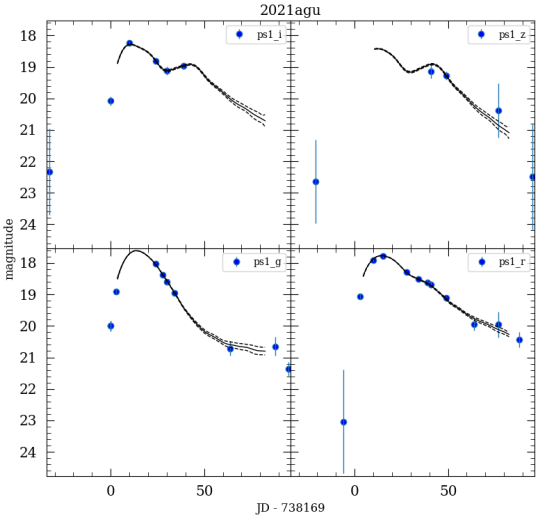

Figure G.51: SN 2021agu

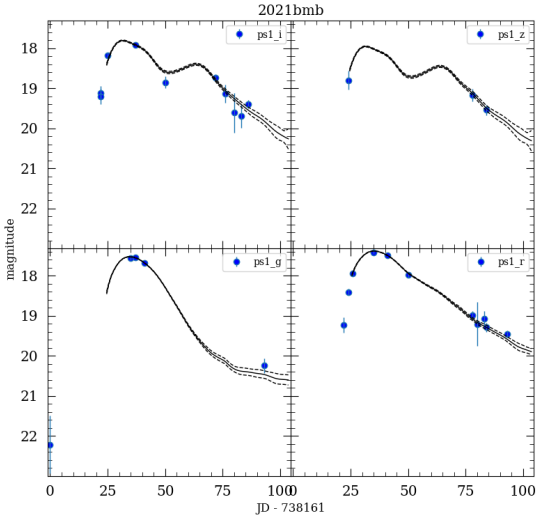

Figure G.52: SN **2021bmb**

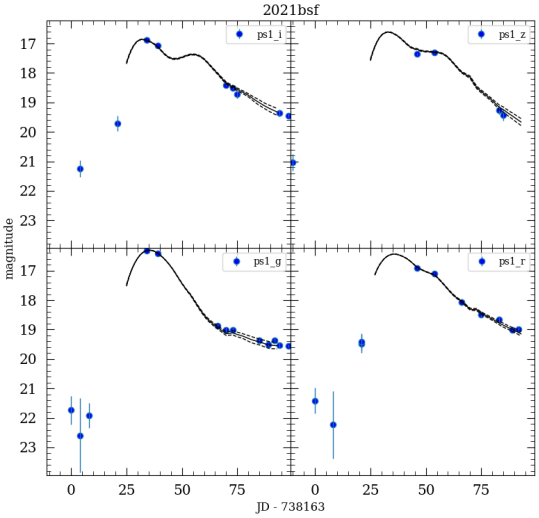

Figure G.53: SN **2021bsf**

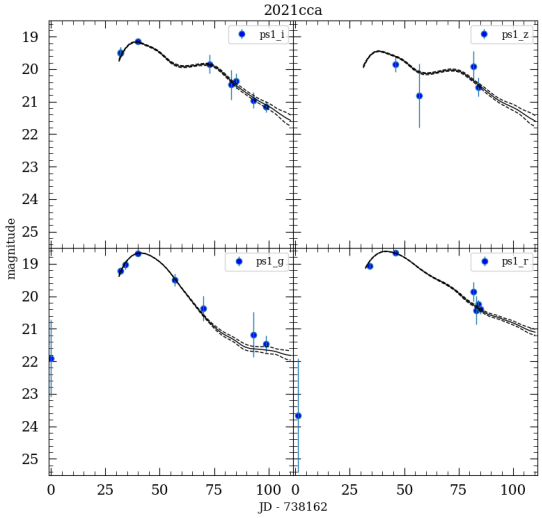

Figure G.54: SN 2021cca

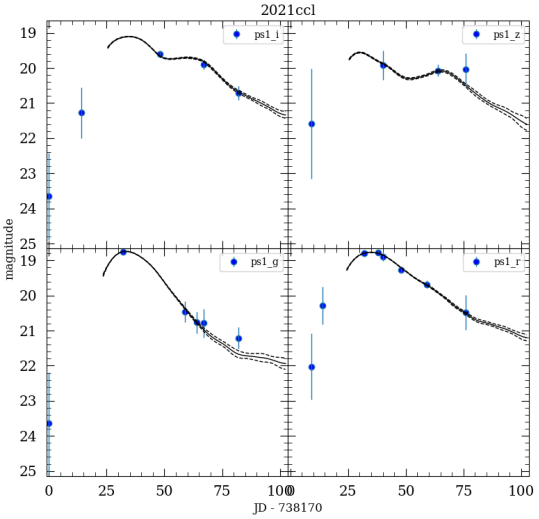

Figure G.55: SN **2021ccl**

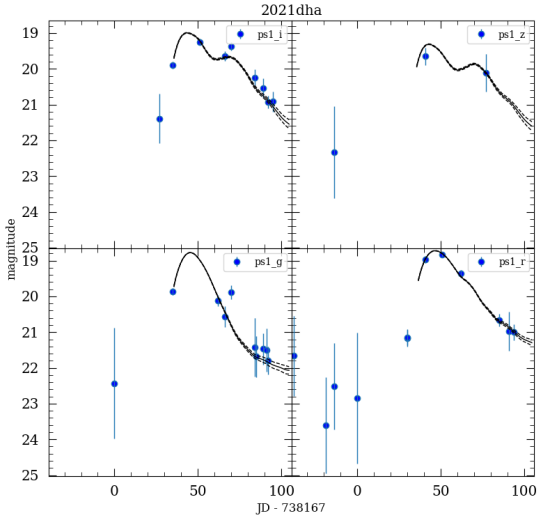

Figure G.56: SN **2021dha**

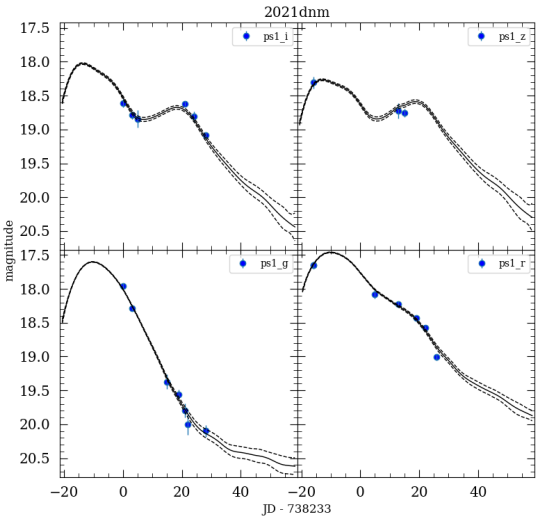

Figure G.57: SN **2021dnm**

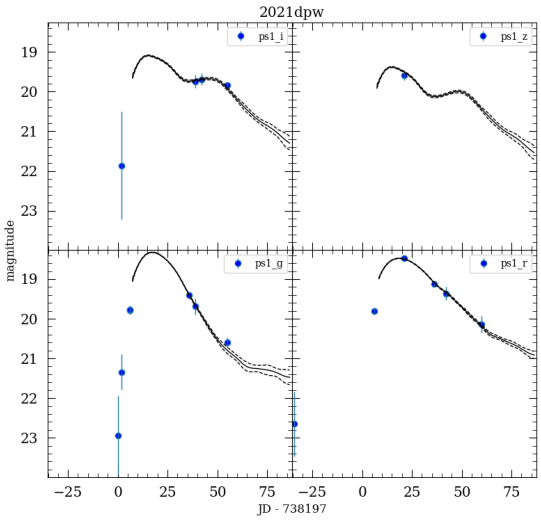

Figure G.58: SN 2021dpw

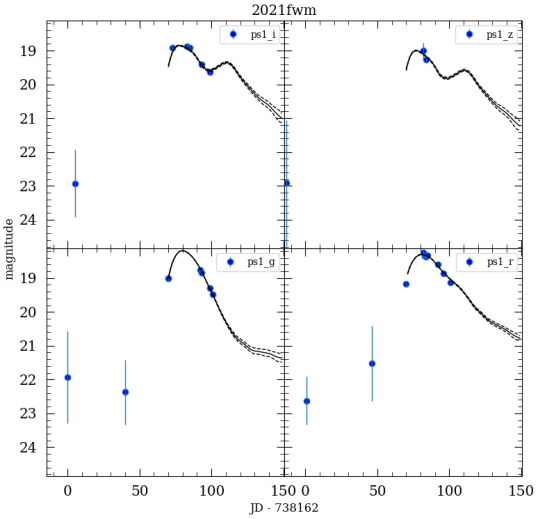

Figure G.59: SN 2021fwm

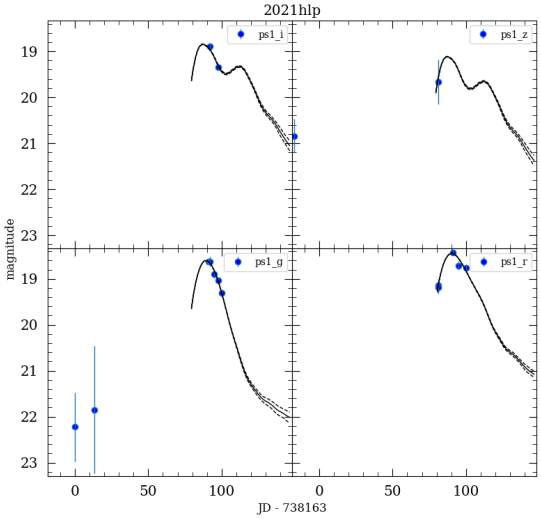

Figure G.60: SN 2021hlp

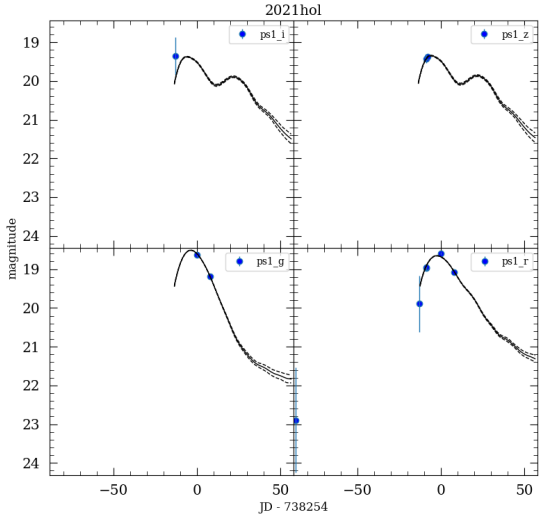

Figure G.61: SN **2021hol**

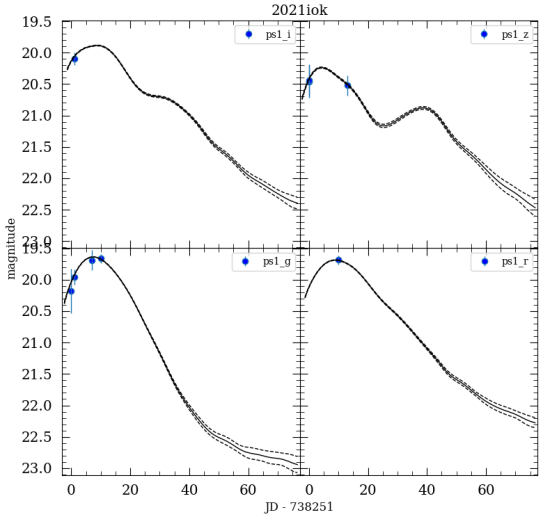

Figure G.62: SN 2021iok

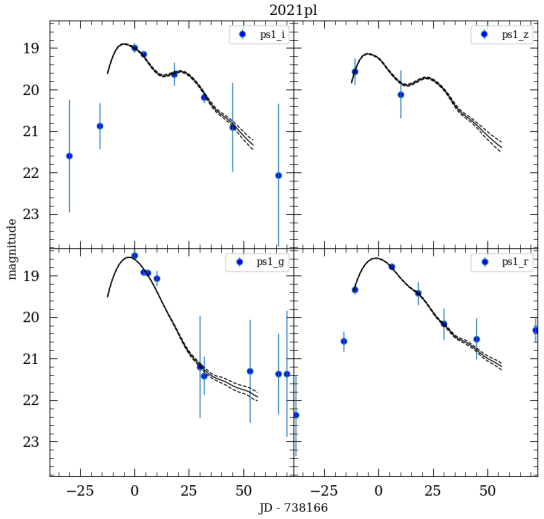

Figure G.63: SN **2021pl**

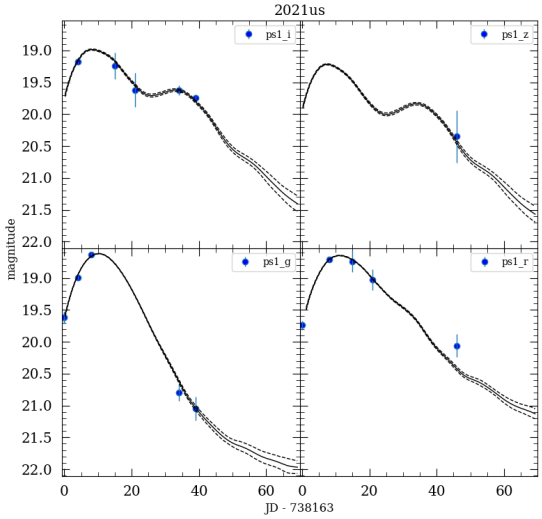

Figure G.64: SN 2021us